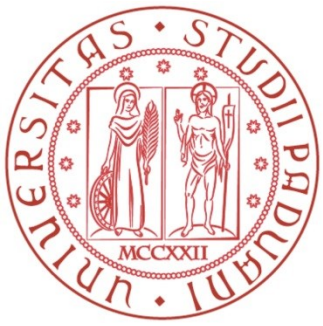

Università degli Studi di Padova

Dipartimento di Ingegneria Industriale

Corso di Laurea Magistrale in Ingegneria Energetica

Tesi di Laurea Magistrale

Experimental investigation of condensation of propylene inside a horizontal enhanced tube

Relatore: Prof. Ing. Davide Del Col (DII-Università di Padova)

Correlatore: Prof. Ing. Luke Andrea (TTK Universität Kassel)

Ing. Christos Tsitsiloudis (TTK Universität Kassel)

Candidato: Camerin Maura (1240331)

Anno Accademico 2021/2022

To
all the people
that kept on believe in me

A tutte le persone
che hanno creduto in me

Sommario

La consapevolezza che ogni azione antropica richiede il consumo di energia sprona l'intera comunità scientifica verso una transizione all'uso di risorse rinnovabili e all'aumento dell'efficienza di tutti i processi. Il presente lavoro si pone l'obiettivo di massimizzare l'efficacia di scambio termico tra un idrocarburo allo stato gassoso e un fluido secondario di raffreddamento durante il processo di condensazione. Per perseguire questo scopo, è stata costruita una struttura sperimentale dove svolgere i test, per determinare le condizioni operative che garantiscano il miglior compromesso tra l'aumento del coefficiente di scambio termico e l'aumento delle perdite di pressione. Questo lavoro è stato svolto presso l'Università di Kassel. La configurazione dell'impianto è tale da permettere non solo test con fluido bifase, ma anche con fluidi monofase per il de-surriscaldamento di un gas e il sotto-raffreddamento di un liquido. L'intera struttura è costituita da un circuito primario e da quattro circuiti secondari. All'interno del circuito primario è locata la sezione di test, costituita da uno scambiatore di calore tubo-in-tubo. Il tubo più interno è un canale micro-alettato in cui fluisce il fluido di lavoro, mentre nella sezione anulare più esterna scorre, in controcorrente, il fluido secondario di raffreddamento. Ogni test viene condotto in determinate condizioni operative relative a temperatura, pressione e titolo di vapore. Queste variabili possono essere modificate al fine di ottenere una vasta panoramica che mostri l'efficacia del processo di scambio termico in diverse situazioni. Il presente lavoro è strutturato in diversi capitoli; dopo un'iniziale revisione dei documenti presenti in letteratura in cui vengono presentate le principali nozioni predittive di interesse, viene descritta in dettaglio la struttura sperimentale. Successivamente, segue un'analisi del processo di calcolo delle variabili ottenute indirettamente e, per concludere, i risultati raggiunti sono descritti e commentati. Tutti i risultati derivanti dai test sperimentali sono confrontati con quelli ottenuti attraverso l'implementazione di correlazioni teoriche presenti in letteratura. Dall'analisi dei dati si evince il vantaggioso aumento del coefficiente di scambio termico derivante dall'utilizzo di una struttura micro-alettata, tuttavia bisogna considerare che si verifica anche un aumento delle perdite di pressione rispetto al caso in cui si adoperi una struttura liscia.

La convenienza nell'utilizzo di una certa soluzione va considerata a seconda dell'applicazione.

Abstract

The awareness that every anthropogenic action requires the consumption of energy spurs the entire scientific community towards a transition to the use of renewable resources and an increase in the efficiency of all processes. The present work aims to maximize the efficiency of heat exchange between a hydrocarbon in the gaseous state and a secondary cooling fluid during the condensation process. In order to pursue this aim, an experimental facility has been built to carry out the tests, to determine the operating conditions that guarantee the best compromise between increasing the heat exchange coefficient and increasing the pressure losses. This work has been carried out at Institute of Technical Thermodynamics at the University of Kassel. The configuration of the facility is such as to allow not only tests with two-phase fluids, but also with single-phase fluids for the de-superheating of a gas and the sub-cooling of a liquid. The entire structure consists of a primary circuit and four secondary circuits. The test section, which consists of a tube-in-tube heat exchanger, is located inside the primary circuit. The inner tube is a micro-fin channel in which the working fluid flows, while the secondary cooling fluid flows in counterflow in the outer annular section. Each test is conducted under certain constant operating conditions relating to temperature, pressure and vapor pressure. These variables can be modified in order to obtain a broad overview showing the effectiveness of the heat transfer process in different situations. The present work is structured in several chapters; after an initial review of the papers in the literature in which the main theoretical notions of interest are presented, the experimental setup is described in detail. Subsequently, an analysis of the calculation process of the indirectly obtained variables follows and, to conclude, the results achieved are described and commented upon. All results deriving from the experimental tests are compared with those obtained through the implementation of predicting correlations found in the literature. From the analysis of the data, it can be seen that there is an advantageous increase in the heat transfer coefficient from the use of a micro-finned structure. However, it must be considered that there is also an increase in pressure loss compared to a smooth structure.

The convenience of using a certain solution must be considered depending on the application.

Table of Contents

Nomenclature

Latin Symbols

A	Considered Surface	$[m^2]$
c_p	Isobaric heat capacity	$\left[\frac{W}{kg \cdot K}\right]$
D, d	Considered Diameter	$[m]$
f	Friction factor	
g	Gravity force	$\left[\frac{m}{s^2}\right]$
G	Specific mass flow	$\left[\frac{kg}{s \cdot m^2}\right]$
h	Fin height	$[m]$
K	Overall heat transfer coefficient	$\left[\frac{W}{m^2 \cdot K}\right]$
L	Tube length	$[m]$
$\dot{m}$	Mass flow	$\left[\frac{kg}{s}\right]$
n	Number of fins	
n_g	Number of grooves	
p	Pressure	$\left[bar, mbar, \frac{mbar}{m}\right]$
q	Specific heat flow	$\left[\frac{W}{m^2}\right]$
Q	Heat	$[J]$
$\dot{Q}$	Heat flow	$[W]$
R	Thermal resistance	$\left[\frac{m^2 \cdot K}{W}\right]$
r	Internal radius	$[m]$
T	Temperature	[°C]
u, v, w	Fluid speed	$\left[\frac{m}{s}\right]$
x	Vapor quality	
X	Martinelli parameter	
z	General length	$[m]$

Greek Symbols

α	Heat transfer coefficient	$\left[\frac{W}{m^2 \cdot K}\right]$
β	Spiral angle of pipe	[°]
γ	Apex angle of pipe	[°]
Δ	General difference	
ε	Void Fraction	
θ	Film angle	
λ	Thermal Conductivity	$\left[\frac{W}{m \cdot K}\right]$
μ	Dynamic Viscosity	$\left[\frac{Pa}{s}\right]$
ν	Specific volume	$\left[\frac{m^3}{kg}\right]$
ρ	Density	$\left[\frac{kg}{m^3}\right]$
σ	Surface tension	$\left[\frac{N}{m}\right]$
φ	Circumferential coordinate	[°]
Φ	Phase multiplicator	

Subscripts

c	Convective condensation, Critical
cb	Convective boiling
$cond$	Condensation
$corr$	Correlation
$evap$	Evaporation
eq	Equivalent
exp	Experimental
ext	External
f	Nusselt film condensing
h	Homogeneous
i	Generic section

in	Inlet
ins	Inside
int	Internal
L	Liquid
LO	Liquid only
m	Mixture
ml	Medium logarithmic
out	Outlet
p	Propylene
ra	Non-homogeneous
r	Reduced
sat	Saturation
sub	Substance
tot	Total
tp	Average local perimeter
V	Vapor
VO	Vapor only
w	Wall

Dimensionless number

Bo	Bond number
Fr	Froude number
Nu	Nusselt number
Pr	Prandtl number
Re	Reynolds number

List of Figures

List of Tables

1 INTRODUCTION

Demand and consumption of energy in the world is growing steadily as technological and social progress are inevitably linked to an increase in energy use. Considering the environmental repercussions, the consequences are worrying, so scientific research focuses on the study of clever and alternative solutions, with particular attention to the efficiency of the physical processes involved. In the energy sector, heat exchange between fluids plays an important role, as it is involved in many processes, especially in the industrial sector. In particular, the two-phase heat exchange between liquid and vapor is studied with interest, as it is involved in the phenomena of condensation and evaporation, that occur for example inside power plants or inside refrigerating cycles. The improvement of the efficiency of this mechanism is the object of many studies and tests with different purposes, such as the reduction of the energy requirement, the reduction of the charge of fluids and the improvement of the compactness of the structures. The purpose of this work is to analyze the performances of a pure hydrocarbon condensing inside a horizontal micro-fin tube, under certain established conditions, to gain better knowledge about two-phase heat transfer and pressure losses.

Condensation occurs when an overheated fluid is cooled down by another fluid, until a change of phase happens, with the passage from the gaseous phase to the liquid phase. The liquid-vapor fluid gives rise to mechanisms that are complex to predict precisely as a wide number of configurations are possible. The classification of the two-phase regimes is relevant since the phase of the fluid is responsible for several dynamics through which heat is transmitted, so that the flow pattern gives information that determines the way the heat transfer coefficient and the pressure drops are calculated. Consequently, their identification allows the correct interpretation of the whole process.

The experiments were carried out at Institute of Technical Thermodynamics at the University of Kassel, where a facility was specially built to carry out tests in total or partial condensation, varying the operating conditions such as pressure, temperature, mass flow rate, vapor quality at the inlet of the tube test. The purpose is to analyze the data collected to understand the performance of the test section, to allow comparisons with other types of tube used, in order to find the best configuration that provides higher values of heat transfer coefficient with reasonable pressure losses. In

this work, a literature review is made to present the main scientific background to the data which are discussed in Chapter 5. An extensive description of the facility is given in Chapter 3 while data reduction is given in Chapter 4. The data collected are plotted in graphs, analyzed and commented through the comparison between the results available from literature and data collected for a smooth tube. The conclusions are provided in Chapter 6.

The present work, with all the practical tests needed, was developed at the Institute of Technical Thermodynamics of the University of Kassel (Germany) within the Erasmus exchange program of the University of Padova (Italy).

2 THEORETICAL BASIS

The processes that involve the change of phase are largely used in the industrial field, like inside vapor power plants or inside refrigerating cycles, where condensation and evaporation occur.

To get a deeper understanding of the processes it is important to clarify the characteristics of the working fluid, specifying if it is a pure substance or a mixture, because the effects during the phase change are very different in the two cases.

The purpose of this work is to analyze the performances of a pure hydrocarbon condensing inside a micro-fin tube, under certain determined conditions.

Condensation occurs when a overheated fluid is cooled down by another fluid, until a change of phase happens, with the passage from the gaseous phase to the liquid phase.

Among all the possible two-phase flows, the one that presents liquid and vapor together is the most complex, because the interface between them is deformable and the gaseous phase is compressible. As a consequence, a wide number of configurations are possible and the determination of a map to predict the exact changing process is difficult. The classification of the two-phase regimes is important because the flow pattern determines the way the heat transfer coefficient and the pressure drops are calculated. Their identification allows the correct interpretation of the whole process.

Many correlations exist in literature to calculate these two parameters. Their determination is difficult because the mechanisms are complex and many variables are involved and influence the process.

2.1 Condensation of pure gas inside horizontal tubes- flow pattern maps

The condensation proceeds gradually and, along the tube, different flow regimes can be recognized while the percentage of liquid increases. Each regime influences the heat exchange with different characteristics and, as a consequence, there is a repercussion in the definition of the heat transfer coefficient and of the amount of pressure losses.

While condensation occurs and the amount of liquid rises, an increment of the influence of the gravity force in comparison to shear stress is notable.

Many equations have been studied in literature to predict the flow regimes according to different conditions such as the geometry of the tube, its inclination, its diameter and the characteristic of the working fluid.

The most important regimes classified are briefly presented [1]:

- Single-phase vapor flow: at the entrance of the heat exchange the vapor quality is expected to be $x = 1$.
- Annular flow: the liquid flows as a film around the pipe wall, while the gas flows in the core part. Because of the presence of the gravity, in the bottom part the film is thicker than in the top part. The heat transfer is influenced by the shear stress both between the vapor and the tube wall, both between the vapor and the liquid.
- Slug flow: the amount of liquid increases and it´s present between the slugs of vapor.
- Stratified-wavy flow: gas velocity is very high compared to the liquid one, therefore the shear stress on the interface is dominant. The vapor interacts with the liquid surface and it provides the formation of waves on it.
- Stratified flow: gas velocity is lower, the flow is gravity driven. The vapor flows in the upper part of the tube due to the lower density of the gaseous phase, while the liquid flows in the bottom part. A well-defined separation is evident between the two fluids.
- Bubble flow: vapor phase occurs just as little bubbles dispersed in the liquid, which flows with higher velocity.

A simple representation can be visualized in Figure 2.1.

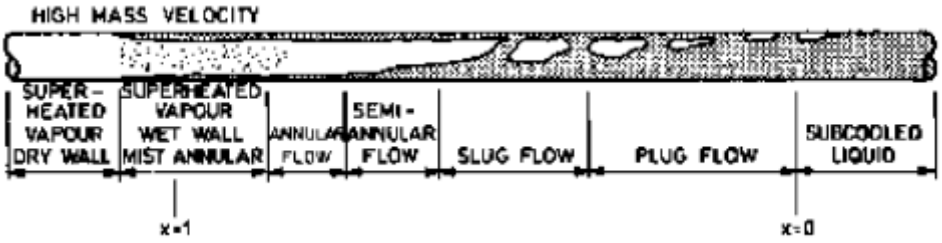

Figure 2.1: Flow regimes during condensation

An effective visualization and calculation of the different regimes is possible through the utilization of the flow pattern maps, anyone made according to the specific case of study.

The most used map was implemented by Taitel and Dukler [2] using the definition of some parameters that allowed the prediction of five flow regimes.

The parameters are defined taking account of the geometrical characteristics of the tube such as its diameter D, the inclination angle β and taking account of the fluid properties like the density of the fluid both for the liquid phase ρ_L and for the gas phase ρ_G.

$$X = \left[\frac{\left(-\frac{dp}{dz}\right)_L}{\left(-\frac{dp}{dz}\right)_G}\right]^{0.5} \tag{2.1}$$

X is called Martinelli parameter, defined as the ratio between the pressure gradient of the liquid and gas phase, considering they both flow as a single phase along the tube length.

$$K = \left[\frac{J_G^2\ \rho_G\ D\ J_L}{g\ D\cos(\beta)\ (\rho_L - \rho_G)u_L}\right]^{0.5} \tag{2.2}$$

$$F = \frac{G\ x}{\sqrt{g\ D\cos(\beta)\ (\rho_L - \rho_G)}} \tag{2.3}$$

$$T = \left[\frac{\left(-\frac{dp}{dz}\right)_L}{g\cos(\beta)\ (\rho_L - \rho_G)}\right]^{0.5} \tag{2.4}$$

The Figure 2.2 shows the flow pattern map for horizontal pipe flows, in which the different regions are defined by the transition lines.

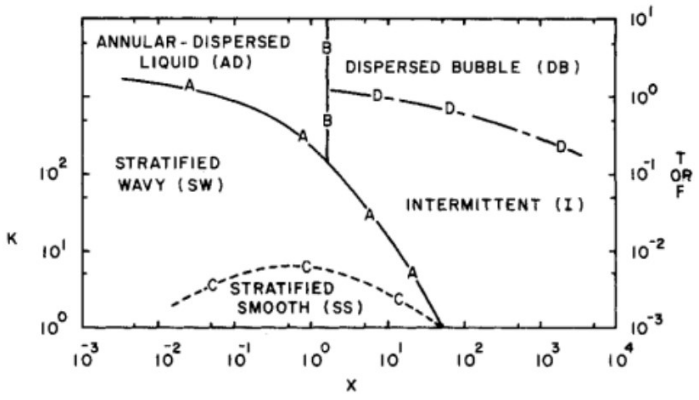

Figure 2.2: Taitel and Dukler flow pattern map [2]

- Line A: definition between wavy stratified and intermittent or annular regime.
- Line B: transition between annular and intermittent flow.
- Line C: transition between stratified wavy and stratified sooth.
- Line D: transition between dispersed bubble and intermittent.

Many other correlations have been implemented over the years for predicting the two-phase flow regime into horizontal tubes. Each result has been obtained considering specific working conditions, geometrical aspects and a well-defined type of fluids suitable for the case of study. The last point is particularly interesting considering that not all the fluids react in the same way despite being subject to the same boundary conditions.

Thome et al. [3] proposed a new map taking advantage of new flow pattern maps introduced in the latest years, taking account of the data collected for seven different refrigerants.

Their study is based on the void fraction model for predicting the cross-sectional area occupied by the vapor with respect to the total cross-sectional area of the flow channel, taking account of different classifications, such as:

- Homogeneous model, where it is supposed liquid and vapor fractions flows with the same velocities.
- One-dimensional model.
- Drift flux models.
- Models for specific flow regimes.
- Empirical methods.

The purpose of their research was focused on the determination of the void fraction, reliable over the whole range of the mass velocities, flow regime and reduced pressure, to permit an accurate calculation of the heat transfer coefficient in wide range of conditions. The best result was obtained implementing a logarithmic mean void fraction between the homogeneous ε_h and the non-homogeneous ε_{ra} void fraction, as follow:

$$\varepsilon = \frac{\varepsilon_h - \varepsilon_{ra}}{\ln\left(\frac{\varepsilon_h}{\varepsilon_{ra}}\right)} \tag{2.5}$$

For the construction of the flow pattern map, the definition of the mass velocities involved is required:

- G_{wavy} is the wavy flow transition mass velocity, A_{Vd} the dimensionless vapor cross-sectional area, h_{Ld} dimensionless liquid height, x the vapor quality, We Weber number and Fr the Froude number.

$$G_{wavy} = \left\{\frac{16A_{Vd}^3 g d \rho_L \rho_V}{x^2\pi^2(1-(2h_{Ld}-1)^2)^{0.5}}\left[\frac{\pi^2}{25\,h_{Ld}^2}\left(\frac{We}{Fr}\right)_L^{-1.023}+1\right]\right\}^{0.5} + 50 - 75e^{-\frac{(x^2-0.97)^2}{x(1-x)}} \tag{2.6}$$

- G_{strat} is the stratified flow transition mass velocity and A_{Ld} dimensionless liquid cross-sectional area.

$$G_{strat} = \left\{\frac{226.3^2 A_{Vd}^2 A_{Ld} \rho_V (\rho_L - \rho_V)\mu_L g}{x^2(1-x)\pi^3}\right\}^{1/3} + 20x \tag{2.7}$$

- X_{IA} is the intermittent to annular flow transition quality.

$$X_{IA} = \left\{\left[0.2914\left(\frac{\rho_V}{\rho_L}\right)^{-1/1.75}\left(\frac{\mu_L}{\mu_V}\right)^{-1/7}\right]+1\right\}^{-1} \tag{2.8}$$

- G_{mist} is the mist flow transition mass velocity and ξ a factor.

$$G_{mist} = \left\{ \frac{7680 A_{Vd}^2 g d \rho_V \rho_L}{x^2 \pi^2 \xi} \left(\frac{Fr}{We} \right)_L \right\}^{0.5} \tag{2.9}$$

- G_{bubbly} is the bubbly flow transition mass velocity and P_{id} is a dimensionless parameter of interface.

$$G_{bubbly} = \left\{ \frac{256 A_{Vd} A_{Ld}^2 d^{1.25} \rho_L (\rho_L - \rho_V) g}{0.3164 (1-x)^{1.75} \pi^2 P_{id} \mu_L^{0.25}} \right\}^{1/1.75} \tag{2.10}$$

The following criteria for the determination of the regime limits are applied, under the hypothesis of considering a fixed value of G in the range of interest.

- Annular flow: $G > G_{wavy};\ \ G < G_{mist};\ \ x > x_{IA}$
- Intermittent flow: $G > G_{wavy};\ \ G < G_{mist}\ or\ G < G_{bubbly};\ \ x < x_{IA}$
- Stratified wavy flow: $G_{strat} < G < G_{wavy}$
- Fully stratified: $G < G_{strat}$
- Mist flow: $G > G_{mist}$

The final analysis of the new method proposed allows to verify its reliability compared to the other flow pattern maps considered by Tandon et al. [4], Sardasei et al. [5], Dobson and Chato [6], Kattan et al. [7].

2.2 Condensation inside micro-fin tubes

The micro-fin tubes are enhanced surfaces largely used in condensation processes. The heat transfer is particular efficient because the micro-fins represent an increment of the heat transfer area and, at the same time, their presence allows to increase the turbulence of the system. Both of these two elements positively influence the heat exchange. As a disadvantage, a gain in the pressure losses value is noticeable, mainly due to the interference between the flow and the structures.

Making a comparison between enhanced and smooth structures, the advantage in using micro-fin tube is visible. In fact, the heat transfer coefficient increases much more than the pressure losses.

From definition, for micro-fin tubes the ratio between the height of the fin and the diameter of the tube is lower than 0.04 [8].

The increase of the heat transfer is possible with a combination of the liquid-vapor interface mixing and turbulent mixing near the wall. The surface tension drainage and swirl effects are presumed to have little influence on the heat transfer enhancement [9]. Yang and Webb [10] assume the surface tension force enhances the condensation coefficient when the fin tips are not flooded by condensate, and this occurs especially when the mass velocity is low and the vapor quality is low. At high mass velocity, the flow is vapor shear dominated and surface tension is less effective. [9]

As a consequence of these characteristics, an increase in the efficiency of the heat exchange is noticeable, and this permits to reduce the dimension of the structures used and the charge of the fluid employed. The last point presented is particularly crucial, considering the current interest in the reduction of the amount of fluid charge, for example into the refrigerating industry. This interest is driven by the increasing concern related to the effect of the Global Warming Potential GDP and Ozone Depletion Potential ODP into the atmosphere. The European environmental standards are becoming much stricter requiring to phase out the use of potentially polluting substances.

The micro-fin tubes can be categorized into different classes. In this work are considered helical micro-fin tubes, cross-grooved tubes and herringbone tubes.

As concern the helical micro-fin tubes, the increase of the heat exchange is provided both by the enhance of the exchange surface and by the particular geometry of the fins that promotes the turbulence during annular flow. The drainage of the condensate is fostered by the surface tension of the liquid phase.

The increase of the pressure drop is attributed by the raise of the vapor velocity in a helical micro-fin tube, due to the huger size of the regions of annular flow, which increases the turbulence of the flow inside the length, compared to a smooth tube [11].

The presence of the fins permits the redistribution of the liquid layer around the circumference of the tube, forcing the flow to become annular instead of intermittent or stratified.

In Figure 2.3 an example of the geometry and of some typical values of the geometrical parameters is shown [12].

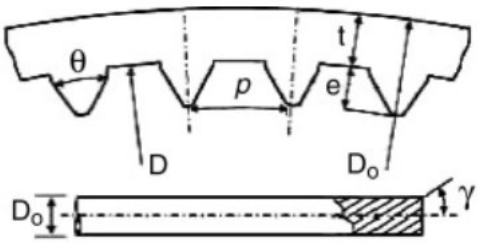

fin tip angle	θ	25°
helix angle	γ	15°
outside diameter	D_o	9.52 mm
inside diameter	D	8.92 mm
fin height	*e*	0.25 mm
wall thickness	t	0.30 mm
fin pitch	p	0.48mm
number of fins	n	55

Figure 2.3: Geometry of micro-fin tube. [12]

As concern the cross-grooved tube, it presents an additional set of grooves at the same spiral angle but with an opposite angular direction and, in general, a different depth [9]. This kind of tube is more performant than the micro-fin tubes. A comparison between the two types is shown in Figure 2.4.

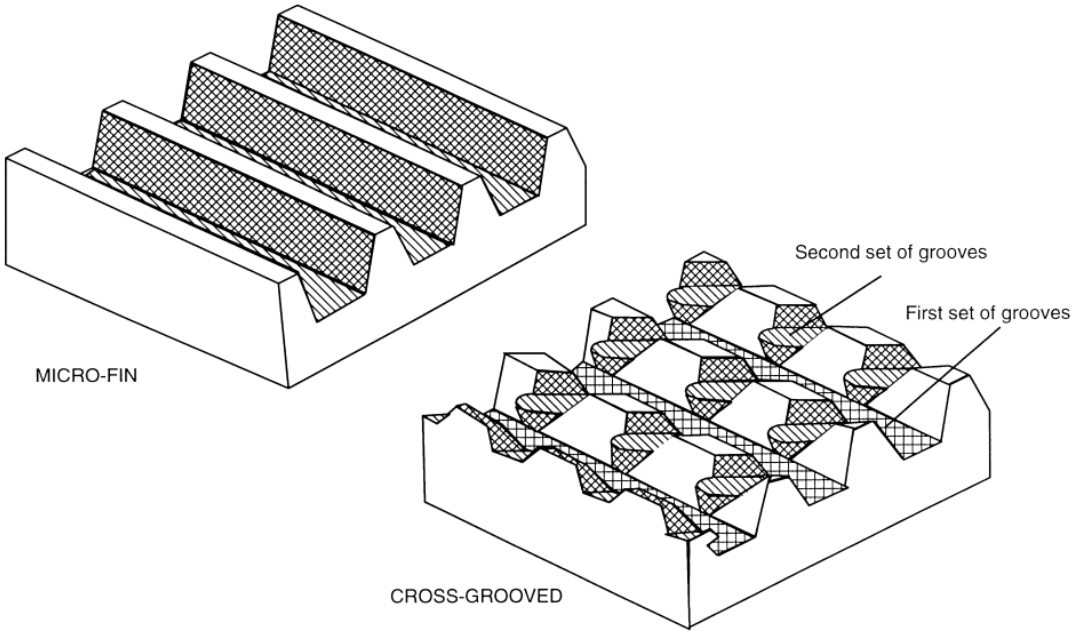

Figure 2.4: Comparison between micro-fin and cross-grooved surfaces. [9]

In the 1990s a new generation of micro-fin tube was developed, called herringbone tube [11]. The characteristic structure of this tube consists of a double chevron-shaped tube, with embossed micro-fin, as shown in Figure 2.5.

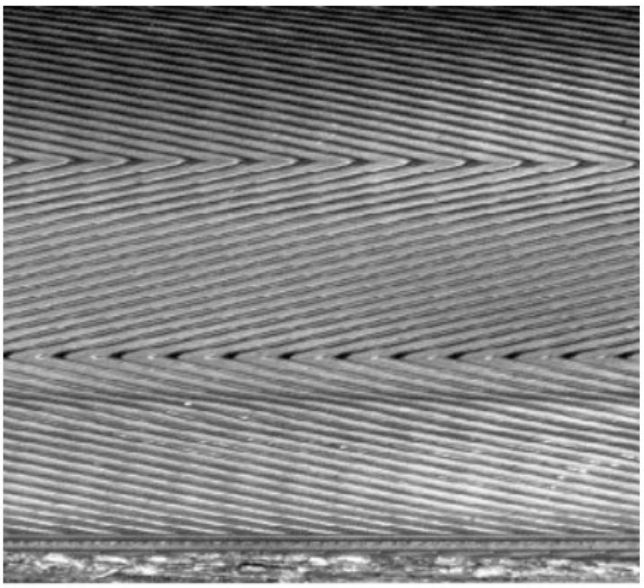

Figure 2.5: Picture of herringbone tube. [11]

A comparison between herringbone and helical structure is shown in figure 2.6 [13].

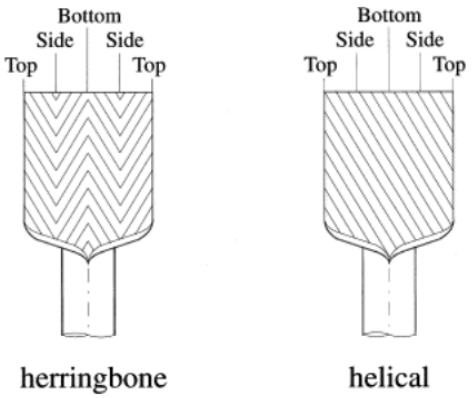

Figure 2.6: Comparison between herringbone and helical structures. [13]

Miyara et al. [13] made some condensation tests with R410A and R22, comparing the value of the heat transfer coefficient and of the pressure drop between helical micro-fin tube and herringbone tube. They reported that the heat transfer coefficient and the pressure drop is higher in herringbone tube than in helical micro-fin tubes in

the high mass velocity region, while they are lower or equal in the low mass velocity region [9].

Despite the numerous advantages, the use of micro-fin tubes can provide some problems if not correctly maintained. In fact, the presence of fouling can be responsible of a huge decrease in the properties. In general, the fouling problem is much more serious for liquids than for gases [14].

2.3 Correlations

The determination of the heat transfer coefficient and of the pressure losses are fundamental for the correct and efficient design of the condenser.

Before any calculations can be made, it is necessary to highlight that the heat transfer coefficient and the friction factor of the enhanced tube are function of the type of flow and of the geometrical conditions. These two characteristics for condensation on enhanced surfaces depend on the following variables [14]:

- Geometry: the tube diameter and the specific geometric features of the enhanced surface
- The operating pressure or saturation temperature
- The mass velocity, the vapor quality and the heat flux or the wall-to-fluid temperature difference

2.3.1 Heat transfer coefficient

A heat flux is generated when a fluid flows in a tube and a temperature difference occurs. It takes place through the interface between the two mediums that behave like thermal resistances, in a way that is proportional to the extension of the surface involved. The specific heat flux per area unit is proportional to the value of the heat transfer coefficient α [W/(K*m^2)], that is the reciprocal of the specific thermal resistance:

$$\dot{q} = \frac{Q}{A} = \frac{T_{wall} - T_{fluid}}{R} = \alpha \cdot \left(T_{wall} - T_{fluid}\right) \tag{2.12}$$

The heat transfer coefficient

$$\alpha = f(\lambda, \rho, c_p, \mu, L, w) \tag{2.13}$$

is strongly related to many parameters, and this characteristic makes its definition particularly complex.

With:

- λ: Thermal conductivity $[W/(m \cdot K)]$
- ρ: Density $[kg/m3]$
- c_p: Isobaric specific heat $[kJ/(kg \cdot K)]$
- μ: Dynamic Viscosity $[kg/(m \cdot s)]$
- L: Characteristic length $[m]$
- w: Fluid speed $[m/s]$

Taking account of all influences, it is possible to determine the number of dimensionless parameters which can describe the velocity and temperature fields. The parameters are:

- Nusselt number Nu

$$Nu = \alpha \cdot \frac{L}{\lambda} \tag{2.14}$$

- Reynolds number Re

$$Re = \frac{\rho w L}{\mu} \tag{2.15}$$

- Prandtl number Pr

$$Pr = \frac{c_p \mu}{\lambda} \tag{2.16}$$

In literature numerous empirical or semi-empirical correlations exist to calculate the heat exchange coefficient, each of them is specific and suitable for determinate conditions and case of study.

In the present work, a comparison between the correlations implemented for smooth and micro-fin tubes are presented:

- As concern smooth tubes, Thome et al. [15] and Shah [16] equations are used.
- As concern enhanced tubes, Cavallini [17] and Yu and Koyama [18] equations and Olivier et al. [19] are used.

Thome and al. [15] considered 15 fluids, including some common refrigerants and some pure hydrocarbons and a wide range of test conditions to propose a new condensation model, distinguish between stratified and annular regimes.

During the annular flow, the liquid film thickness is assumed to be δ.

During fully stratified flow, Thome considered the liquid distributed as a truncated annular ring of uniform thickness δ in the bottom part of the tube, as shown in Figure 2.7.

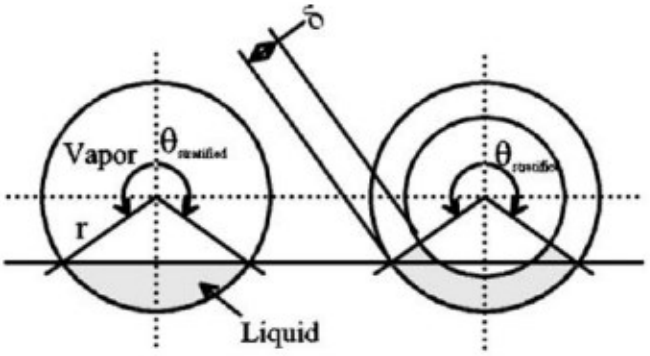

Figure 2.7: Simplified flow structure for stratified flow [15]

The upper angle of the tube not wetted by stratified liquid is called θ, while θ_{strat} is the stratified angle around upper perimeter of the tube.

The phenomenon of the convective condensation (α_c) is applied to the perimeter wetted by the axial flow of liquid film. In annular flows, this refers to the entire perimeter, while in stratified flow it refers only to a part.

The film condensation coefficient (α_f) is applied to the upper perimeter of the tube in stratified flows. It is obtained applying the Nusselt falling film theory to the inside of the horizontal tube. The Figure 2.8 shows a schematic representation.

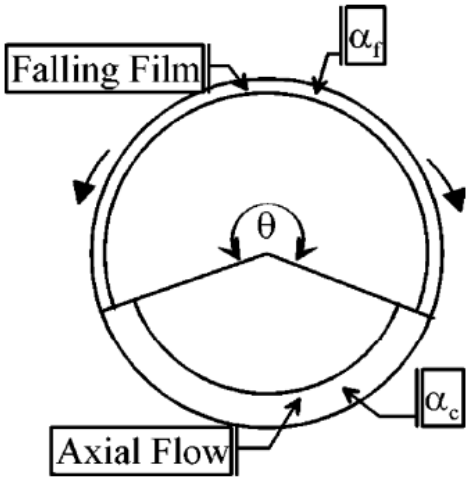

Figure 2.8: heat transfer model showing convective and falling film boundaries [15]

The general expression for the local condensing heat transfer coefficient α_{tp} is:

$$\alpha_{tp} = \frac{\alpha_f r\theta + (2\pi - \theta) r\alpha_c}{2\pi r} \tag{2.17}$$

Where:

- r: internal radius of the tube
- θ: falling film angle around the top perimeter of the tube

It is evident that for annular flow $\theta = 0$, and therefore $\alpha_{tp} = \alpha_c$, while for fully stratified flow $\theta = \theta_{strat}$.

The angle θ is obtained by assuming a quadratic interpolation:

$$\theta = \theta_{strat}\left[\frac{(G_{wavy} - G)}{(G_{wavy} - G_{strat})}\right]^{0.5} \tag{2.18}$$

In the above equation, G_{wavy} and G_{strat} are determined by the equations in the flow pattern map.

The convective condensation heat transfer coefficient is obtained from the turbulent film equation, where m and n are exponents based respectively on Pr_L and on Re_L:

$$\alpha_c = cRe_L^n Pr_L^m \frac{\lambda_L}{\delta} f_i \tag{2.19}$$

The interfacial roughness correction factor f_i is determined as follow:

$$f_i = 1 + \left(\frac{u_V}{u_L}\right)^{1/2} \left(\frac{(\rho_L - \rho_V) g \delta^2}{\sigma}\right)^{1/4} \tag{2.20}$$

The film condensation heat transfer coefficient α_f is obtained from the theory of Nusselt for laminar flow of a falling film on the internal perimeter of the tube:

$$\alpha_f = 0.728 \left[\frac{\rho_L(\rho_L - \rho_V) g h_L {\lambda_L}^3}{\mu_L d(T_{sat} - T_w)}\right]^{1/4} \tag{2.21}$$

Shah [16] considered three different regimes and, for each one, a different value of the two-phase heat transfer coefficient α_{TP}

$$\text{Regime I:} \quad \rightarrow \quad \alpha_{TP} = \alpha_I \tag{2.22}$$

$$\text{Regime II:} \quad \rightarrow \quad \alpha_{TP} = \alpha_I + \alpha_{Nu} \tag{2.23}$$

$$\text{Regime III:} \quad \rightarrow \quad \alpha_{TP} = \alpha_{Nu} \tag{2.24}$$

The parameters are expressed as follow:

$$\alpha_I = \alpha_{LO} \cdot \left(1 + \frac{3.8}{Z^{0.95}}\right) \left(\frac{\mu_L}{14\mu_G}\right)^{(0.0058 + 0.557 \cdot pr)} \tag{2.25}$$

$$\alpha_{LO} = 0.023 \cdot {Re_{LO}}^{0.8} \cdot Pr_L^{0.4} \cdot \frac{\lambda}{D} \tag{2.26}$$

$$Z = \left(\frac{1}{x} - 1\right)^{0.8} {p_r}^{0.4} \tag{2.27}$$

$$\alpha_{Nu} = 1.32 \cdot {Re_{LO}}^{-1/3} \left[\frac{\rho_L(\rho_L - \rho_G) g \cdot {\lambda_L}^3}{{\mu_L}^2}\right]^{1/3} \tag{2.28}$$

As concern structured tubes, Cavallini et al. [17] reviewed some correlations for low-fin, micro-fin and cross-grooved tubes and provided their presentation.
Yu and Koyama [18] developed a correlation for micro-fin tubes, defined as follow:

$$\varepsilon^{-1} = 1 + \left[\frac{(1-x)\rho_G}{x \cdot \rho_L}\right]\left\{0.4 + \frac{0.6\left[x\left(\frac{\rho_L}{\rho_G}\right) + 0.4(1-x)\right]^{0.5}}{[x + 0.4(1-x)]^{0.5}}\right\} \quad (2.29)$$

$$H = \varepsilon + \{10(1-\varepsilon)^{0.1} - 8\}\varepsilon^{0.5}(1-\varepsilon^{0.5}) \quad (2.30)$$

$$Nu_B = 0.725 \cdot H \cdot \left[\frac{Ga \cdot Pr_L}{Ph_L \cdot \eta_A}\right]^{0.25} \quad (2.31)$$

$$\Phi_G = 1.1 + 1.3\left\{\frac{G^{0.35}X_{tt}^{0.35}}{[g \cdot d_M \cdot \rho_G(\rho_L - \rho_G)]^{0.175}}\right\} \quad (2.32)$$

$$Nu_F = 0.152\left(\frac{\Phi_G}{X_{tt}}\right)Re_L^{0.68}(0.3 + 0.1Pr_L^{1.1}) \quad (2.33)$$

$$Nu = \sqrt{Nu_F^2 + Nu_B^2} \quad (2.34)$$

Cavallini et al. [17] provided a correlation for low-fin, micro-fin and cross-grooved tubes, depending on the value attributed to some constant, experimentally defined.

$$Re_{eq} = 4M\frac{(1-x) + x\left(\frac{\rho_L}{\rho_G}\right)^{1/2}}{\pi \cdot d \cdot \mu_L} \quad (2.35)$$

$$Rx = \left\{\frac{\left[2 \cdot h \cdot n_g(1 - \sin\left(\frac{\gamma}{2}\right)\right]}{\left[\pi \cdot d \cdot \cos\left(\frac{\gamma}{2}\right)\right]} + 1\right\} / \cos(\beta) \quad (2.36)$$

$$Bo = \frac{g \cdot \rho_L \cdot h \cdot \pi \cdot d}{8 \cdot \sigma \cdot n_g} \quad (2.37)$$

$$Nu = 0.05Re_{eq}^{0.8}Pr_l^{\frac{1}{3}}(Bo \cdot Fr)^t Rx^s \quad (2.38)$$

Olivier et al. [19] adapted the correlations from literature for herringbone and helical micro-fin tubes to provide equations for application in annular and intermittent flow.

$$Re_{eq} = 4M\frac{(1-x) + x\left(\frac{\rho_L}{\rho_G}\right)^{1/2}}{\pi \cdot d_i \cdot \mu_L} \quad (2.39)$$

$$Rx = \left\{ \frac{2 \cdot h \cdot n \left[1 - \sin\left(\frac{\gamma}{2}\right)\right]}{\pi d_i \cos\left(\frac{\gamma}{2}\right)} + 1 \right\} (cos\beta)^{-1} \tag{2.40}$$

$$Bo = \frac{g \cdot \rho_L \cdot h \cdot \pi \cdot d_i}{8 \cdot \sigma \cdot n} \tag{2.41}$$

$$Fr = \frac{u_{vo}^2}{g \cdot d_i} \tag{2.42}$$

$$TF = (1 - x) + x^{1.3} \tag{2.43}$$

$$\begin{gathered} s = 0.715 \; for \; herringbone \; tubes \\ s = 0.700 \; for \; helical \; micro - fin \; tubes \end{gathered} \tag{2.44}$$

$$\alpha = \frac{\lambda_L}{d_i} 0.05 Re_{eq}^{s} Pr_L^{\frac{1}{3}} TF (Rx)^2 (Bo \cdot \ln(Fr))^{-0.26} \tag{2.45}$$

It is evident how the correlations implemented for micro-fin tubes have to take account of the particular geometry of the fins.

2.3.2 Pressure Drop

Pressure drop for two-phase fluid is more complex to predict in comparison with one-phase pressure drop, because many effects related to the change of phase occur. Different flow regimes come in succession and, consequently, a discontinuity in the flux is generated. Normally, the calculations try to simplify the process, considering a continuous flow instead of a discontinuous flow. Moreover, a distinguish between homogeneous models and non-homogeneous models can be done. The first ones assume that the velocity of both gas and liquid phase is equal, and this consideration allows to suppose the fluid acts like a single-phase flow. In this case, the correlations for the single-phase fluid can be used, taking account of the mean values of fluid characteristics and velocities of both phases.

The heterogeneous models consider the two phases flowing separately at different velocity along the tube. To simplify the calculation, normally constant characteristic are assumed for both phases.

The two-phase pressure drop accounts for three contributions: static pressure change, momentum pressure change and friction pressure drop:

$$\Delta p_{total} = \Delta p_{static} + \Delta p_{momentum} + \Delta p_{friction} \tag{2.46}$$

Considering horizontal tubes, $\Delta p_{static} = 0$.

Similarly to what is already shown for the heat transfer coefficient, in literature numerous correlations to calculate the pressure drops are available, each of them suitable for certain conditions and case of study.

In the present work, a comparison between the correlations implemented for smooth and micro-fin tubes are presented:

- As concern smooth tubes, Friedel [20] and Müller et al. [21] equations are used.
- As concern enhanced tubes, Cavallini et al. [22], Haraguchi et al. [23] and Olivier et al. [19] equations are used.

Müller et al. [21] suggested a simple method that passes through the definition of both pressure drops for liquid and gaseous phase.

$$If\ Re\ \leq\ 1187 \rightarrow\ \zeta = \frac{64}{Re} \tag{2.47}$$

$$If\ Re > 1187\ \rightarrow\ \zeta = \frac{0.3164}{Re^{\frac{1}{4}}} \tag{2.48}$$

$$\Delta p_{1-phase} = \frac{\zeta \cdot G^2}{2 \cdot D \cdot \rho} \tag{2.49}$$

$$K = \Delta p_{1-phase,fluid} + 2 \cdot (\Delta p_{1-phase,gaseous} - \Delta p_{1-phase,fluid}) \cdot x \tag{2.50}$$

$$\Delta p_{2-phases} = K \cdot (1-x)^{1/3} + \Delta p_{1-phase,gaseous} \cdot x^3 \tag{2.51}$$

Friedel [19] implemented his method involving the definition of more parameters, as it is shown below:

$$if\ Re\ \leq\ 1055 \rightarrow\ \zeta = \frac{64}{Re} \tag{2.52}$$

$$if\ Re > 1187\ \rightarrow\ \zeta = \left[0.86859 \cdot \log\left(\frac{Re}{1.964 \cdot log(Re) - 3.8215}\right)\right]^2 \tag{2.53}$$

$$A = (1-x)^2 + x^2 \cdot \left(\frac{\rho_L \cdot \zeta_G}{\rho_G \cdot \zeta_L}\right) \tag{2.54}$$

$$\rho_{2-phases} = \frac{1}{\frac{x}{\rho_G} + \frac{(1-x)}{\rho_L}} \tag{2.55}$$

$$R = A + 3.43 \cdot x^{0.685} \cdot (1-x)^{0.24} \cdot \left(\frac{\rho_L}{\rho_G}\right)^{0.8} \left(\frac{\mu_G}{\mu_L}\right)^{0.22} \left(1 - \frac{\mu_G}{\mu_L}\right)^{0.89} {Fr_L}^{-0.047} \cdot {We_L}^{-0.0334} \tag{2.56}$$

$$\Delta p_{1-phase} = \frac{\zeta \cdot G^2}{2 \cdot D \cdot \rho} \tag{2.57}$$

$$\Delta p_{2-phases} = \Delta p_{1-phase,gas} \cdot R \tag{2.58}$$

Cavallini et al. [22] developed a method for both micro-fin and cross-grooved tubes. The first step of the analysis is based on the definition of the type of flow and, consequently, on the frictional factor that has to be used, both for liquid and gaseous phases.

$$Turbulent\ flow\ \ \rightarrow\ \ f_1 = 0.079 \cdot \left(\frac{G \cdot D}{\mu}\right)^{-0.25} \tag{2.59}$$

$$Laminar\ flow\ \ \rightarrow\ \ f_2 = \frac{16}{\left(\frac{G \cdot D}{\mu}\right)} \tag{2.60}$$

$$f = \max(f_1, f_2) \tag{2.61}$$

Then the definition of some parameters is shown:

$$E = (1-x)^2 + x^2 \left(\frac{\rho_L \cdot f_G}{\rho_G \cdot f_L}\right) \tag{2.62}$$

$$F = x^{0,78} \cdot (1-x) \cdot 0.224 \tag{2.63}$$

$$H = \left(\frac{\rho_L}{\rho_G}\right)^{0.91} \left(\frac{\mu_G}{\mu_L}\right)^{0.19} \left(1 - \frac{\mu_G}{\mu_L}\right)^{0.7} \tag{2.64}$$

$$\rho_m = \frac{\rho_L \cdot \rho_G}{x \cdot \rho_L + (1-x)\rho_G} \tag{2.65}$$

$$\Phi_{LO}^2 = E + \frac{3.23 \cdot F \cdot H}{Fr^{0.045} \cdot We^{0.035}} \tag{2.66}$$

With the parameters described, the definition of the adiabatic pressure drop is possible, considering no change of the vapor title along the length of the tube.

$$\Delta p_{adiabatic} = \frac{\Phi_{LO}^2 \cdot 2 \cdot f_L \cdot G^2}{D \cdot \rho_L} \tag{2.67}$$

The effective value of pressure drop takes also account of other corrective factors, as explained successively:

$$G_c = M \cdot \frac{\frac{dx}{dz}}{\pi \cdot \left(\frac{D}{2}\right)^2} \tag{2.68}$$

$$if\ \varepsilon > 0.1 \quad \rightarrow \quad C_o = 1 + 0.2(1-x)\left[\frac{g \cdot D \cdot \rho_L^2}{G^2}\right]^{1/4} \tag{2.69}$$

$$if\ \varepsilon \rightarrow 0 \quad \rightarrow \quad C_o = 0 \tag{2.70}$$

$$\varepsilon = (x\rho_L) / \left\{C_o[x \cdot \rho_L + (1-x)\rho_G] + (\rho_L \rho_G u_{g_j})/G\right\} \tag{2.71}$$

$$u_{g_j} = 1.18(1-x)[\sigma \cdot g(\rho_L - \rho_G)/\rho_L^2]^{1/4} \tag{2.72}$$

$$\tau_I = \Delta p_{adiabatic} \cdot u_G \cdot \frac{D}{4} \tag{2.73}$$

$$\Phi_F = -\frac{G_c u_G}{\tau_I} \tag{2.74}$$

$$\Theta = \frac{\Phi_F}{\exp(\Phi_F) - 1} \tag{2.75}$$

$$\Delta p_{condensation} = \Delta p_{adiabatic} \cdot \Theta \tag{2.76}$$

Haraguchi et al. [23] implemented a correlation that involves the Lockhart-Martinelli parameter and two constants, experimentally determined.

$$C_1 = 1.1;\ C_2 = 1.3 \tag{2.77}$$

$$\Phi_G = C_1 + C_2 \left\{ \frac{G \cdot X_{tt}}{[g \cdot D_m \cdot \rho_G(\rho_L - \rho_G)]^{0.5}} \right\}^{0.35} \tag{2.78}$$

$$\left(\frac{dp}{dz}\right)_f = \Phi_G^2 \cdot 2 \cdot f_G \frac{(G \cdot x)^2}{D \cdot \rho_G} \tag{2.79}$$

Olivier et al. [19] developed a two-phase multiplier-type of pressure correlation for the helical micro-fin and herringbone tubes.

$$\frac{A}{A_n} = 1 - \frac{2 \cdot h \cdot n \cdot t}{\pi \cdot d_i^2 \cdot cos\beta} \tag{2.80}$$

$$f_{lo} = 0.046 \cdot Re_L^{-0.2} \left(\frac{d_i}{d_{eq}}\right)^{-1} \left(\frac{A}{A_n}\right)^{-0.5} (2sec\beta)^{1.1} \tag{2.81}$$

$$\Delta p_{lo} = \frac{2 f_{lo} G^2 (1 - x)^2 L}{\rho_L d_i} \tag{2.82}$$

$$\Phi_L^2 = 1.376 + \frac{7.242}{X_{tt}^{1.655}} \tag{2.83}$$

$$\Delta p_f = \Delta p_{lo} \Phi_L^2 \tag{2.84}$$

.

3 EXPERIMENTAL SETUP

In this chapter the main components of the test rig are described.

3.1 Test Facility

The KIIR test rig was built by the Thermodynamic department of University of Kassel to run different experimental tests regarding the condensation process. The tests are implemented setting the operative parameters, then some measurements are made and the data are collected and analyzed. The main focus is on the determination of the pressure losses and on the calculation of the heat transfer coefficient.
For each experiment, the pressure and temperature values can be changed, such as the type of working fluid and the test tube, to analyze the influence of different structures on the condensation process.
The facility, schematically represented in Figure 3.1, consists in different parts:

- A primary cycle, which includes the test section
- A bypass cycle
- Four secondary cycles, one of them involved in the test section.

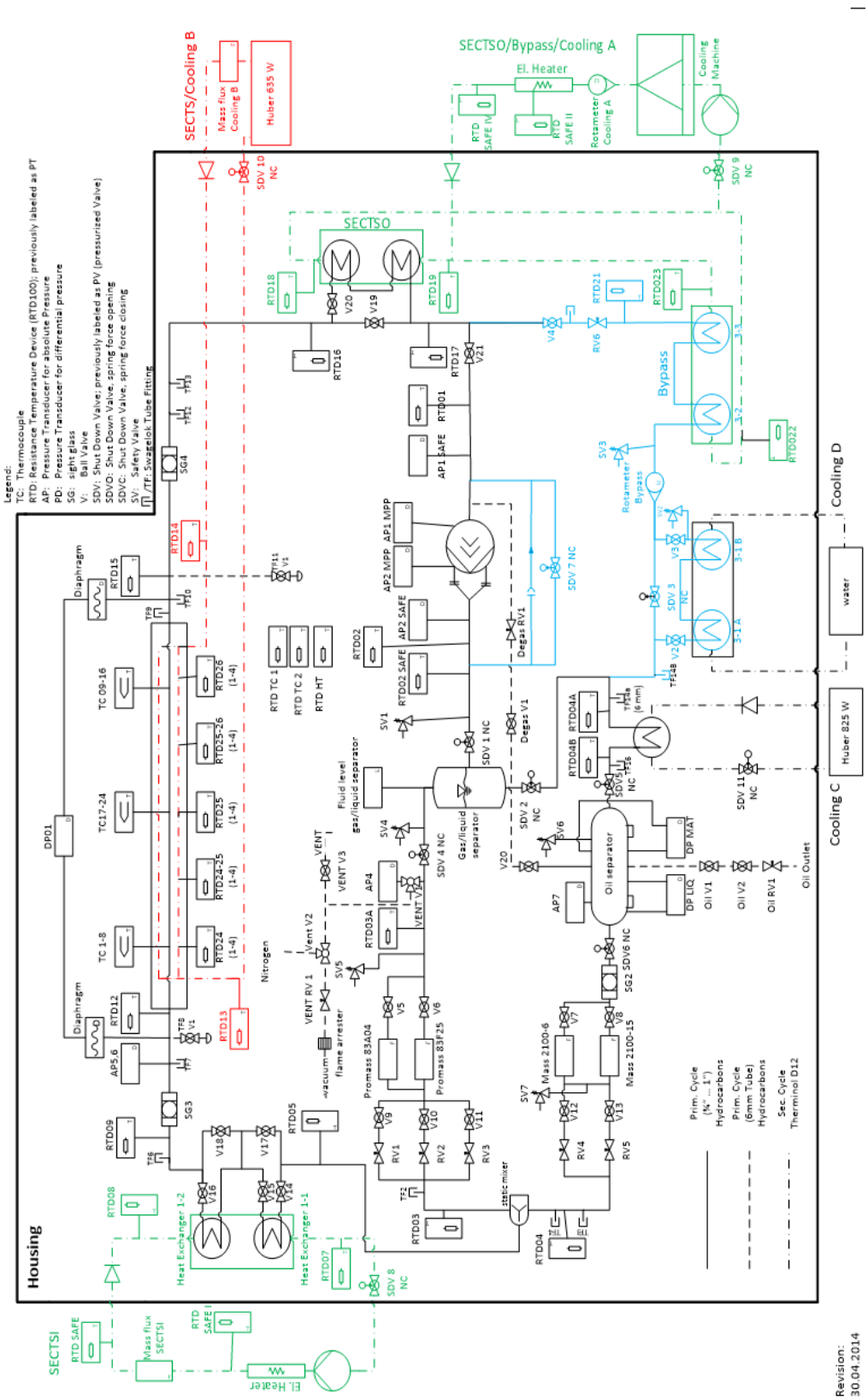

Figure 3.1: Schematic representation of the facility

Figure 3.2 provides a 3D representation of the main components of the circuit.

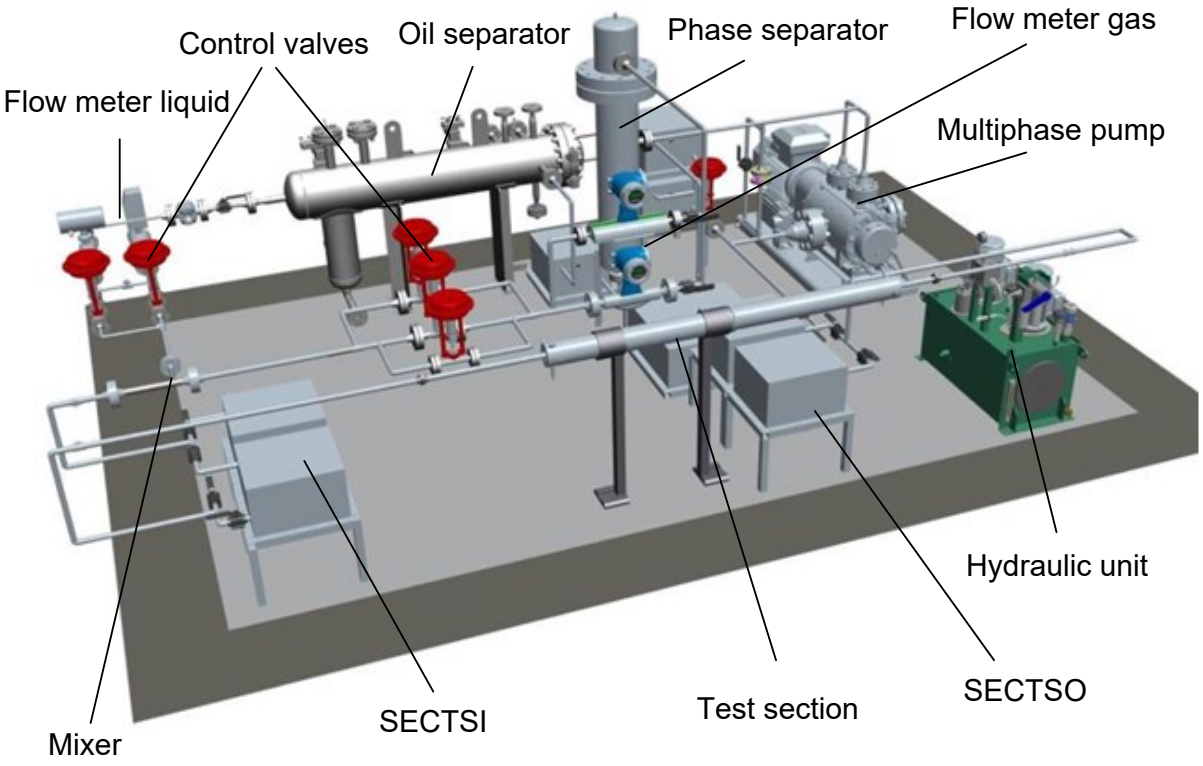

Figure 3.2: 3D representation of the main components of the circuit

3.1.1 Primary Cycle

The primary cycle is the core part of the whole facility, where the test section is located and the data resulted from the condensation process are collected.

In the primary cycle the operative parameters are set and checked through the sensors positioned along the whole circuit.

A schematic representation of the system is presented in Figure 3.3, and the denomination of the main components is reported in Table 3.1.

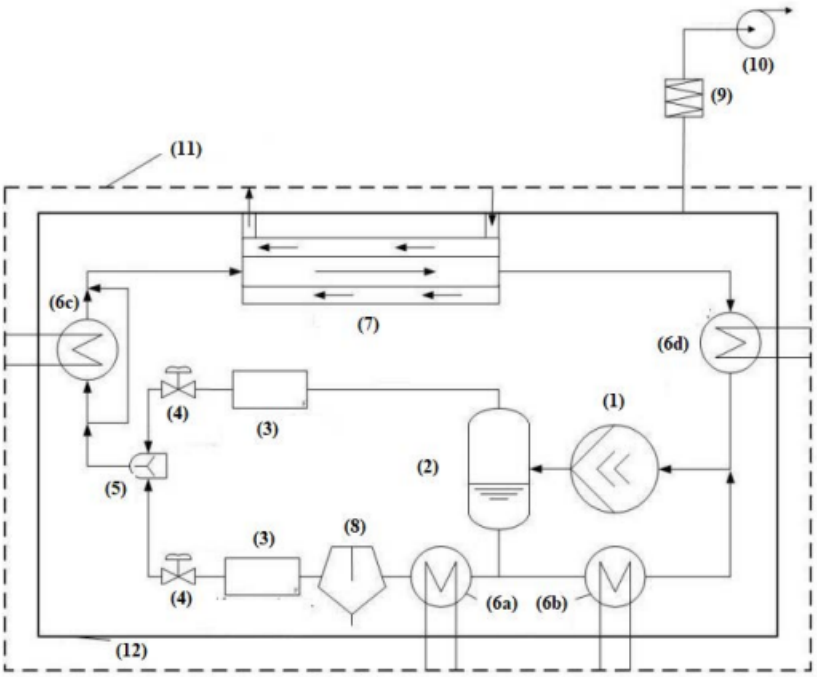

Figure 3.3: Schematic representation of the primary cycle

Name	Denomination of the components
1	Multi-phase pump
2	Phase separator
3	Mass flow meters
4	Control valve
5	Static mixer
6	Heat exchanger
7	Measuring section
8	Oil separator
9	Activated carbon filter
10	Ventilator
11	Secondary circuit
12	Protection case

Table 3.1: Denomination of the main components of the primary cycle

The working fluid is pumped in the cycle through a multi-phase pump (1). It is a specially developed prototype screw pump for low-viscosity fluids that properly works under four precise conditions:

- To avoid cavitation, the suction pressure has to be higher than 0.5 bar.
- Due to mechanical limitations, the pressure difference between suction and discharge ports has to be lower than 10 bar.
- To avoid overheating during the compression, the mass-based gas content at suction has to be higher than 94%.
- The rotational speed range is between 400 and 1500 rpm. Varying the velocity, the volumetric flow rate in the primary cycle can be changed.

After the pump, the fluid is sent to the phase separator (2), where the liquid is divided from the gas by gravitational effect. From this component, the liquid and the gas continue flowing in different lines: the liquid line starts from the bottom of the separator, while the gas line starts from the upper part.

After the separator, the liquid line splits in two. One side leads to the by-pass section where a heat exchanger (6b) dissipates the heat produced by the pump, in order to preserve the correct operative conditions in which the pump has to work. The amount of liquid mass flux at inlet of the pump can be regulated by the presence of a valve. The other side leads the liquid to the test section, after being passed through a series of components of the circuit. The heat exchanger (6a) subcools the liquid to avoid the evaporation, because the fluid is in saturated conditions after passing through the phase separator. Afterwards, in the oil separator (8), the liquid is purifying by the presence of the oil collected during the flow inside the pump, where it's used as a lubricant for the proper functioning of the machinery. The presence of the oil is undesired inside the circuit outside the pump because it affects the fluid properties and the heat transfer measurements. After being purified, the liquid flows in two parallel pipes in order to better regulate the amount of fluid to send to the test tube. In fact, each pipe is connected to a Coriolis flow meter (3), able to measure mass flow. Next to this measurement section, there are two needle valves (4) that control the mass flow allowed in the static mixer (5), where the liquid and the gas pipes are reconnected.

Similarly, after the two-phase separator, the gas line is split in three parallel pipes connected to Coriolis flow meters (3) and to needle valves (4) to set the pressure

loss, as already seen for the liquid lines. In the static mixer (5) the two lines converge and the desired fluid composition for the test section is provided.

3.1.2 Secondary Cycles

The secondary cycles consist of four smaller circuits connected to the primary cycle, as can be seen in Figure 3.1.

The purpose is to vary the thermal level of the working fluid in different positions: they are mainly composed by a heating machine, a pump, a heat exchanger and a thermostat that controls the temperature of the secondary working fluid. A brief description is furnished:

- Test Section Inlet Cycle (*SECTSI*) is placed before the entrance of the test section and it provides heat to the working fluid in order to rise the inlet temperature, especially when overheated gas is requested. In two-phase applications it can be used to control the gas quality of the working fluid. It is equipped with five valves that allow the working fluid to bypass the heat exchanger or to flow just in a smaller part of it, with the purpose to reduce the pressure drop for high mass flows.
- Test Section Cycle (*SECTS*) includes the heat exchanger connected at the end of the test tube, with the purpose of cool down the inlet temperature of the oil.
- Test Section Outlet Cycle (*SECTSO*) is connected to a heat exchanger downstream the test section. It is normally used when it is necessary to cool down the working fluid or to complete the condensation in phase transition tests. A bypass cycle is included, in case its utilization is not requested.
- Cooling C is an additional heat exchanger to provide subcooling of the liquid phase, if needed.

3.1.3 Test Section

The test section is the main component to be investigated during the experimental processes because the condensation occurs inside the tube, through the heat exchange between the working fluid and the secondary fluid flowing in counter flow.

The test section consists of a micro-fin tube 3150 mm long, with a diameter of 15.1 mm. A 2400 mm long-shell and with a diameter of 37 mm is coupled with the tube, in

order to permit the flowing of the oil for the heat exchange. A schematic representation is reported in Figure 3.4.

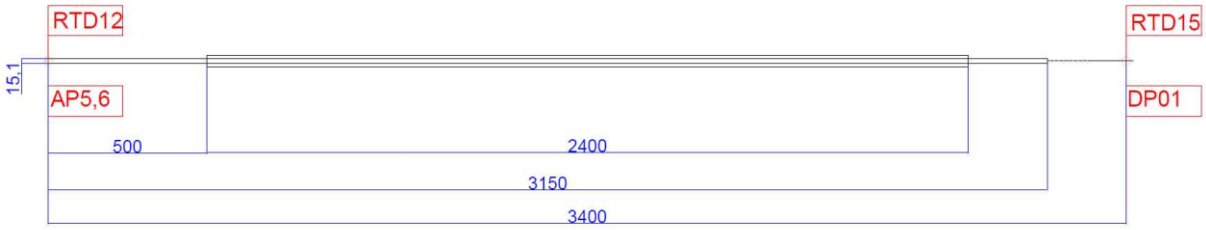

Figure 3.4: Representation of the test section

The working fluid flows inside the inner diameter, while, in the shell tube, thermal oil (therminol D12) is used as secondary fluid.

The tube is positioned between a compensator sleeve in order to avoid the mechanical stress to the structure while the whole facility is working.

All the parameters are controlled through the sensors carefully located with the purpose to collect the pressure and temperature data of both the working and secondary fluid.

As concern the working fluid, in order not to disturb the flow and to have a better hydro-thermodynamic behavior of the working fluid, inside the test section there are no sensors. This choice has been made also considering the difficulties related to this kind of installation. Before the entrance of the test section, pressure and inlet temperature are measured by an absolute pressure sensor (AP5,6) and a temperature sensor (RTD12). The outlet temperature and the pressure loss are then measured after the exit of the test section with a second temperature sensor and a differential pressure sensor (RTD15, and DP01). The configuration can be seen in Figure 3.4.

To obtain data along the test tube, type K thermocouples (TC) are glued around the outer diameter of the inner test tube wall in four measurement positions. A representation of their disposition along the tube is shown in Figure 3.5, while in Figure 3.6 a photo shows how the sensors are glued to the tube.

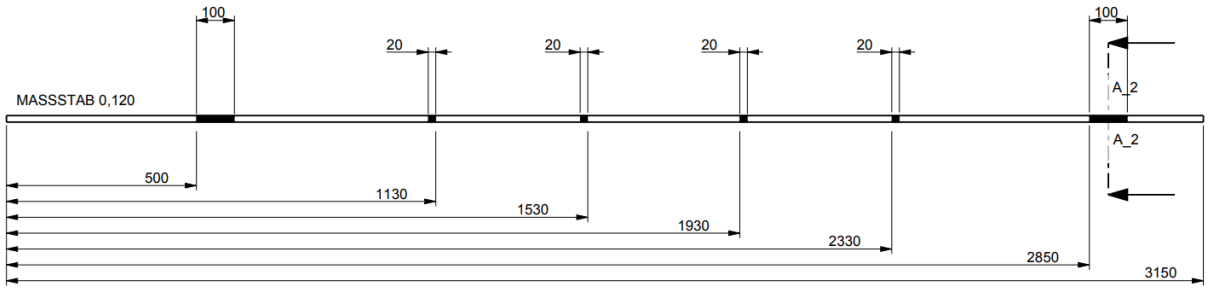

Figure 3.5: Disposition of the thermocouple along the test tube

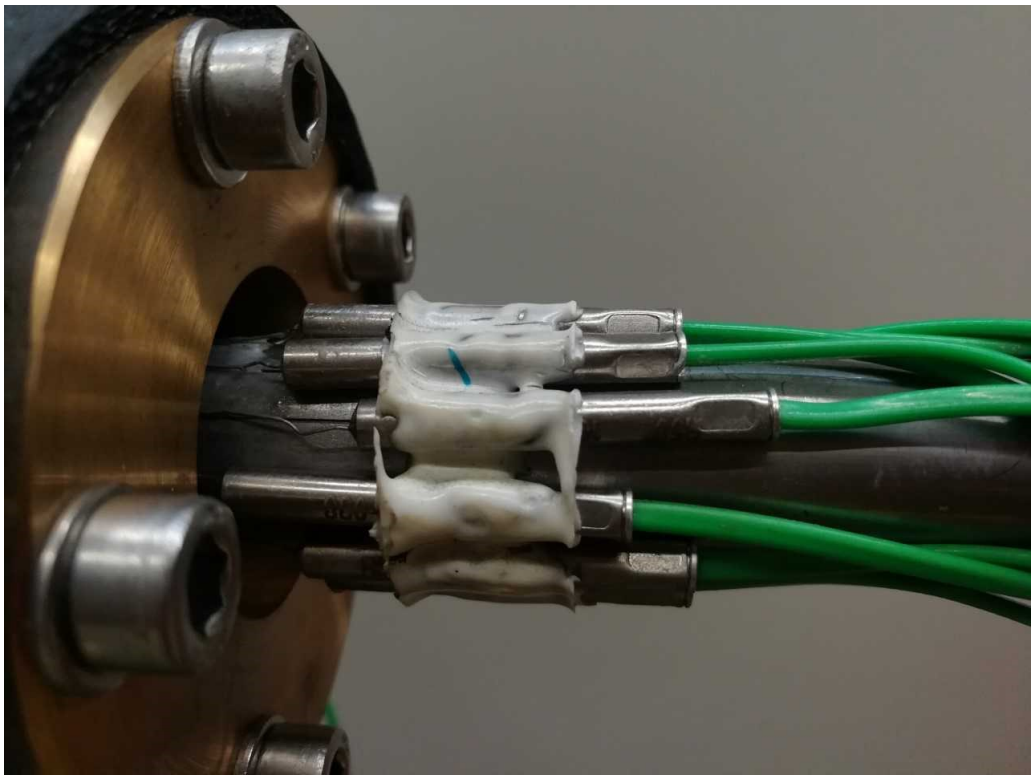

Figure 3.6: Thermocouples glued in the tube

In the first and final sections, four thermocouples are arranged at 90° from each other, while in the two middle sections eight sensors are installed at 45° from each other. A representation of the location in the middle section is given in Figure 3.7.

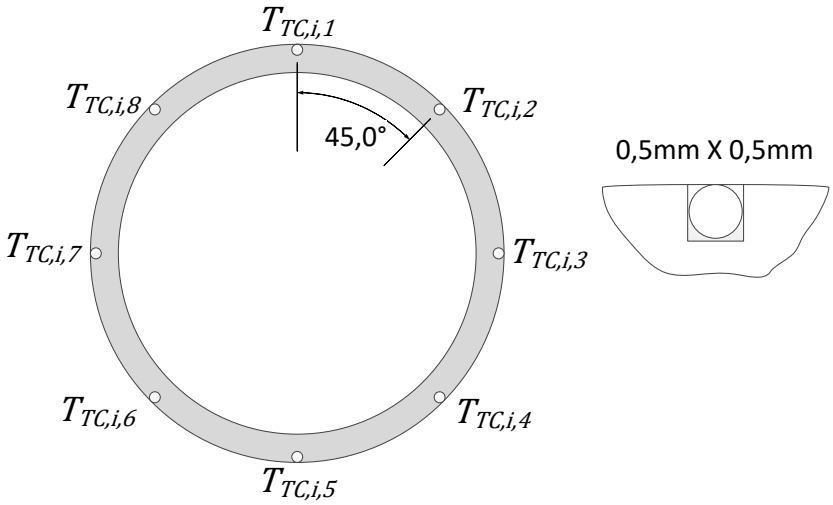

Figure 3.7: Disposition of the thermocouples around the tube in the middle sections

The total amount corresponds to 24 temperature sensors employed.

Along the tube, the tidy disposition of the thermocouple wires, avoiding the crossing of the cables, is crucial to prevent derived turbulence effects into the flow. In fact, this induced turbulence could affect the value of the heat exchanged and of the pressure losses, providing errors during the measurements. In fact, the data collected would be different in comparison with the ones collected for a flow without interferences.

For some industrial applications, just the general trend of the temperature along the tube is requested, without precise information for each section. In these cases, integral measurements are run, just involving the sensors positioned at the inlet and the outlet of the test section.

The structure of the shell tube is shown in a more detailed way in Figure 3.8.

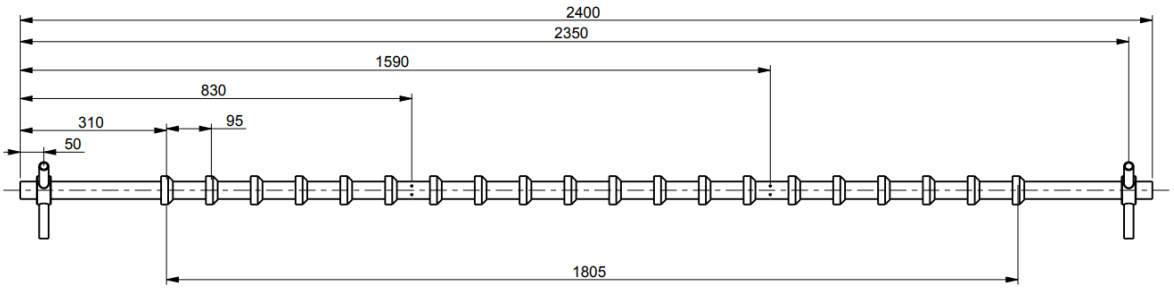

Figure 3.8: Structure of the shell tube

The pressure of the secondary fluid is measured at inlet and outlet section of the shell tube to detect the whole amount of pressure drop, while the temperature is detected in 20 positions every 95 mm through the use of resistance thermometers (RTD24(1-4) - 26(1-4)) threaded in the outer pipe and positioned in the center of the bulk flow. In every section, the position of the temperature sensors has an offset of 180° and is alternated in the upper and bottom side of the tube, as can be seen in Figure 3.9.

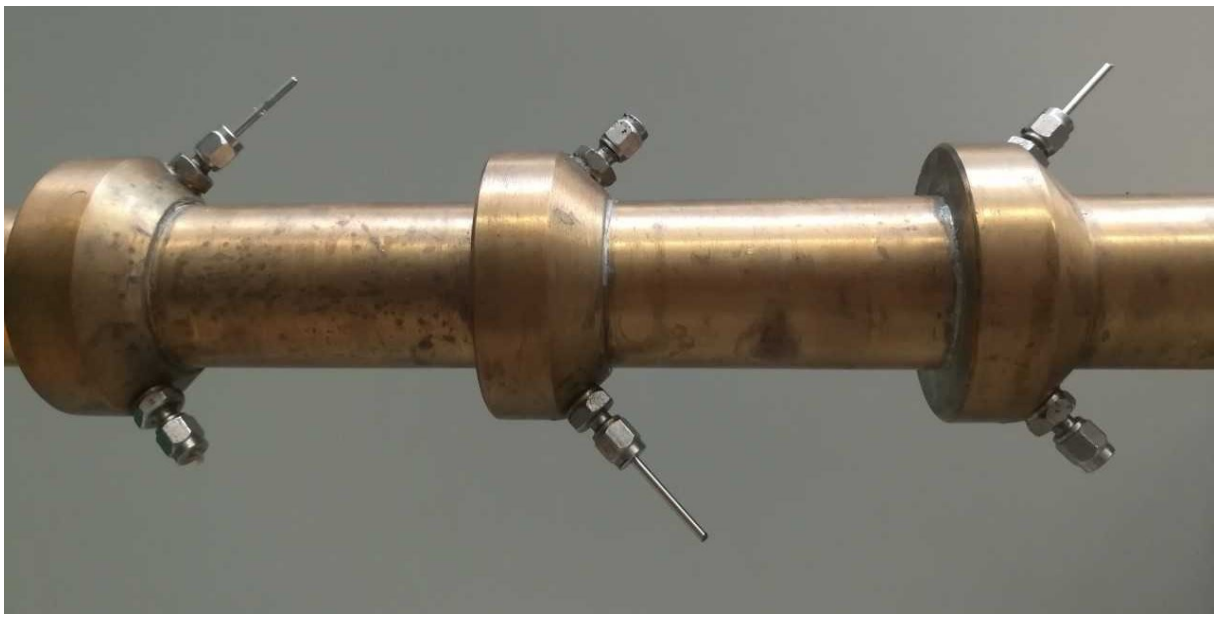

Figure 3.9: Disposition of the RTD sensors along the shell tube

This arrangement has been chosen to guarantee the higher accuracy during the measurements and to reduce the errors that the turbulent flow inside the annulus could create. Moreover, the use of a wide amount of measurement sections allows to estimate with more accuracy the temperature trend of the secondary working fluid along the test section.

Connected to the shell tube, there is the Test Section Cycle (*SECTS*), equipped with a cooling machine (Huber 635 W) which provides the set temperature to the oil and conveys it towards the test section through three sub pipes connect to the delivery with the test section, as seen in Figure 3.10.

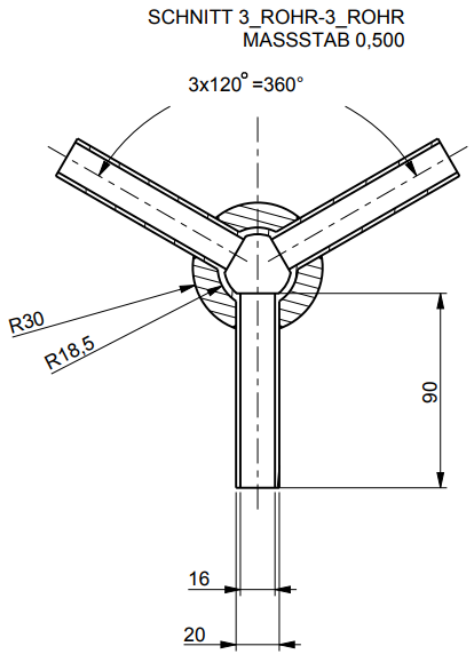

Figure 3.10: Structure of the channels for the oil entrance and exit from the test section

The Test Section Cycle (*SECTS*) is also equipped with a bypass valve which can be used to regulate the mass flow to the test rig. The secondary fluid flows through a flow meter and then in the shell side, in counter flow to the primary working fluid. Before entering the heat exchanger, inlet temperature of the secondary working fluid is measured (RTD14).
The outlet temperature of the secondary fluid (RTD13) is measured after the regroup of the outlet sub pipes. A return pipe connects the outlet of the test section with the cooling machine closing the cycle.

3.2 Sensors

Three groups of sensors are used in the test rig to measure the hydro-thermal proprieties of the fluids:

- Temperature sensors
- Pressure sensors
- Mass flow sensors

All the sensors are connected to a multiplexer where all the signals coming from the test rig converge in order to be processed by the measurement computer, involving the LabView software. Through the program, the display of all the parameters of the circuit is shown and the control of the valves is possible.

3.2.1 Temperature Sensors

As mentioned in the previous description there are two kinds of temperature sensors in the test rig called with different acronyms: TC for Thermocouple and RTD for Resistance Temperature Detector.

- The thermocouples TC are active transducers so they don't need power supply. They directly convert the heat in electricity generating a voltage difference as output, based on the Seebeck effect. The thermocouples employed are K type, composed by two-conductor alloys, Chromel and Alumel, and they are also covered with two protective layers: The outer one is made by Inconel while the inner one is made by Magnesium oxide. This kind of thermocouple is particularly resistant due to the materials used, and this characteristic makes them suitable to work in oxidant environments with a wide range of temperatures. In addition, they have a quick response to temperature variations and they usually have a quiet longer life in comparison to the other types. In this application, the hot junction is glued into the grooves all around the test tube, while the cold one, used as a reference, is placed in a metal plate. The temperature is measured with a resistance temperature detector. Since the thermocouples are glued into the grooves, an additional thermal resistance occurs and a correction has to be implemented in order to calculate a proper value of the heat transfer coefficient.

Resistance Temperature Detector RTDs are passive sensors; their functioning is based on the dependence existing between the resistivity of a conductor and the temperature. To record all of the changes and to perform the measurements, electricity has to be provided to the RTD. They work in a more limited range of temperature in comparison with Thermocouples but, as an advantage, they have a more linear behavior which allows them to be calibrated easily through a calibration bath (JuLabo FK31SL). The RTD employed in the test rig are PT100, so a platinum electrical resistance that measures 100 Ω at a temperature of 0 degree. This kind of sensors is suitable to work in a rugged environment.

3.2.2 Pressure Sensors

Absolute and Differential Pressure transducers are used for the measurement of the pressure in the rig. Pressure measurements are used to calculate the fluid proprieties in the test section and to analyze the pressure drop along the length of the tube. Furthermore they are used to ensure the proper functioning of the multiphase pump, to avoid damages. Strain gauges pressure sensors are installed in the rig. The structure is made by a diaphragm in contact with the fluid which is deformed by the pressure. The deformation is measured and the corresponding pressure value is obtained.

3.2.3 Flow Sensors

Two types of flow meters are employed in the test rig: Coriolis and Rotameter flow sensors.

- Coriolis sensors are inertial flow meter that measure directly mass flow through the variation of the angular momentum induced in the fluid by the sensor. These sensors are used to measure the gas and liquid mass flow in the divided phase segment of the rig after the phase separator. The flow meter consists of a pair of parallel vibrating tubes, which deflect according to the mass flow rate of the measured fluid that is flowing inside. The tubes are fixed in two parts. An electromechanical drive unit, positioned midway between the two anchors, provides vibrations in each tube and this motion induces the fluid particles to move orthogonally in respect to the direction of the main flow. This effect produces a Coriolis force, that causes a deflection of the tubes. The deflection is measured by a suitable sensor.
- Rotameter sensors are variable area meter and in the test rig they are used to measure the bypass flow. A shaped weight inside the sensor is pushed up by the drag force of the flow and pulled down by gravity. The position at the equilibrium defines the volumetric flow in the pipe. The output value is also given by an analogic indicator outside the sensor.

3.2.4 Sensors Data Sheets

Data sheets of the sensors involved in the measurement are reported in Table 3.2.

Sensor	***Range***		***Unit***	***Accuracy***
	Min	Max		
TC			°C	$\pm$ 0,1 °C of m.v.
RTD			°C	$\pm$ 0,05 °C of m.v.
AP1	0	30	bar	$\pm$ 0,2 % of e. v
AP2	0	100	bar	$\pm$ 0,2 % of e. v
AP5,6	5	85	bar	$\pm$ 0,106 % of e. v.
DP01	0	1000	mbar	$\pm$ 0,040 % of e. v
Promass 83A04	0	90	kg/h	$\pm$ 0,1 % m.v. off 22,5 kg/h
Promass 83F25	0	3600	kg/h	$\pm$ 0,1 % m.v. off 540 kg/h
Mass2100-6	0	563,2	kg/h	$\pm$ 0,05 % m.v. off 30 kg/h
Mass2100-15	0	2914	kg/h	$\pm$ 0,05 % m.v off 80 kg/h
Mass Flux Coolin B	0	10000	kg/h	$\pm$ 0,1 % m.v. off 105 kg/h
Rotameter	0	5,5	m³ / h	$\pm$ 1,6 % m.v. off 3,065 m^3/h

Table 3.2: Sensor data sheets

3.3 Fluids of the Test Rig

All the fluids employed in the test rig can be categorized in primary and secondary working fluids. The primary fluid is propylene, which flows in the whole primary circuit. Secondary fluids are used to set the temperatures of the working fluid inside the cycle and to cool down the test section. In order to quantify the intake or outtake of heat in the test rig, thermal proprieties of these fluids have to be established.
In the whole test rig, three different fluids are used:

- Propylene: it is a hydrocarbon and it is used as working fluid in the primary cycle. Its main characteristics are briefly presented:
  - Zero Ozone Depletion Potential (ODP=0)
  - Low Global Warming Potential (GWP=2)
  - Good thermodynamic properties

  - Low charge requested
  - Good compatibility with system components
  - High flammability. According to the ASHRAE safety groups, its designation is A3, that means low toxicity but extremely high flammability.
- Water: used directly only in the first heat exchanger of the bypass cycle and then as waste heat fluid in the cooling machine of the SECTSO and in all the Huber thermostats.
- Therminol D12: it is based on halogen-free chemistry and has an operating temperature range of -85°C to 190°C. Thanks to its excellent heat transfer properties, in the test rig it is used in all secondary cycles and in the test section to exchange heat with the working fluid. For that reason its properties have to be evaluated precisely; they can be easily detected using the REFPROP software.

3.4 Safety measures

Since the working fluid used in the facility is high flammable, safety measures against explosion has to be taken into account. The primary circuit is surrounded by an enclosure and a gas warning sensor detects the percentage of hydrocarbon in the air. If a certain limit is exceeded, a ventilator system is activated and the working fluid is drained outside the enclosure and adsorbed by an activated carbon filter.

4 DATA REDUCTION

In this chapter, the methods to collect the data and to calculate the heat transfer coefficient for a two-phase fluid are explained. The pressure losses are directly measured through the sensors, without involving any calculation or correction of the values reached.

4.1 Thermal Resistances

During the heat exchange, many thermal resistances interfere in the process, reducing the amount of heat transferred. The knowledge of these effects is needed to implement a deeper analysis of the data, if requested.

- Insulation Resistance, R_{ins}, is the resistance of the insulation layer wrapped around the outer tube. The insulation layer is put to reduce the amount of heat exchanged between the cooling fluid and the external environment.
- The external Resistance, $R_{out,}$ is the thermal resistance of the shell side of the test pipe. The resistance occurs between the temperature sensed by the thermocouples on the outer wall of the inner tube and the temperature of the cooling fluid.
- Corrective Resistances, $R_{Corr,ext}$, $R_{Corr,int}$ are related to the constitutive layers of the thermocouples. A schematic representation of layers involved is given in Figure 4.1.

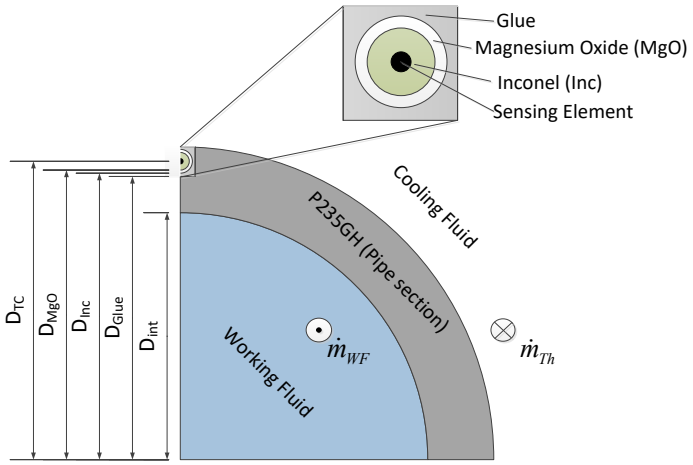

Figure 4.1: Composition of the layers in the wall of the test pipe

- The internal Resistance, $R_{int,}$ is the resistance of the convective heat transfer coefficient and its calculation is the purpose of the tests run in the facility. It occurs between the inner wall temperature and the working fluid temperature.

4.2 Heat transfer coefficient

For the constitution of the test rig, both integral and local measurements of the heat transfer coefficient can be done. In the first case, only the data at the beginning and at the end of the test tube are collected, while in the second case, the one regarding this work, the data all along the length of the tube are necessary.
As explained in chapter 3, to reach this purpose the thermocouples are installed in the external surface of the inner tube to detect the local wall temperature profile and, indirectly, the temperature trend of the primary fluid. In order to improve the accuracy, the wall temperature in each measurement section is assumed as the mean value provided by all the *n* sensors installed in that section.

$$T_{wall,i} = \sum_{j=1}^{n} \frac{T_{wall,i,j}}{n} \tag{4.1}$$

Due to several reasons, some sensors may record wrong data which can affect the results of the data reduction. To avoid this problem, the disconnection of the inaccurate sensor from the multiplexer is possible.
Considering the energy balance in the system between the two fluids, the heat flux of the working fluid in the *i-th* measuring section is:

$$\dot{Q}_{p,i} = \dot{Q}_{oil,i} + \dot{Q}_{loss,i} \tag{4.2}$$

The heat loss is defined as:

$$\dot{Q}_{loss,i} = \frac{\lambda_{ins} \cdot 2\pi \cdot z_i}{\ln\left(\frac{D_{ins,ext}}{D_{ins,int}}\right)} \cdot \Delta T_{ins,i} \tag{4.3}$$

Where the thermal potential is expressed by:

$$\Delta T_{ins,i} = T_{ins,ext,i} - T_{ins,int,i} \tag{4.4}$$

The temperatures inside and outside the insulation layer are not measured and, as a consequence, the determination of the heat loss is not possible. As an assumption,

the measuring section is considered an adiabatic system. This simplification is possible considering the presence of the insulation layer all around the tube, characterized by a low thermal conductivity ($\lambda_{ins} = 0.033\ W/(m \cdot K)$). The amount of losses is negligible.
With this hypothesis,

$$\dot{Q}_{p,i} = \dot{Q}_{oil,i} \tag{4.5}$$

In particular, the heat transfer in the oil is expressed by:

$$\dot{Q}_{oil,i} = \dot{m}_{oil} cp_{oil} (T_{oil,i+1} - T_{oil,i}) \tag{4.6}$$

The specific heat capacity of the oil is assumed to be constant between two measurement sections.
The heat transfer can be estimated also as follow:

$$\dot{Q}_{oil,i} = \left|\dot{Q}_{p,i}\right| = K \cdot A \cdot \Delta T_{ml} \tag{4.7}$$

Where the ΔT_{ml} is the logarithmic mean temperature difference between the oil and propylene temperatures:

$$\Delta T_{ml} = \frac{\left(T_{p,in} - T_{oil,out}\right) - \left(T_{p,out} - T_{oil,in}\right)}{\ln\left(\frac{T_{p,in} - T_{oil,out}}{T_{p,out} - T_{oil,in}}\right)} \tag{4.8}$$

KA is the global heat transfer coefficient multiplied for the area of the hollow cylinder:

$$\frac{1}{KA} = \frac{1}{\alpha_{inside} A_{inside}} + \frac{\delta}{\lambda_{medium} A_{medium}} + \frac{1}{\alpha_{outside} A_{outside}} \tag{4.9}$$

Just the thermal resistance of the tube wall is taken in account, while the thermal resistance of the glue layers in considered negligible.
From the Equation (4.8), the value of α_{inside} can be made explicit, but since the value of the heat transfer coefficient in the oil side $\alpha_{outside}$ is not known, and it would provide too many unknown variables in the equation, a modification of the (4.7) is implemented. The variation is proposed taking account of the information available from the data collected in the test rig. In particular, the wall temperature represents a useful variable to use. Considering the heat flux exchanged between the working fluid and the tube surface, it's possible to write:

$$\dot{Q}_{oil,i} = \left|\dot{Q}_{p,i}\right| = K \cdot A \cdot \Delta T_{mean} \tag{4.10}$$

The temperature difference is calculated between the propylene in saturated condition and the mean value of the wall temperature, defined in equation (1):

$$\Delta T_{mean} = T_{p,i} - T_{wall,mean} \tag{4.11}$$

The corresponding value of the KA is given:

$$\frac{1}{KA} = \frac{1}{\alpha_{inside} A_{inside}} + \frac{\delta}{\lambda_{medium} A_{medium}} = \frac{1}{2\pi \cdot dz}\left(\frac{1}{\alpha_{inside} r_{inside}} + \sum_j \frac{1}{\lambda_j} \ln\left(\frac{D_{j+1}}{D_j}\right)\right) \tag{4.12}$$

Since the local values are needed, the heat transfer has to be calculated in any point of the tube length z. The equation (4.10) can be written as:

$$\frac{\Delta \dot{Q}_i}{\Delta z} = K \cdot A \cdot \frac{\Delta T_{mean}}{\Delta z} \tag{4.13}$$

Replacing the equation (4.12) in (4.13):

$$\frac{\Delta \dot{Q}_i}{\Delta z} = \frac{2\pi \cdot \Delta T_{mean}}{\alpha_{inside} r_{inside} + \sum_j \frac{1}{\lambda_j} \ln\left(\frac{D_{j+1}}{D_j}\right)} \tag{4.14}$$

From the Equation (4.13) the mean value of the heat transfer coefficient can be written as:

$$\alpha_{i,mean} = \frac{1}{r_i\left(\frac{2\pi \Delta T_{mean}}{\frac{\Delta \dot{Q}_{oil,i}}{\Delta z}} - \sum_j \frac{1}{\lambda_j} \ln\left(\frac{D_{j+1}}{D_j}\right)\right)} \tag{4.15}$$

$\alpha_{i,mean}$ refers to the mean value of the heat transfer coefficient that is possible to calculate as a unique average value in a single section around the hollow cylinder. It is considered as a mean value because it takes account of the mean temperature wall of each section, as described in equation (4.1).

In order to consider all the different values of the heat transfer coefficient around the cylinder in a single section, another definition of the temperature difference is used:

$$\Delta T_{local} = T_{p,i} - T_{wall,local} \tag{4.16}$$

$\alpha_{i,local}$ is consequently defined as follow:

$$\alpha_{i,local} = \frac{1}{r_i\left(\frac{2\pi\Delta T_{local}}{\frac{\Delta\dot{Q}_{oil,i}}{\Delta z}} - \sum_j \frac{1}{\lambda_j}\ln\left(\frac{D_{j+1}}{D_j}\right)\right)} \tag{4.17}$$

If the values of the heat transfer coefficients are requested not only in the four measurement sections but in every point along the length, it is sufficient to interpolate the wall temperature in the segment between two following measurement sections.

4.3 Working fluid properties

Inside the inner diameter of the test tube, no sensors are installed to avoid interference inside the flow. As a consequence of this choice, the temperature of the working fluid is unknown, but it can be evaluated making a linear interpolation along the length between the inlet and outlet values, that are precisely collected by the sensors, as seen in Chapter 3.

Linear tendency is a simplifying assumption, because the fluid is two-phase and the change of temperature could have a more complicated trend.

The heat exchanged from the two-phase flow side can be expressed as follow:

$$\dot{Q}_{p,i} = \dot{m}_p \Delta h_{evap}(x_{i,p} - x_{i+1,p}) \tag{4.18}$$

Δh_evap represents the enthalpy of evaporation of propylene at the working pressure, while x_i is the flow vapor content in the measurement section. This variable can't be directly measured due to the experimental setup of the test section, but it can be indirectly determined as:

$$x_{i+1,p} = -\frac{\dot{Q}_{i+1}}{cp_p \dot{m}_p} + x_{i,p} \tag{4.19}$$

The inlet vapor quality is calculated considering the energy balance in the static mixer, before to enter in the test tube.

$$x_p = \frac{h_{inlet} - h_{L,sat}}{h_{G,sat} - h_{L,sat}} \tag{4.20}$$

The values of enthalpy of the saturated liquid $h_{L,sat}$ and of the saturated vapor $h_{G,sat}$ are specific for each substance and depend on the pressure. In the test rig, the

pressure in the static mixer is measured, so the enthalpies of the saturated fluid can be determined properly using the REFPROP software.
The enthalpy at inlet refers to the enthalpy of the mixture, and takes account of the mass flow measured in the gas and liquid lines before to enter in the static mixer.

$$h_{inlet} = \frac{\dot{m}_G h_G + \dot{m}_L h_L}{\dot{m}_G + \dot{m}_L} \tag{4.21}$$

The specific enthalpies h_G and h_L are function of both temperature and density. The density is measured by the Coriolis sensors in the gas and liquid lines, while the temperature is measured by the RTD that are installed all along the test rig.
The real mass flow of the liquid and the gaseous phase at inlet of the test section can be compared with:

$$\dot{m}_G = x \cdot \dot{m}_{tot} \tag{4.22}$$

$$\dot{m}_L = (1 - x) \cdot \dot{m}_{tot} \tag{4.23}$$

The volumetric flow vapor content is calculated by doing the ratio between the gas and the total volume flow:

$$\xi = \frac{V_G}{V_{tot}} = \frac{\frac{\dot{m}_G}{\rho_G}}{\frac{\dot{m}_G}{\rho_G} + \frac{\dot{m}_L}{\rho_L}} \tag{4.24}$$

5 EXPERIMENTAL RESULTS

In this chapter the procedure of the data acquisition for the experimental investigation is described. Afterwards, the results of the measurements are shown in chronological sequence in order to explain how the commissioning phase of the rig was carried out.

5.1 Measuring with the KIIR Test Facility

Before to start with the measurements, it's necessary to arrange the test rig. The test tube to be investigated is installed and insulated all around the external diameter to reduce the influence of the external temperature and the heat dispersion. Then the RTD and TC sensors are connected.

5.2 Validation tests

In order to obtain precise results from the experiment, it is appropriate to check if all the sensors are working in a correct way. In fact, since they are sensitive and fragile instruments, it is quiet common that some of them are broken or damaged.

5.2.1 Temperature sensors

For the first measurement, the circuit is stopped and left static, so the temperature of the environment is collected by the RTDs and TCs for three days. The data are displayed and controlled through the LabView software, then the trend of the temperature over the time is plotted in two graphs to better analyze the results. From this step, it's evident how the RTDs are working in a proper way, recording coherent values (Figure 5.1). Since it is known that some RTDs are not working, their corresponding values are not take into account.

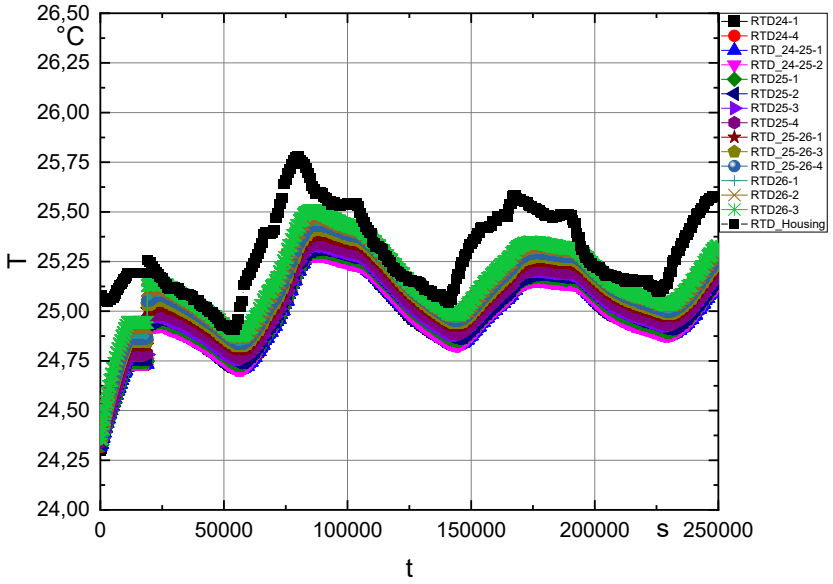

Figure 5.1: Environmental temperature collected by RTDs over the time

On the contrary, it is evident that some TCs are not precise, as it can be seen in Figure 5.2.

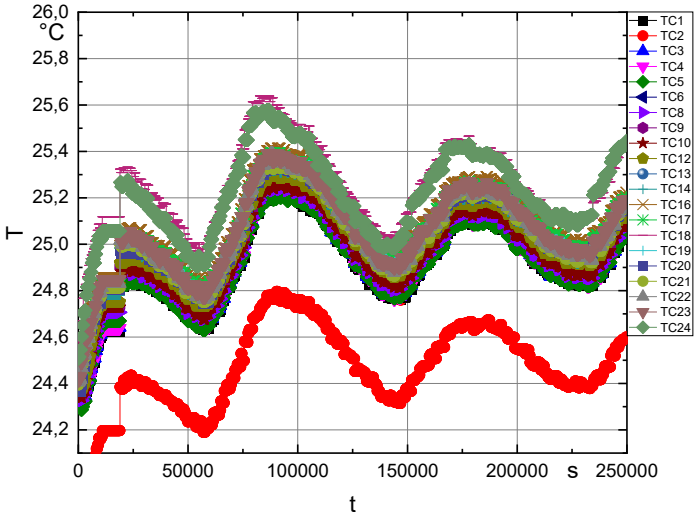

Figure 5.2: Environmental temperature collected by TCs over the time

To better understand this trend, the temperature over the position along the length of the tube is plotted in Figure 5.3, highlighting the four measurement sections. The measurements are done four times.

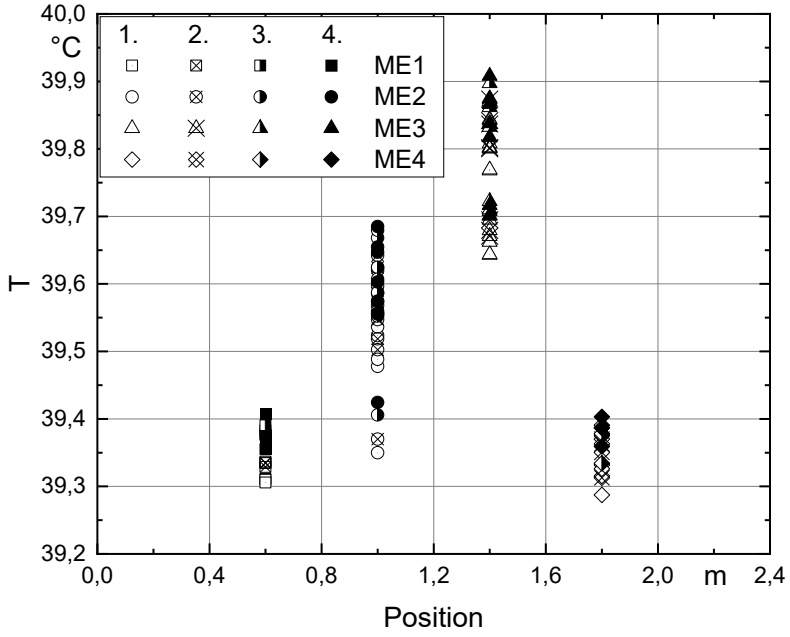

Figure 5.3: Plot of temperature over the position along the tube length

It's evident that in the first and fourth sections all the thermocouples involved measure the same value of temperature with high accuracy, while in the second and third sections there is a wider range in the spread of the values. Since the sensors are very sensitive and it's common that some breakages occur, a comparison with new sensors is done. The new thermocouples are put in a container with a distilled water at 0°C and the data are collected. The plot shows the same trend of the other thermocouples, making possible to exclude damages in the sensors. Checking the data obtained during the calibration process, the same trend is confirmed. To exclude mistakes due to a not-suitable calibration functions, a correction of the functions is implemented. Since the thermocouples are glued to the inner tube and their removal is not possible, a different procedure is used. The cooling machine (Huber 635 W) of the SECTS cycle is set to provide specific temperatures to the oil (from 0°C to 80°C), that are collected by the thermocouples. Since the values of the voltage are not available, a graph between the reference temperature and the thermocouple

temperature is made for all the TCs. A linear interpolation is implemented by the program and the coefficients of interpolation are calculated. In such a way, the new calibration functions are defined and set inside the LabView software to give the correct output values of temperature during the measurements. Figure 5.4 shows the graph for the TC1.

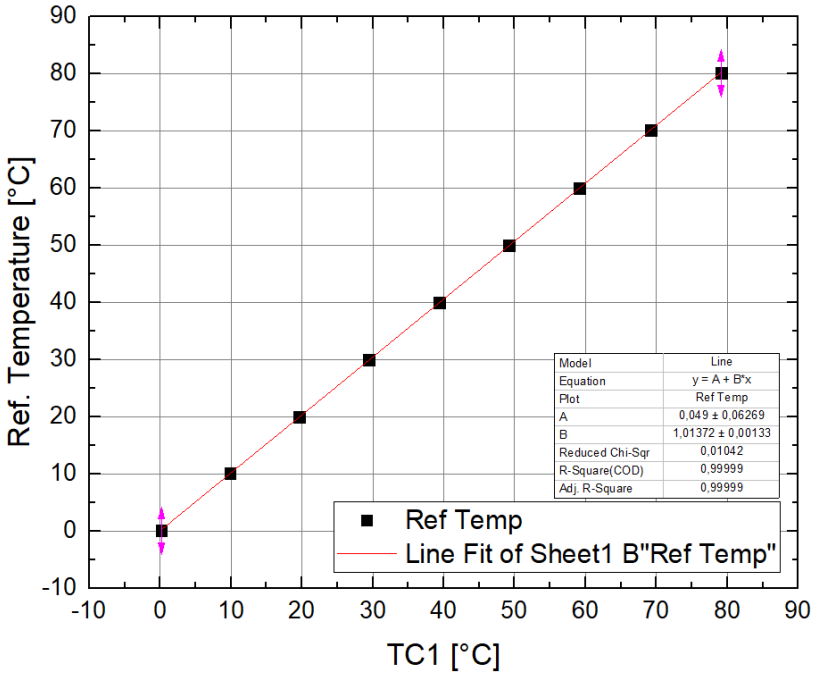

Figure 5.4: Calibration function for TC1

As it is possible to see in Figure 5.5, the new calibration functions record more precise values, since the range of temperature difference between the different sensors is reduced. The majority of the TCs collect data inside a range between 40,3°C and 40,4°C.

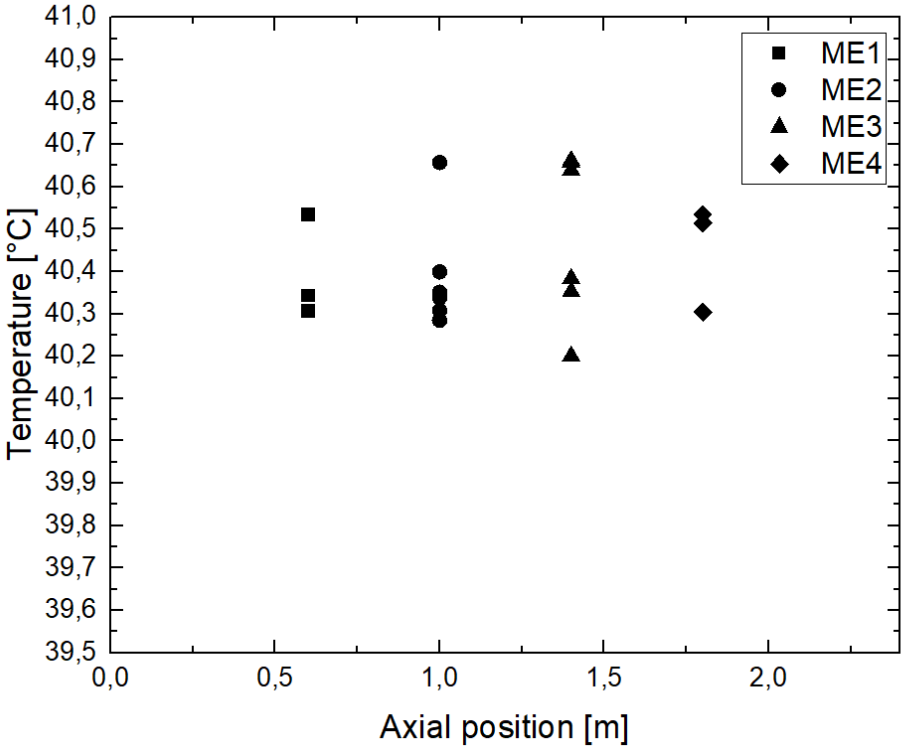

Figure 5.5: Temperature data collected using the new calibration functions

To improve the accuracy, the offset of the sensors that work outside from this range is correct. This procedure is applied for TC1, TC9, TC14, TC16, TC17, TC19, TC21, TC22. It is conceivable that some thermocouples record temperature values outside the acceptable range because they are more affected by external interference. For example, it has been suggested that the insulation of some sensors is not completely accurate, or that there are interferences between certain components in the circuit, or that the sensors are influenced by the direction of positioning.

Similarly, some RTDs (RTD24-25-2, RTD25-3, RTD-4, RTD25-26-1) show values outside the range desired, as seen in Figure 5.6. Their offset is correct in order to reach values inside the same range of the others.

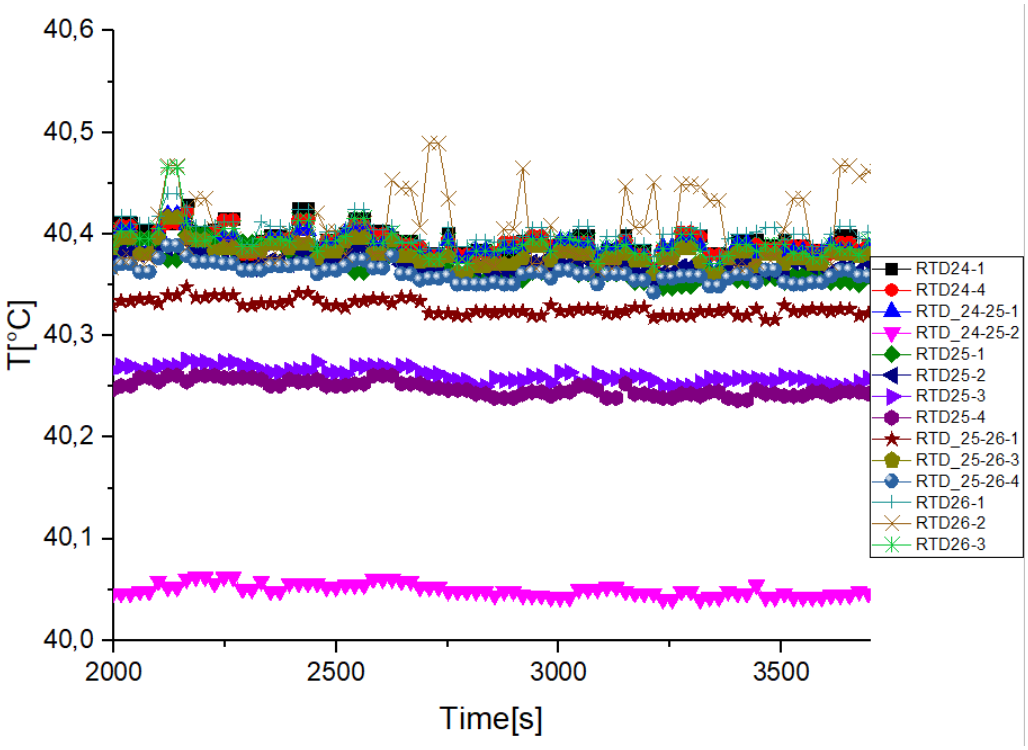

Figure 5.6: Temperature measured by the RTDs over the time

5.3 Experimental heat transfer coefficient and pressure losses

The KIIR test facility is built to investigate the condensation process of hydrocarbons, as explained in detail in Section 3.1. During experimental operations, inside the test section flows a two-phase mixture with decreasing vapor quality along the heat exchanger.

All the parameters can be checked simultaneously because the circuit is displayed through the LABVIEW software. Some variables can also be changed directly from the software, acting for example on the opening section of the valves to change the mass flux or the vapor content, or changing the rotational speed of the pump. The valves employed act both in the liquid and vapor pipes to change the percentage of vapor content and they have different sizes to control in a more efficient way the amount of fluid that passes through them. The value of most important parameters of the fluid before to enter in the test section, like the mass flux G and the vapor content x, are displayed in the window in the left side of the screen, to check the starting conditions.

Four different measurements are taken setting the values of temperature, pressure and mass flux of the working fluid, and the temperature difference between the oil and the propylene at the respective inlet sections, as shown in Table 5.1.

Measurements	**p***	**p**	**T_{sat}**	**G**	**ΔT_{sub}**
		[bar]	**[°C]**	**[kg/(m²s)]**	**[K]**
1	0,25	11,4	24,5	600	15
2	0,25	11,4	24,5	300	15
3	0,50	22,75	54,5	600	15
4	0,50	22,75	54,5	300	15

Table 5.1: Measurement settings

For each measurement test, the vapor content at inlet is changed between $x = 0{,}1$ and $x = 0{,}9$ with steps of $0{,}1$ unities, while the values of temperature and pressure are constant. During the test, not a complete but just a partial condensation occurs; the value of the vapor content at the exit of the test tube can be calculated thanks to the data collected, if needed.

As an example for the general trend for each experiment, Table 5.2 shows some data collected for the first measurement, such as the vapor content at inlet for each test, the propylene and oil temperature at inlet and outlet of the tube.

G [kg/(m^{2}s)]	p [bar]	x_{inlet}	Position [m]	T_{fluid} [°C]	Position [m]	T_{oil} [°C]
600	11,4	0,11885	-0,5	24,163	0	12,181
			3,4	23,568	2,4	10,528
		0,20858	-0,5	24,18	0	12,216
			3,4	23,489	2,4	10,534
		0,31137	-0,5	24,227	0	12,257
			3,4	23,342	2,4	10,531
		0,39194	-0,5	24,225	0	12,272
			3,4	23,144	2,4	10,533
		0,48712	-0,5	24,117	0	12,266
			3,4	22,819	2,4	10,532
		0,58876	-0,5	24,138	0	12,267
			3,4	22,485	2,4	10,53
		0,69563	-0,5	24,293	0	12,279
			3,4	22,054	2,4	10,529
		0,79443	-0,5	24,208	0	12,258
			3,4	21,508	2,4	10,526
		0,90476	-0,5	24,193	0	12,257
			3,4	21,165	2,4	10,531

Table 5.2: Data for first measurements

As a first analysis, it's evident that the vapor content is set inside an acceptable range of mistake around 3%. The fluid temperature is measured before and after the test section, and it is separately compared with the theoretical value of the saturation temperature at a considered pressure through the use of REFPROP software. The condensation process is theoretically considered isothermal and isobaric, but since some irreversible phenomena occur, a decrease of temperature and pressure of the fluid is recorded in the practical experience. From the Table 5.2 it is evident that the temperature difference of the propylene between inlet and outlet section increases with the increase of vapor quality. Cavallini et al. [24] provides an explanation considering that at high value of vapor content there is higher energy consumption on the vapor-liquid interference. Moreover, higher shear stress leads to higher velocity gradient and, as a consequence, also the temperature gradient in the thermal boundary layer increases. This phenomenon stands for the increase of temperature gradient near the wall that allows the increase of the heat transfer coefficient at the expense of frictional pressure drop along the tube, as it will be shown and discussed

in the following sections through the use of the plots. For an increasing vapor quality higher values for the heat transfer can be expected due to the increasing turbulences in the interphase between liquid and vapor as well as on the tube wall. At the beginning the passage from the pure vapor to the annular flow takes place pretty quickly with the formation of some liquid droplets in the cavities on the wall surfaces, and they easily grow until they create a liquid film all around the circumference. The whole process is facilitated by the enhanced structures that provide nucleation sites. Further information regarding the temperature variation of the working fluid is presented in the Appendix 8.1. In particular, the perspective of the analysis is focused on the trend of the temperature difference between the propylene end wall temperature around the circumferential section of the tube. The temperature difference is plotted for each measurement section along the length of the test tube.
The oil used as a cooling fluid has a temperature set at 10°C, but since the regulation inside the SECTS has a range of sensitivity, its temperature at the inlet of the shell tube is around 10,5°C at the position of $z = 0\ m$. It is evident how, for all the tests, the increase of temperature at the exit of the section at $z = 2{,}4\ m$ is around $2°C$.
In the following sections, the influence of the test conditions is discussed.

5.3.1 Influence of mass flux and inlet pressure for the determination of the heat transfer coefficient

In this section, the change of the value of the heat transfer coefficient over the vapor quality is discussed. Every measurement is referred to a determined value of the vapor quality at inlet of the test tube. In the following graphs, for each test four data are plotted, that refers to the vapor content and the heat transfer coefficient in the four measurement sections along the tube, with the purpose to verify how much the condensation occurs and which is the heat transferred section by section.
In Figure 5.7 is plotted the trend of the heat transfer coefficient varying the vapor content at the inlet of the test tube at $p = 11{,}4\ bar$, for two values of mass flux: $G = 600\ kg/m^2s$ and $G = 300\ kg/m^2s$. For each value of vapor quality, four data are plotted, one for each measurement section along the tube.

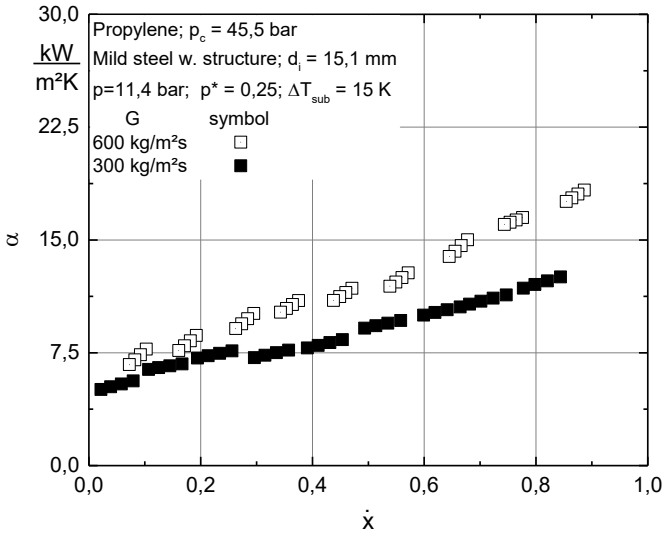

Figure 5.7: Comparison of heat transfer coefficient over the vapor content for $G = 600\ kg/m^2s$ and $G = 300\ kg/m^2s$ at $p = 11{,}4\ bar$

The general trend shows the increase of the value of the heat transfer coefficient with the increase of the vapor quality for both the mass fluxes. This behavior is explicable considering the flow pattern during condensation. In fact, the increase of the heat flux with increasing vapor quality is noticeable. In this condition, the velocity of the fluid is higher in respect of the velocity at lower vapor quality due to the lower value of the density, and this promotes turbulence, so that the interference between liquid and vapor phase is relevant. Decreasing the vapor content, some liquid drops start to appear scattered in the fluid until the annular flow is established, with a film of liquid all around the inner diameter of the tube.

Considering that an enhanced tube is used during these experiments, the passage between the pure vapor and the annular flow takes place probably quite quickly in respect of what normally happens inside a smooth tube, because the cavities facilitate the formation of the liquid drops on the surface, and they allow their growth in a more efficient way.

With a low value of vapor quality, the flow is stratified with a thick layer of liquid that provides thermal resistance and, as a consequence, the heat transfer process is less efficient. In addition, in this configuration the tube is flooded, so the advantage of the enhanced structure is less effective.

Furthermore, it is evident that the trend linking coefficient increase with vapor content growth is steeper when the mass flux is greater. The difference isn't particularly relevant at low values of vapor quality such as $x = 0{,}1$ and $x = 0{,}2$ but it becomes progressively more significant at higher values. As already explained, at low vapor content the tube is flooded by the liquid phase, so the heat transfer process is not particularly active. For high vapor content, the velocity of the fluid is higher such as the turbulence, especially increasing the mass flux, so the process is affected in a positive way as it can be seen by the maximum values reached by the heat transfer coefficient.

It is also evident that the percentage of condensation is different for the two mass fluxes despite the fact that in both cases each test is conducted with the same vapor content at the inlet of the test tube. At lower mass flux, $G = 300\ kg/m^2s$, the condensation between the four measurement sections is about 6%, while at $G = 600\ kg/m^2s$ is about $3 - 4\%$. In fact, considering $x = 0{,}1$, for $G = 600\ kg/m^2s$ the change from the first to the last section is $x = 0{,}10277 \div 0{,}07237$, while for $G = 300\ kg/m^2s$ the change is $x = 0{,}07931 \div 0{,}02157$. In the second case, the value of vapor quality in the first section it is similar to the value obtained in the fourth section at $G = 600\ kg/m^2s$. This behavior is independent of the initial value of vapor quality and it can be explained by considering the structure of the facility ring. In fact, the desired composition of the fluid occurs through the mixture of liquid and vapor coming from two different lines in the proximity of the static mixer. The vapor content is measured here, but the fluid runs through a section of pipe before entering the test section. In that line there are no further measuring systems and therefore some mechanisms are unknown. It is possible that condensation starts before entering the test section due to the fact that the subcooled liquid comes into contact with the vapor. This seems to occur especially at $G = 300\ kg/m^2s$, where the overall amount of substance in a certain area is lower, so the process probably occurs more quickly. To confirm this hypothesis, an optical visualization of the fluid inside the tube would be useful. As a final consideration, it can be said that at lower value of mass flux the condensation occurs more quickly, but since the velocity is lower, the overall heat transfer process is less efficient, so that also the heat transfer coefficient is lower.

In Figure 5.8 the trend of the heat transfer coefficient varying the vapor content at the inlet of the test tube is plotted at $p = 22{,}75\ bar$, for two values of mass fluxes: $G =$

$600\ kg/m^2s$ and $G = 300\ kg/m^2s$. For each value of vapor quality, four data are plotted, one for each measurement section along the tube.

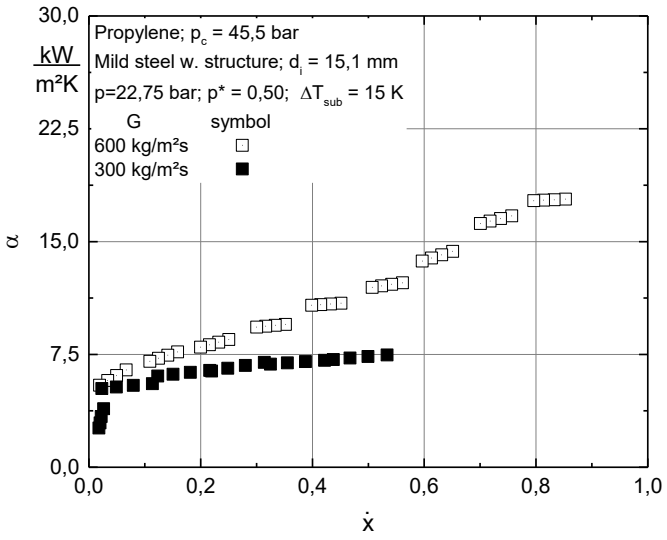

Figure 5.8: Comparison of heat transfer coefficient over the vapor content for $G = 600\ kg/m^2s$ and $G = 300\ kg/m^2s$ at $p = 22{,}75\ bar$

In this case, the data at $G = 300\ kg/m^2s$ are measured for $x = 0{,}1 \div 0{,}6$ because over these values the system wasn't reaching the stability under these conditions. The inclination of the straight line for the lower value of mass flux is flatter than for $G = 600\ kg/m^2s$. It is evident that for $p^* = 0{,}50$ the influence of the mass flux in the system is particularly relevant to achieve higher values of heat transfer coefficient, compare to the case of Figure 5.7. Moreover, for $G = 300\ kg/m^2s$ it can be seen a big increase in the alpha value, moving from $x = 0{,}1$ to $x = 0{,}2$. Then the increase is much smoother between $x = 0{,}2$ and $x = 0{,}3$. Over this point, the values of the coefficient show a trend that is almost constant at central values of vapor quality. If it had been possible to measure the data even at higher vapor values, the gradient of the curve would probably have increased again.

In Figure 5.9 and Figure 5.10 the influence of the system pressure is shown. In Figure 5.9 the data for the two different values of pressure $p = 11{,}4\ bar$ and $p = 22{,}75\ bar$ at $G = 600\ kg/m^2s$ are compared.

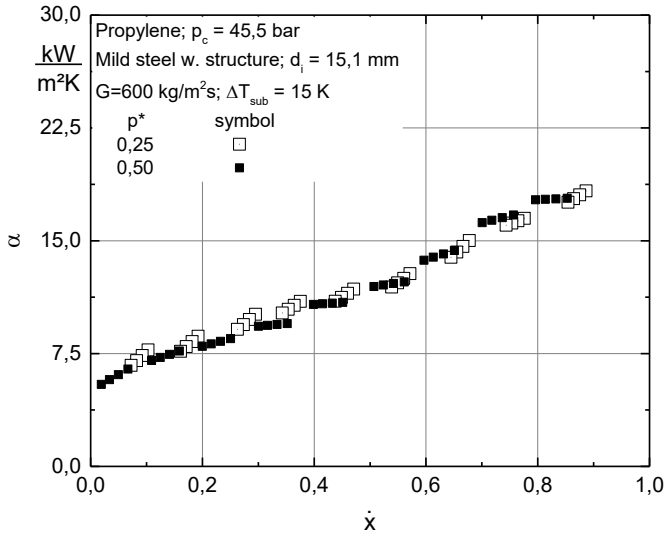

Figure 5.9: Comparison of heat transfer coefficient over the vapor content at $G = 600\ kg/m^2s$ for $p^* = 0{,}25$ and $p^* = 0{,}50$

Despite the pressure condition is different, the heat transfer coefficient's values achieved are close for all the vapor qualities. Empirical experience shows that the heat transfer coefficient at low pressures is greater than that at higher pressures. In this case, the difference is not so marked.

The main difference between the two trends can be seen by looking at the four values for each test at a specific value of vapor content at the tube inlet. As a first analysis it can be seen that, for each group of four measurements, the values related to $p^* = 0{,}25$ and $p^* = 0{,}50$ are not overlapping. The condensation percentage is different in the two cases; taking in account an average value, at lower pressure the condensation along the tube length is about 3%, while at higher pressure is about 6%. In particular, it can be observed that there is a larger variation in the vapor quality between the value measured at the inlet of the test tube and that calculated in the first measuring section, especially for $p^* = 0{,}50$. This effect can be explained considering that the properties of the fluid such as density and enthalpy are affected by the value of pressure, so at $p^* = 0{,}50$ the condensation seems to occur more quickly. Increasing the pressure, the enthalpy of both liquid and vapor phase increases, such as the vapor density. Even if the liquid density decreases, the mixture density normally increases too.

In Figure 5.10 the data for the two different values of pressure $p^* = 0{,}25$ and $p^* = 0{,}50$ at $G = 300\ kg/m^2s$ are compared.

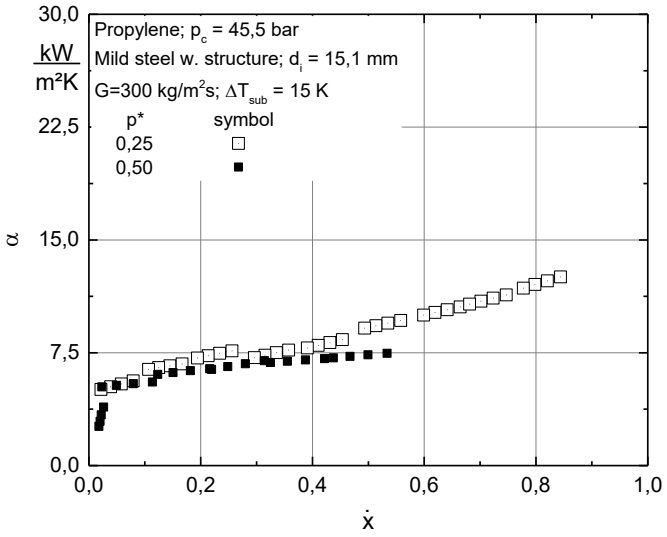

Figure 5.10: Comparison of heat transfer coefficient over the vapor content at $G = 300\ kg/m^2s$ for $p^* = 0{,}25$ and $p^* = 0{,}50$

The trend for $G = 300\ kg/m^2s$ for both the reduced pressure $p^* = 0{,}50$ is very close and the lines are almost overlapped for $x = 0{,}2 \div 0{,}5$. At $x = 0{,}6$ the inclination of the curve for $p^* = 0{,}25$ seems to start being steeper than what appears to be the trend for $p^* = 0{,}50$.

From the overall analysis of all the plots, it is evident that the variation of the mass flux influences the heat transfer process much more than the change of pressure.

5.3.2 Influence of mass flux and inlet pressure for the determination of the pressure losses

The pressure is measured before and after the test section and thus the value of pressure losses is obtained, as explained in Chapter 3. In the following graphs, the pressure variation is considered in one meter length.

In figure 5.11 is plotted the trend of the pressure losses varying the vapor content at the inlet of the test tube at $p = 11{,}4\ bar$, for two values of mass flux: $G = 600\ kg/m^2s$ and $G = 300\ kg/m^2s$.

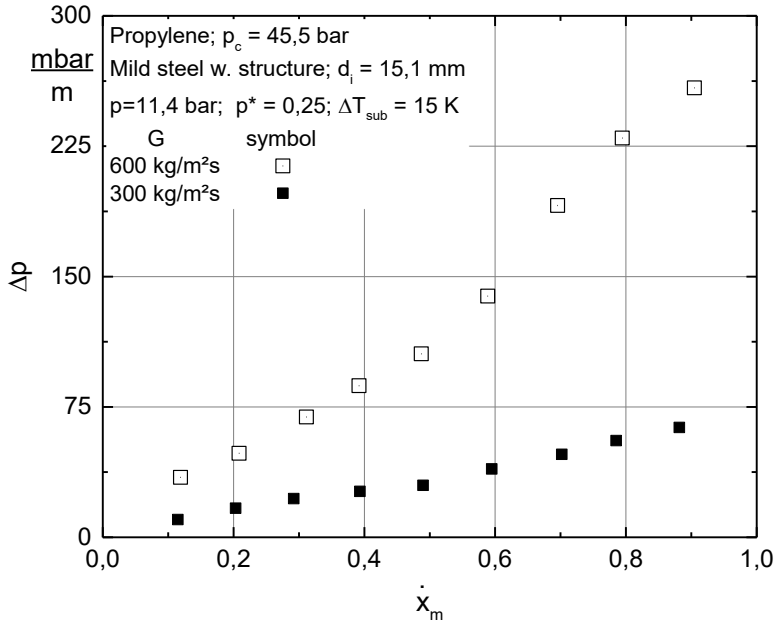

Figure 5.11: Comparison of pressure losses over the vapor content for $G = 600\ kg/m^2s$ and $G = 300\ kg/m^2s$ at $p = 11{,}4\ bar$

As a general trend, it's evident that the pressure drop increases with the vapor quality. The explanation comes from the analysis of the flow pattern: at high values of vapor content the fluid is heavily affected by the enhanced structure that promotes turbulence and friction increases the pressure losses. In addition, the motion is dominated by the tangential force between vapor and liquid film. The shear stress between the two phases causes a separation of liquid drops from the liquid phase and their mix inside the vapor. Moreover, the density of the two-phase fluid ρ_m decreases and so the overall velocity of the flow is bigger. At low amount of vapor, the tube is flooded so the presence of the micro-fins is not that relevant and the properties of the fluid are different. In fact, increasing the quantity of liquid the density increases and the velocity decreases such as the pressure loss.

Comparing the data with $G = 600\ kg/m^2s$ and $G = 300\ kg/m^2s$ it is possible to see that for both cases the trend is respected but, similarly to what happened with the heat transfer coefficient, in the second case the values obtained are much lower. In fact, at lower velocities the turbulence and the shear stress are less effective and as

a consequence the pressure losses are less important, especially for low values of vapor quality.

The slope of the curves obtained from the different mass flux values shows a different trend in the two cases. In fact, for $G = 300\ kg/m^2s$ the trend is almost completely linear, while for $G = 600\ kg/m^2s$ the trend is linear until $x = 0{,}5$, then the slope becomes steeper. It can be explained referring to the flow pattern since for high vapor quality and, at the same time, high mass flux the fluid is extremely turbulent and chaotic.

In figure 5.12 is plotted the trend of the pressure losses varying the vapor content at the inlet of the test tube at $p = 22{,}75\ bar$, for two values of mass flux: $G = 600\ kg/m^2s$ and $G = 300\ kg/m^2s$.

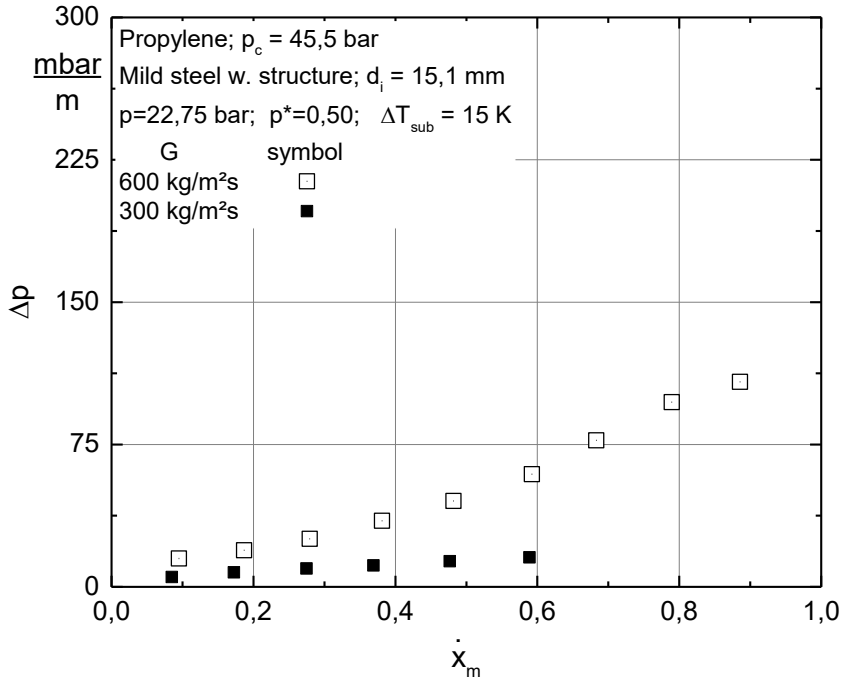

Figure 5.12: Comparison of pressure losses over the vapor content for $G = 600\ kg/m^2s$ and $G = 300\ kg/m^2s$ at $p = 22{,}75\ bar$

As seen in the previous section, the data at $G = 300\ kg/m^2s$ are measured for $x = 0{,}1 \div 0{,}6$ because over these values the system wasn't reaching the stability.

The same trend already analyzed and explained in Figure 5.8 is confirmed, but in comparison with it, the minimum and maximum values of the pressure losses are

significantly different at high pressure. In fact, considering the Figure 5.11, where the pressure is set at $p = 11{,}4\ bar$, for $G = 600\ kg/m^2s$ the value of the pressure losses varies between $\Delta p = 34{,}5 \div 258{,}5\ mbar/m$. For $G = 300\ kg/m^2s$, $\Delta p = 10 \div 63\ mbar/m$.

Considering Figure 5.12, where the pressure is set at $p = 22{,}75$, for $G = 600\ kg/m^2s$ the value of the coefficient varies between $\Delta p = 14{,}9 \div 108\ mbar/m$. For $G = 300\ kg/m^2s$, $\Delta p = 5 \div 15{,}5\ mbar/m$.

A more specific comparison is shown through the Figure 5.13 and Figure 5.14, where the pressure losses are plotted for a specific mass flux at two different values of pressure in the system.

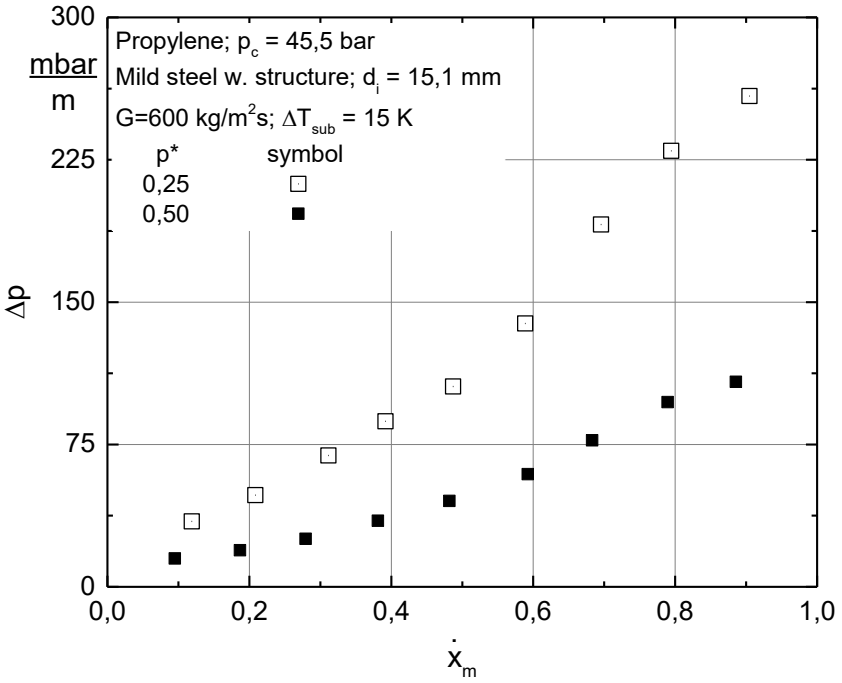

Figure 5.13: Comparison of pressure losses over the vapor content at $G = 600\ kg/m^2s$ for $p^* = 0{,}25$ and $p^* = 0{,}50$

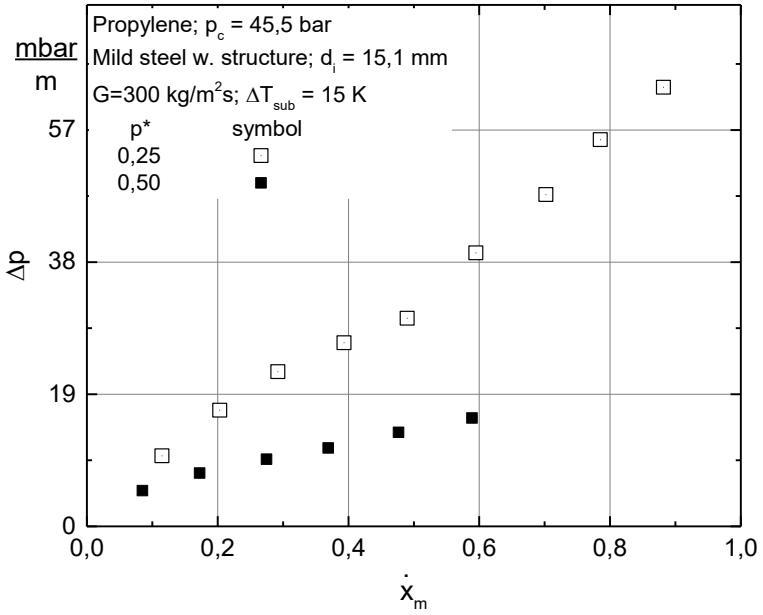

Figure 5.14: Comparison of pressure losses over the vapor content at $G = 300\ kg/m^2s$ for $p^* = 0{,}25$ and $p^* = 0{,}50$

As already explained, for both the plots the difference between the two pressures in the system is not particularly relevant for the lowest values of vapor content, while it grows hugely at high value of vapor quality.

5.4 Comparison between data collected and correlations

In this section the data collected and the results obtained by the use of some correlations are compared, both for the heat transfer coefficient and pressure losses. The correlations are implemented with the use of the software MATLAB. The properties of the fluid at different thermodynamic states are found through the use of REFPROP, linked to MATLAB.

In order to properly analyze the results, the main geometric characteristics of the test tube are defined in Table 5.3.

$$d = 15{,}1\ mm$$

$$\gamma = 30°$$

$$\beta = 50°$$

$$n_g = 30$$

$$h = 0{,}0004\ m$$

$$L = 2{,}4\ m$$

Table 5.3: Geometric characteristics of the test tube

The schematic representation of the apex angle γ, the spiral angle β and the fin height h is shown in Figure 5.15 [9].

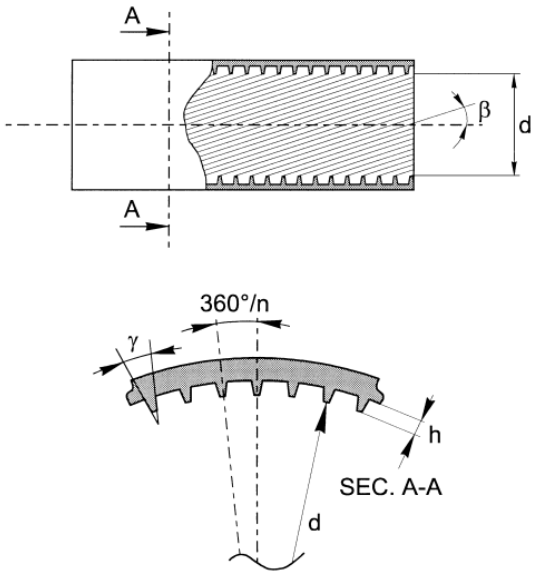

Figure 5.15: schematic representation of the apex angle γ, the spiral angle β and the fin height h [9]

5.4.1 Heat transfer coefficient

In this section, the comparison between the experimental data collected and the calculated results by the use of mathematical correlations is made. In particular, the correlations of Yu and Koyama [18] and Cavallini et al. [17] already presented in Chapter 2.3 are used, but also the correlation of Olivier et al. [19] is applied. The correlations are normally experimentally based, and the purpose of their use is to validate the empirical data through the prediction of the general trend of the heat transfer. It has to be considered that in every real experience there are some complex phenomena that can modify the trend. Prediction is particularly difficult in the case of micro-fin tubes, because the flow is made more chaotic by the enhanced

structures and the transition between one flow regime and another occurs at slightly times than with smooth tubes. Moreover, the correlations normally try to combine accuracy and simplicity as a good compromise because the mathematical description of the physical mechanisms can be particularly difficult. Normally, the correlations provide equations that can describe the overall phenomenon, but it has to be taken in consideration that the whole process is different in dependence of the flow regime inside the tube, because the internal mechanism changes while the condensation proceeds. The variation of the flow patterns reflects the different ways the vapor and liquid phases are distributed inside the tube and this is the cause why the heat transfer mechanism is different for each flow pattern [25].

The results from the correlations account values for $x = 0{,}01 \div 0{,}99$ with steps of $0{,}01$ unities, while the experimental data present four values for each group of measurements for $x = 0{,}1 \div 0{,}9$ with steps of $0{,}1$ unities, that refer to the measurement sections along the tube length.

In Figure 5.16 the values for the heat transfer coefficient at $p = 11{,}4\ bar$ for $G = 600\ kg/m^2 s$ over the vapor quality are plotted, highlighting the comparison between the experimental data and the results of the correlations.

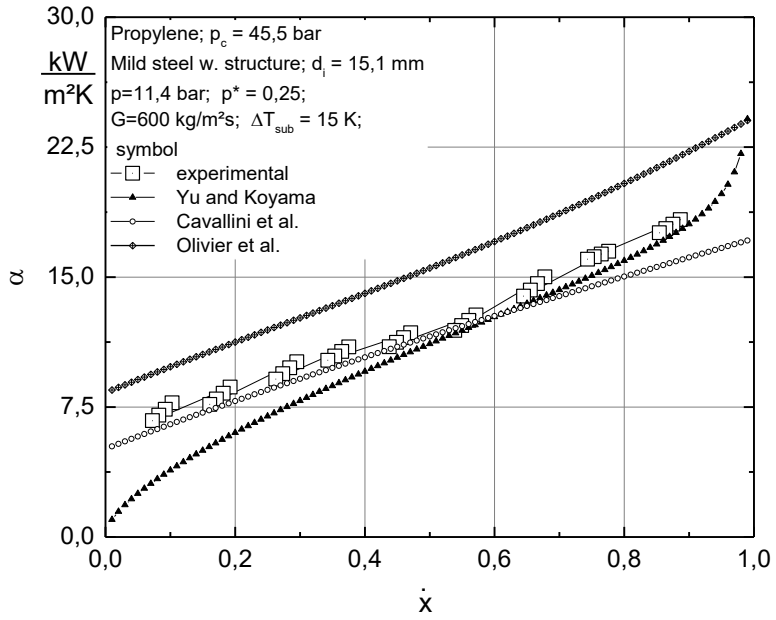

Figure 5.16: Heat transfer coefficient at $p = 11{,}4\ bar$ for $G = 600\ kg/m^2s$ over the vapor quality. Comparison between experimental data and results from Yu and Koyama [18], Cavallini et al. [17] and Olivier et al. [19] correlations

From the analysis of the plot, it is evident that Olivier et al. [19] correlation provides the higher values. The trend of the whole straight line is the most reliable, because it is parallel to the line of the experimental data for all the vapor qualities. Nevertheless, Cavallini et al. [17] correlation is the most precise prediction for $x = 0{,}1 \div 0{,}7$ because the line is almost superimposed to the experimental values, especially around $x = 0{,}5 \div 0{,}6$. Over this range, the difference between the two trends gets bigger increasing the vapor quality. As concern Yu and Koyama [18] correlation, it provides lower values of heat transfer coefficient along all the values of the vapor quality, but especially for $x = 0{,}1 \div 0{,}4$. Between $x = 0{,}5 \div 0{,}9$ the predictions are particularly close to the real experience. For $x = 0{,}9 \div 0{,}99$ and $x = 0 \div 0{,}1$ the gradient of inclination of the theoretical line changes and it is different from that provided by the other two correlations. Even if there are no data collected in these two ranges to check what would be the empirical result, it is probable that Yu and Koyama [18] correlation provides a reliable trend. In fact at high quality the heat transfer coefficients are very huge and the gradient of the curve is very steep. This

phenomenon is particularly evident with the enhanced surfaces, because the grooves promote the formation of the liquid droplets and, as a consequence, this implicates the existence of a greater region of annular flow compared to what happens normally inside a smooth tube. As Olivier et al. [19] explained, the fins redistribute the liquid layer around the circumference of the tube, forcing the flow to become annular rather than intermittent or stratified. Decreasing the vapor content between $x = 0 \div 0{,}1$ the heat transfer coefficient is expected to fast decrease faster because the fluid is almost completely composed by liquid, which floods the tube providing higher thermal resistances. The process of condensation is completed.

In Figure 5.17 the values for the heat transfer coefficient at $p = 11{,}4\ bar$ for $G = 300\ kg/m^2s$ over the vapor quality are plotted, highlighting the comparison between the experimental data and the results of the correlations.

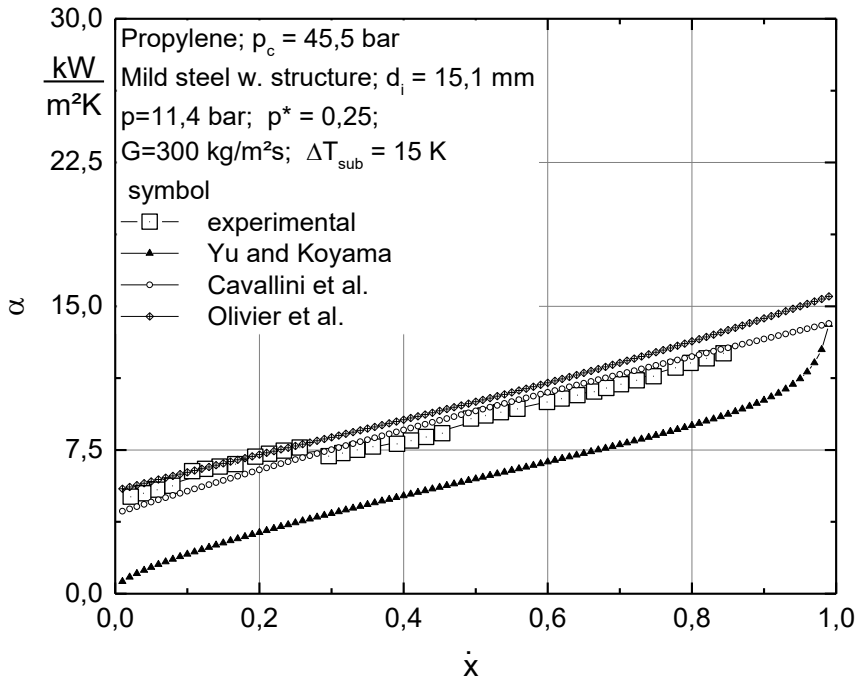

Figure 5.17: Heat transfer coefficient at $p = 11{,}4\ bar$ for $G = 300\ kg/m^2s$ over the vapor quality. Comparison between experimental data and results from Yu and Koyama [18], Cavallini et al. [17] and Olivier et al. [19] correlations

In this operative condition, both Cavallini et al. [17] and Olivier et al. [19] provide reliable results since the two curves are almost overlapped to the experimental data for each value of vapor quality. Yu and Koyama [18] correlation provides instead much lower results, but the shape of the curve between $x = 0 \div 0{,}1$ is the most reliable. In fact, in that range also the experimental data show a change in the gradient of the line.

In Figure 5.18 the values for the heat transfer coefficient at $p = 22{,}75\ bar$ for $G = 600\ kg/m^2s$ over the vapor quality are plotted, highlighting the comparison between the experimental data and the results of the correlations.

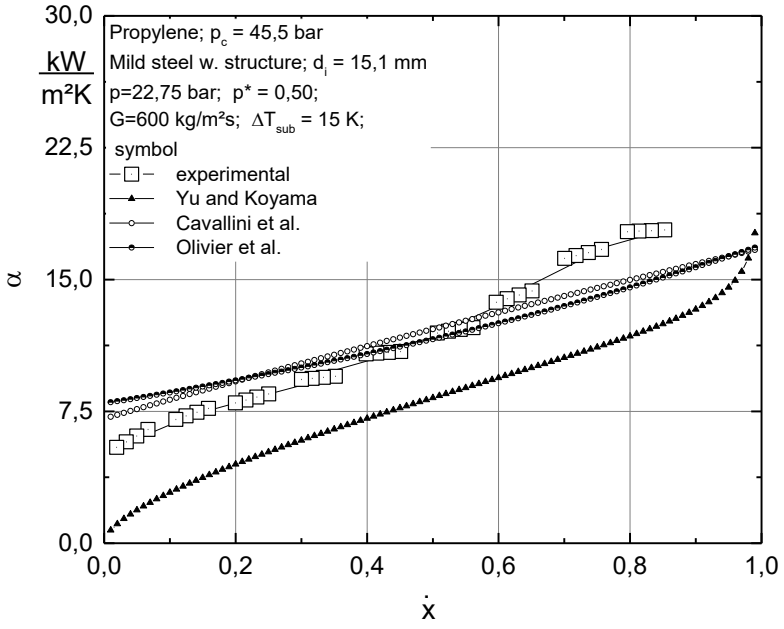

Figure 5.18: Heat transfer coefficient at $p = 22{,}75\ bar$ for $G = 600\ kg/m^2s$ over the vapor quality. Comparison between experimental data and results from Yu and Koyama [18], Cavallini et al. [17] and Olivier et al. [19] correlations

In these operative conditions, Cavallini et al. and Olivier et al. correlations provide less precise results compared to the previous cases in Figure 5.16 and Figure 5.17. In fact, they both predict in a reliable way the heat transfer coefficient value for $x = 0{,}4 \div 0{,}7$ where the lines are overlapped, but then the range of mistake becomes higher at low vapor content and even more for $x = 0{,}8 \div 0{,}9$. The biggest difference between these two predictions and the experimental trend comes from the shape of

the curves. In fact, Cavallini et al. [17] and Olivier et al. [19] predict a linear trend, while the experimental data show a change in the gradient of the curve very close to that presented by Yu and Koyama [18] increasing the amount of liquid. Despite this similarity, the range of mistake in the coefficient value is too high for the correlation to be considered reliable. In addition, for $x = 0{,}8 \div 0{,}9$ neither Yu and Koyama [18] predicted correctly the trend of the heat transfer coefficient. In general for $G = 600\ kg/m^2s$ and $p = 22{,}75\ bar$ all three correlations don't provide reliable and reliable results at high value of vapor content. After all the considerations, it can anyway be said that the correlations that provide closer results are both Cavallini et al. [17] and Olivier et al. [19].

In Figure 5.19 the values for the heat transfer coefficient at $p = 22{,}75\ bar$ for $G = 300\ kg/m^2s$ over the vapor quality are plotted, highlighting the comparison between the experimental data and the results of the correlations.

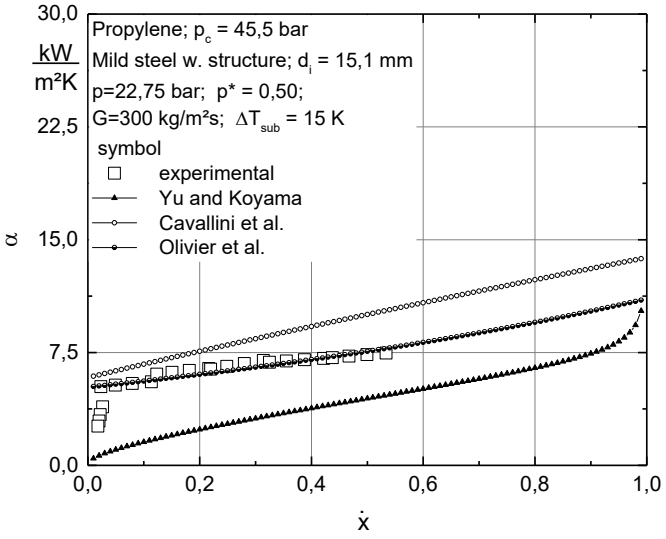

Figure 5.19: Heat transfer coefficient at $p = 22{,}75\ bar$ for $G = 300\ kg/m^2s$ over the vapor quality. Comparison between experimental data and results from Yu and Koyama [18], Cavallini et al. [17] and Olivier et al. [19] correlations

Figure 5.19 shows that, in the considered condition, the most reliable prediction is given by Olivier et al. [19] correlation. In fact, the values are overlapped for almost the whole trend. The main mistake is made at low values of vapor quality, where the experimental trend is more similar to the one predicted by Yu and Koyama [18]. As

concern the values of the coefficient in this range, they are in the middle between the Olivier et al. [19] and Yu and Koyama [18] results. For these operative conditions, the values from Cavallini et al. [17] correlation differentiate highly from the experimental results.

As a general consideration, it can be said that the precision of these predictions decreases, increasing the pressure in the system. The three used correlations were more reliable at $p = 11{,}4\ bar$ instead of $p = 22{,}75\ bar$ for both $G = 600\ kg/m^2s$ and $G = 300\ kg/m^2s$. The best prediction is given by both Cavallini et al. and Olivier et al. for $p = 11{,}4\ bar$ and $G = 300\ kg/m^2s$. It seems that Cavallini et al. and Olivier et al. can predict in a more reliable way the values of the heat transfer coefficient alternatively depending on the conditions, while Yu and Koyama [18] predict in a more precise way the overall trend of the curve.

Figure 5.20 and Figure 5.21 show the trend of the ratio between the experimental heat transfer coefficient and the calculated coefficient for Yu and Koyama [18], Cavallini et al. [17] and Olivier et al. [19] correlations as a function of the experimental heat transfer coefficient at $p = 11{,}4\ bar$, $G = 600\ kg/m^2$ and $p = 11{,}4\ bar$, $G = 300\ kg/m^2$ respectively.

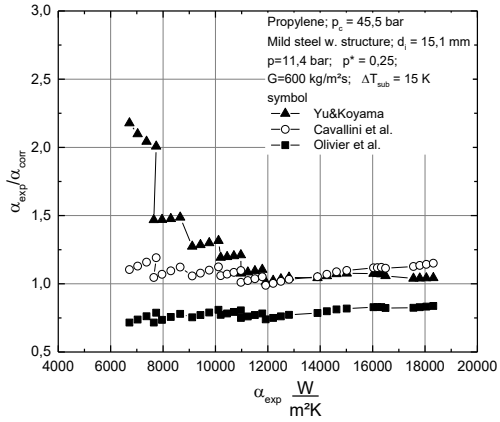

Figure 5.20: Trend of the ratio between the experimental heat transfer coefficient and the calculated coefficient by correlations as a function of the experimental heat transfer coefficient at $p = 11{,}4\ bar$ and $G = 600\ kg/m^2s$

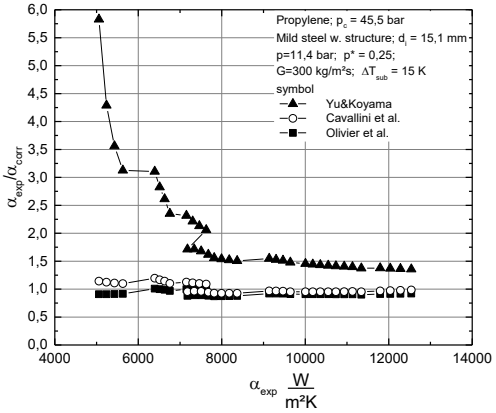

Figure 5.21: Trend of the ratio between the experimental heat transfer coefficient and the calculated coefficient by correlations as a function of the experimental heat transfer coefficient at $p = 11{,}4\ bar$ and $G = 300\ kg/m^2s$

Both the graphs show that the ratio is close to unity for all the correlations from the middle values of the coefficient to the highest values. For the lower values, the trend is respected for Cavallini et al. [17] and Olivier et al. [19], while Yu and Koyama [18] is less precise, as expected from the analysis of Figure 5.16. Considering the values provided by Yu and Koyama [18] correlation, at $G = 600\ kg/m^2$ for the lowest value of the heat transfer coefficient $\alpha_{exp} = 5057{,}65\ W/(m^2K)$, the ratio reaches the maximum value $\alpha_{exp}/\alpha_{corr} = 6$.

In Figure 5.22 an Figure 5.23 can be observed the ratio between the experimental heat transfer coefficient and the calculated coefficient for Yu and Koyama, Cavallini et al. [17] and Olivier et al. [19] correlations as a function of the experimental heat transfer coefficient at $p = 22{,}75\ bar$, $G = 600\ kg/m^2$ and $p = 22{,}75\ bar$, $G = 300\ kg/m^2$ respectively.

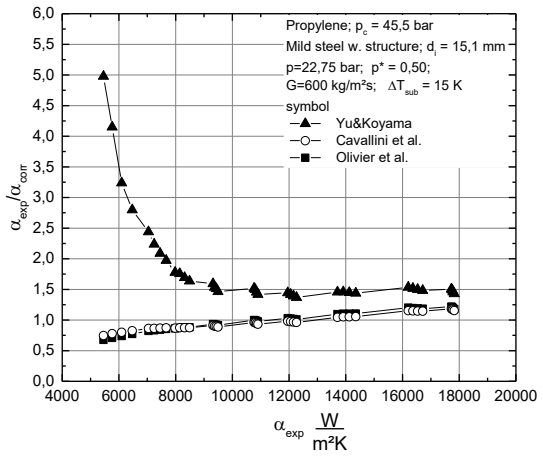

Figure 5.22: Trend of the ratio between the experimental heat transfer coefficient and the calculated coefficient for Yu and Koyama [18], Cavallini et al. [17] and Olivier et al. [19] correlations as a function of the experimental heat transfer coefficient at $p = 22{,}75\ bar$ and $G = 600\ kg/m^2$

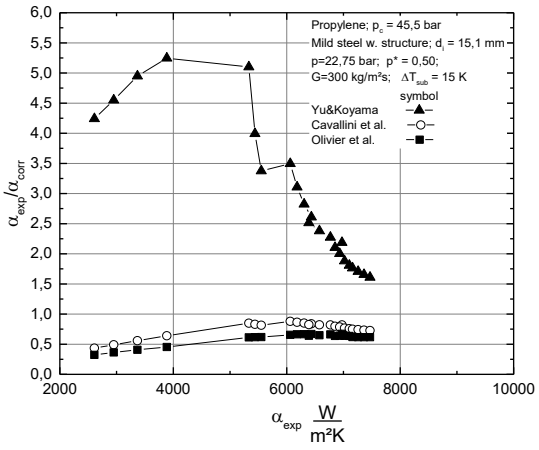

Figure 5.23: Trend of the ratio between the experimental heat transfer coefficient and the calculated coefficient for Yu and Koyama [18], Cavallini et al. [17] and Olivier et al. [19] correlations as a function of the experimental heat transfer coefficient at $p = 22{,}75\ bar$ and $G = 300\ kg/m^2$

As concern Figure 5.22, it is possible to observe that for Yu and Koyama [18] correlation the trend of the ratio decreases, increasing the experimental heat transfer coefficient, while the ratio made by the use of Olivier et al. [19] and Cavallini et al. [17] shows the opposite trend.

Figure 5.23 shows a different trend in respect of what already seen in the previous plots. Olivier et al. [19] and Cavallini et al. [17] ratio increases with the increase of the experimental heat transfer coefficient, while Yu and Koyama [18] ratio starts to increase, reaches the maximum ratio $\alpha_{exp}/\alpha_{corr} = 5{,}25$ at $\alpha_{exp} = 3885{,}5\ W/(m^2K)$ and than decreases. Both ratios given by Olivier et al. [19] and Cavallini et al. [17] remain below zero for the whole range of $\alpha_{exp} = 2608 \div 7468\ W/(m^2K)$.

As a general consideration from the analysis of Figure 5.20, Figure 5.21, Figure 5.22 and Figure 5.23, it can be said that in all the studied operating conditions, in an approximate range of $\alpha_{exp} = 2600 \div 6500\ W/(m^2K)$ the ratio given by Yu and

Koyama [18] is between $\alpha_{exp}/\alpha_{corr} = 6 \div 2{,}5$. Considering the present case of study, this correlation proves more appropriate for higher alpha values. Both ratios given by Olivier et al. [19] and Cavallini et al. [17] remain close to unity for every value of heat transfer coefficient in the whole conditions, with no particular differences between them.

Figure 24, Figure 25, Figure 26, Figure 27 give a practical visualization of the error range of the coefficient prediction compared to the data collected under different operating conditions, plotting the experimental heat transfer coefficient over the heat transfer coefficient calculated through the Yu and Koyama [17], Cavallini et al. [17] and Olivier et al. [19] correlations.

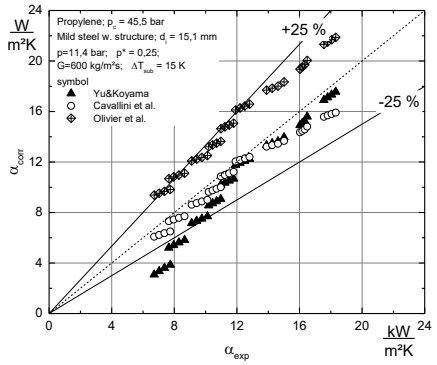

Figure 5.24: Range of divergence between experimental heat transfer coefficient and data derived from correlations at $p = 11{,}4\ bar$ and $G = 600\ kg/m^2$

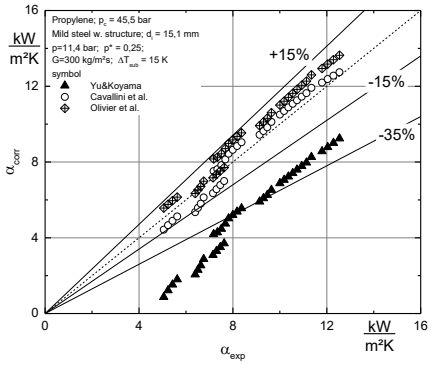

Figure 5.25: Range of divergence between experimental heat transfer coefficient and data derived from correlations at $p = 11{,}4\ bar$ and $G = 300\ kg/m^2$

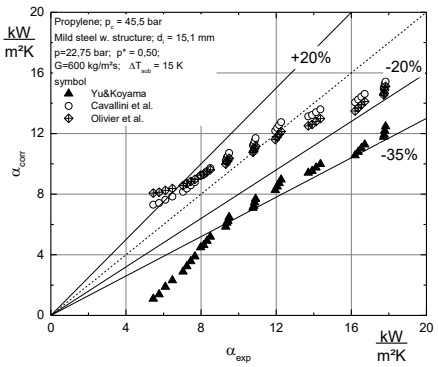

Figure 5.26: Range of divergence between experimental heat transfer coefficient and data derived from correlations at $p = 22{,}75\ bar$ and $G = 600\ kg/m^2$

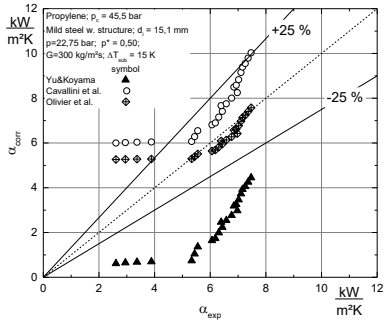

Figure 5.27: Range of divergence between experimental heat transfer coefficient and data derived from correlations at $p = 22{,}75\ bar$ and $G = 300\ kg/m^2$

Considering all the plots, the spread of data is generally between $15 \div 25\%$ over or under the bisector, that represents the exact coincidence of results and experimental data. The exception occurs for Yu and Koyama [18] results, since it normally provides values between -35% or more, except for the tests at $p = 11{,}4\ bar$, $G = 600\ kg/m^2$.

5.4.2 Pressure losses

In this section, the comparison between the experimental data collected and the expected results from the use of mathematical correlations is made. In particular, the correlations of Haraguchi et al. [23] and Cavallini et al. [22] already presented in Chapter 2.3 are used, but also the correlation of Olivier et al. [19] is employed. The data refer to the pressure losses calculated in one meter tube length, for values of vapor content at the entrance of the test tube $x = 0{,}1 \div 0{,}9$ with steps of $0{,}1$ unities.

In Figure 5.28, Figure 5.29, Figure 5.30 and Figure 5.31 the values for the pressure losses over the vapor quality are plotted, highlighting the comparison between the experimental data and the results of the correlations, respectively at $p = 11{,}4\ bar$, $G = 600\ kg/m^2s$, at $p = 11{,}4\ bar$, $G = 300\ kg/m^2s$, at $p = 22{,}75\ bar$, $G = 600\ kg/m^2s$, at $p = 22{,}75\ bar$, $G = 300\ kg/m^2s$.

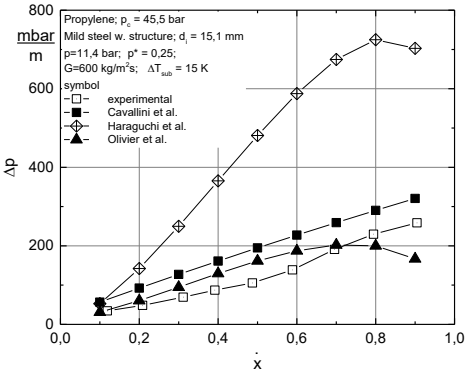

Figure 5.28: Pressure losses at $p = 11{,}4\ bar$, $G = 600\ kg/m^2s$ over the vapor quality. Comparison between experimental data and results given by Haraguchi et al. [23], Cavallini et al. [22] and Olivier et al. [19]

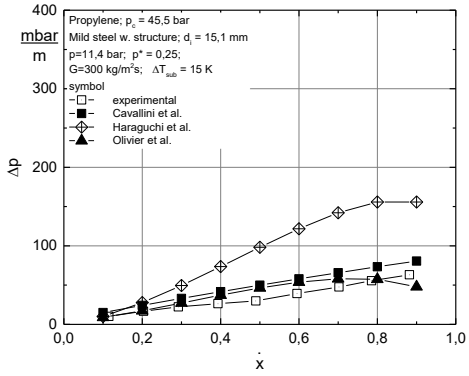

Figure 5.29: Pressure losses at $p = 11{,}4\ bar$, $G = 300\ kg/m^2s$ over the vapor quality. Comparison between experimental data and results given by Haraguchi et al. [23], Cavallini et al. [22] and Olivier et al. [19]

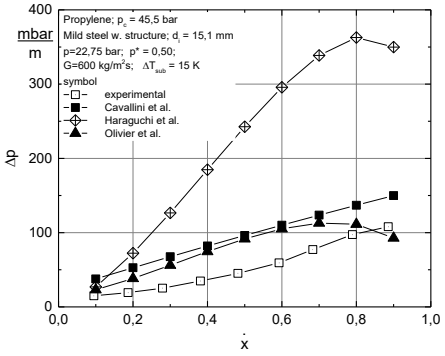

Figure 5.30: Pressure losses at $p = 22{,}75\ bar$, $G = 600\ kg/m^2s$ over the vapor quality. Comparison between experimental data and results given by Haraguchi et al. [23], Cavallini et al. [22] and Olivier et al. [19]

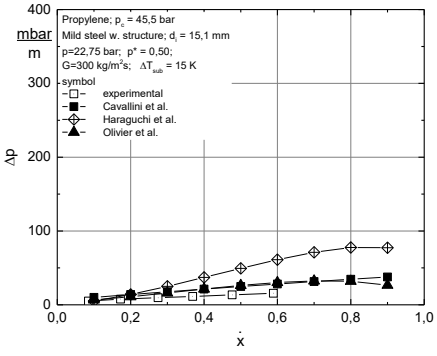

Figure 5.31: Pressure losses at $p = 22{,}75\ bar$, $G = 300\ kg/m^2s$ over the vapor quality. Comparison between experimental data and results given by Haraguchi et al. [23], Cavallini et al. [22] and Olivier et al. [19]

From the global analysis of all graphs, it is evident that the pressure losses increase at higher values of vapor quality, as expected. In fact, at high values of vapor content, the fluid is mainly composed by vapor, the velocity is high such as the turbulence, so the pressure losses are significant. In addition, this case of study employs a micro-fin tube that increases the chaos in the system through the presence of the enhanced structures. At low values of vapor quality, the velocities are lower and pressure losses are correspondingly low. Moreover, the tube is flooded, so the effect of the fins is less relevant.

Considering the prediction of the pressure losses given by Haraguchi [23], it is evident that the results obtained are considerable huger in respect of the measurement and in respect of the other correlations prediction, especially at high vapor quality. The worst prediction is given for the operating condition of $p = 11{,}4\ bar$, $G = 600\ kg/m^2s$, as it is evident considering Figure 5.28. In this case, at $x = 0{,}9$, the difference between the value predicted and the value calculated is $444\ mbar/m$. The experimental experience shows that the penalty in terms of pressure losses in the system is much less relevant. Probably, this correlation suggests greater importance to the presence of the fins and at the same time it could also consider a huger influence of the change of the flow regime inside the tube at high vapor quality. At high vapor quality the prediction shows an accentuated decrease of the gradient of the slope. This effect is explained by Cavallini et al. [24], since at high vapor quality the flow pattern tends to be annular and to be dominated by the tangential force between vapor and liquid film. In the experimental experience, this trend is confirmed, but it's less evident.

The correlations of Cavallini et al. [22] and of Olivier et al. [19] fit the experimental data in a much more reliable way. The values provided are close to the empirical experience, but the trend of the curve doesn't precisely follow the experimental line, especially when there is a change in the inclination, as it can be seen in Figure 5.30.

In general, all the correlations predict higher values than the experimental values.

Figure 32, Figure 33, Figure 34, Figure 35 give a practical visualization of the error range of the coefficient prediction compared to the data collected under different operating conditions, plotting the experimental heat transfer coefficient over the heat transfer coefficient calculated through the Haraguchi et al. [23], Cavallini et al. [22] and Olivier and al. [19] correlations.

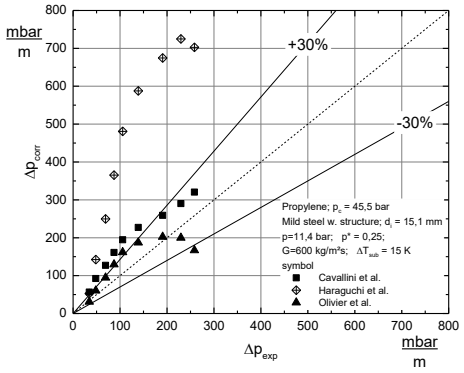

Figure 5.32: Range of divergence between experimental pressure losses and results derived from correlations at $p = 11{,}4\ bar$ and $G = 600\ kg/m^2$

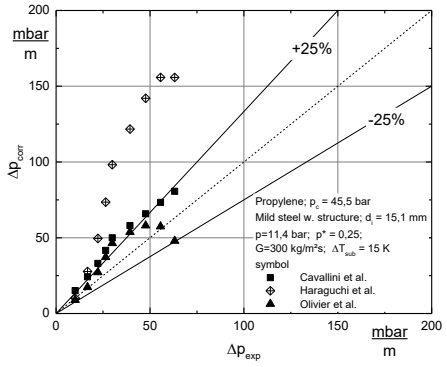

Figure 5.33: Range of divergence between experimental pressure losses and results derived from correlations at $p = 11{,}4\ bar$ and $G = 300\ kg/m^2$

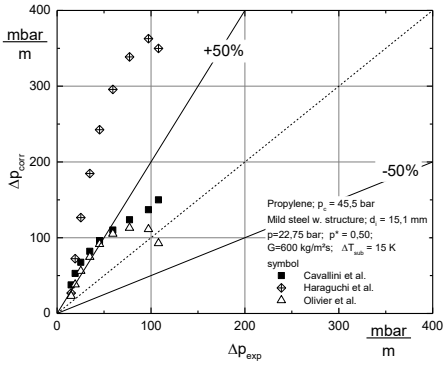

Figure 5.34: Range of divergence between experimental pressure losses and results derived from correlations at $p = 22{,}75\ bar$ and $G = 600\ kg/m^2$

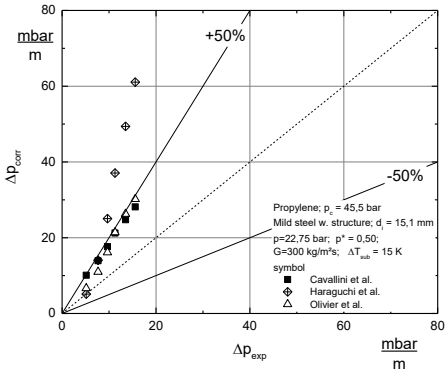

Figure 5.35: Range of divergence between experimental pressure losses and results derived from correlations at $p = 22{,}75\ bar$ and $G = 300\ kg/m^2$

From the analysis of all the plots it is evident that Cavallini et al. [22] and Olivier et al. [19] correlations provide good results with a range of spread between $25 \div 30\%$ at $p = 11{,}4\ bar$, while at $p = 22{,}75\ bar$ the divergence is around 50%. Haraguchi et al. [23] correlation doesn't suit the case of study.

5.5 Comparison between smooth and micro-fin tubes

In this section, the data of the heat transfer coefficient and the pressure losses measured and collected for smooth are validated by the use of Thome et al. [15] and Shah [16] correlations. Then, the data collected for smooth and micro-fin tubes are compared, to highlight the effect of the micro-structures in the physics of the heat transfer, in order to consider the advantages and disadvantages of both the possibilities considered.

To collect the data for the smooth tube, the same facility with the same configuration is used but a different tube is located in place of the micro-fin tube. The new tube is made of mild steel, with an inner diameter $d_i = 14{,}65\ mm$.

5.5.1 Heat transfer coefficient

Figure 5.36 and Figure 5.37 show the data collected and the results obtained by the use of Thome et al. [15] and Shah [16] correlations, respectively at $p = 11{,}4\ bar$ and at $p = 22{,}75\ bar$, for both $G = 600\ kg/m^2s$ and $G = 300\ kg/m^2s$.

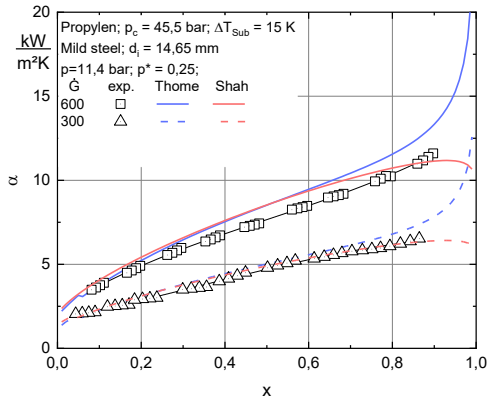

Figure 5.36: Heat transfer coefficient experimentally collected and achieved by the use of Thome et al. [15] and Shah [16] correlations at $p = 11{,}4\ bar$ for $G = 600\ kg/m^2s$ and $G = 300\ kg/m^2s$

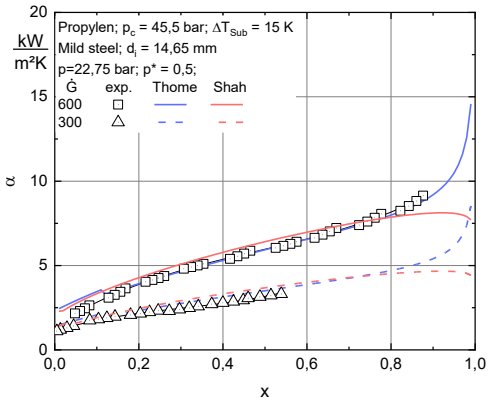

Figure 5.37: Heat transfer coefficient experimentally collected and achieved by the use of Thome et al. [15] and Shah [16] correlations at $p = 22{,}75\ bar$ for $G = 600\ kg/m^2s$ and $G = 300\ kg/m^2s$

The experimental data accord for both the predictions in the considered range $x = 0{,}1 - 0{,}9$. From $x = 0{,}9$, the correlations predict two different trends. Thome et al. [15] correlation predicts a continue exponential increase of the heat transfer coefficient until $x = 1$, while Shah [16] considers a decrement in this range. Measurements were not carried out in this range of vapor quality, so for this reason it is not possible to establish with extreme certainty what trend should be expected at the highest vapor content values, but it is possible to assume that Thome et al. [15] provides the most accurate data, because all the experimental data seem much more consistent with this case.

Figure 5.38, Figure 5.39, Figure 5.40 and Figure 5.41 show the comparison between the heat transfer coefficient for the micro-fin and the smooth tube respectively at $p = 11{,}4\ bar,\ G = 600\ kg/m^2s,$ at $p = 11{,}4\ bar,\ G = 300\ kg/m^2s,$ at $p = 22{,}75\ bar,\ G = 600\ kg/m^2s$, at $p = 22{,}75\ bar$, $G = 300\ kg/m^2s$.

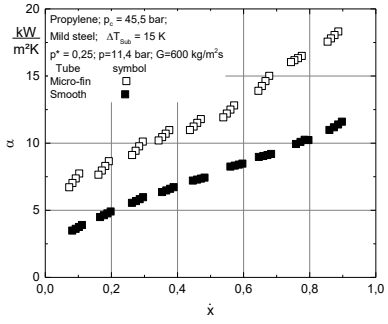

Figure 5.38: Comparison of heat transfer coefficient for micro-fin and smooth tube at $p = 11{,}4\ bar$, $G = 600\ kg/m^2s$

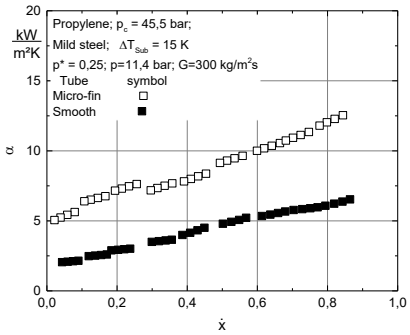

Figure 5.39: Comparison of heat transfer coefficient for micro-fin and smooth tube at $p = 11{,}4\ bar$, $G = 300\ kg/m^2s$

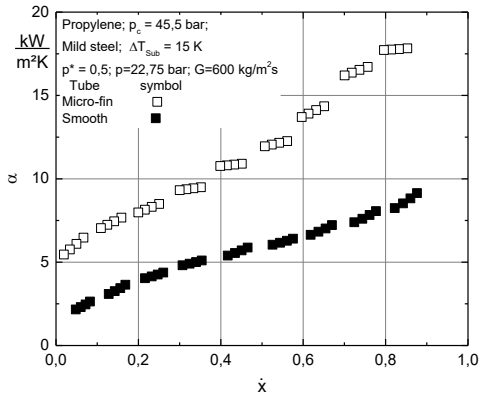

Figure 5.40: Comparison of heat transfer coefficient for micro-fin and smooth tube at $p = 22{,}75\ bar$, $G = 600\ kg/m^2s$

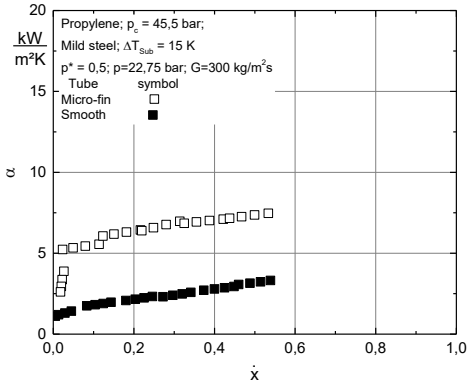

Figure 5.41: Comparison of heat transfer coefficient for micro-fin and smooth tube at $p = 22{,}75\ bar$, $G = 300\ kg/m^2s$

The analysis of all the graphs clearly shows the advantage of using the micro finned tube, since the values achieved for the heat transfer coefficient are considerably huger for all the values of the mass flux. This effect is even more visible at high values of vapor quality, around $x = 0{,}5 \div 0{,}9$. As it can be seen in Figure 5.38, Figure 5.39 and in Figure 5.40, the curve associated with the micro-fin tube data begins to have a steeper inclination in this range. That means the influence of the enhanced structures is more relevant when the fluid is mainly composed by vapor. In fact, the presence of the fins is particularly effective in the promotion of the formation of the liquid drops all around the circumference of the tube and the consequent establishment of the annular flow. Moreover, since the micro-structures inside the tube increase the turbulence, the consequent improving in the heat transfer process is concrete. This trend would probably also be confirmed by the data shown in Figure 5.41, if it had been possible to make the measurements up to $x = 0{,}9$. Referring to the case of Figure 5.41 in particular, Pate et al. [26] give an explanation of the advantage of structured fins when low mass fluxes are employed. Considering also previous studies, they concluded that, in general, the presence of the spiral flow reduces the stratified flow region, but in particular at low flow rates, where stratified flow might otherwise occur, the spiraled fins cause the upper surface to be wetted, thus producing a thin liquid film on the grooved wall. In that study, for the same

conditions the smooth tube upper wall was dried during stratified flow, so the presence of the liquid film enhanced heat transfer. The consideration comes from a concrete comparison between flow-pattern maps for a smooth tube with photographs of the fluid inside a micro-fin tube [26].

The advantage in the use of the micro-fin tube can be seen through the graphs in Figure 5.42, Figure 5.43, Figure 5.44 and Figure 5.45. They show the percentage increase of the heat transfer coefficient using the micro-fin tube instead of the smooth tube respectively at $p = 11{,}4\ bar$, $G = 600\ kg/m^2s$, at $p = 11{,}4\ bar$, $G = 300\ kg/m^2s$, at $p = 22{,}75\ bar$, $G = 600\ kg/m^2s$, at $p = 22{,}75\ bar$, $G = 300\ kg/m^2s$.

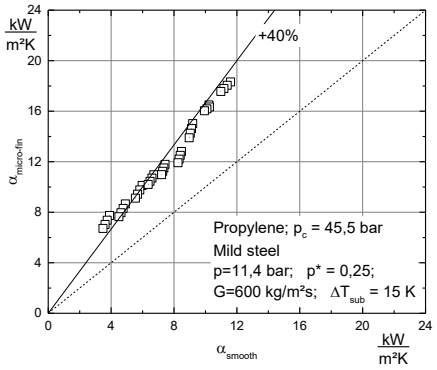

Figure 5.42: Percentage increase of the heat transfer coefficient value due to the use of the finned compared to the smooth tube at $p = 11{,}4\ bar$, $G = 600\ kg/m^2s$

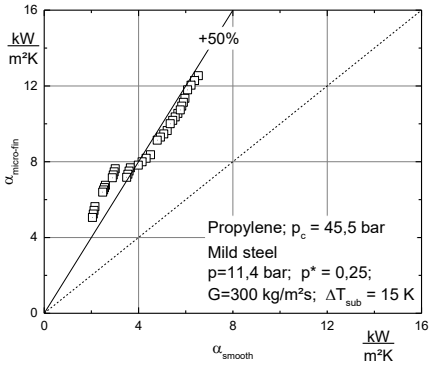

Figure 5.43: Percentage increase of the heat transfer coefficient value due to the use of the finned compared to the smooth tube at $p = 11{,}4\ bar$, $G = 300\ kg/m^2s$

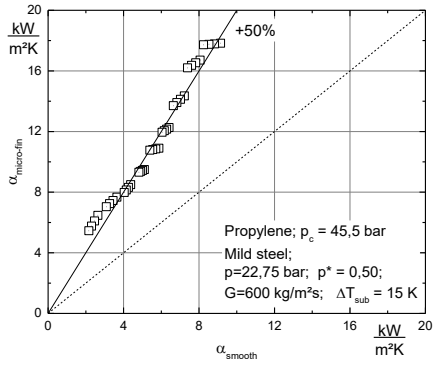

Figure 5.44: Percentage increase of the heat transfer coefficient value due to the use of the finned compared to the smooth tube at $p = 22{,}75\ bar$, $G = 600\ kg/m^2s$

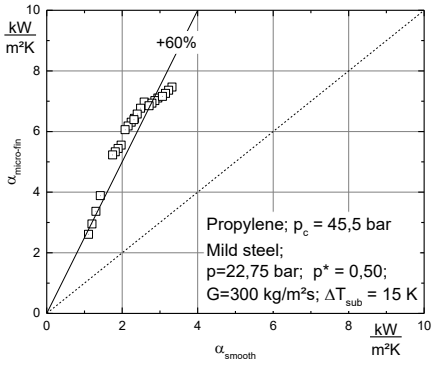

Figure 5.45: Percentage increase of the heat transfer coefficient value due to the use of the finned compared to the smooth tube at $p = 22{,}75\ bar$, $G = 300\ kg/m^2s$

The benefit of micro-structures is considerable because the increase in the coefficient in the worst case is between $15 \div 30\%$, at $p = 11{,}4\ bar$, $G = 600\ kg/m^2s$ in Figure 5.42. Considering the tests ran at $p = 22{,}75\ bar$, Figure 5.44 and Figure 5.45, the increment is even bigger and for $G = 600\ kg/m^2s$ achieve $+45\%$. Considering the global trend, the best result is obtained at $p = 22{,}75\ bar$, $G = 300\ kg/m^2s$, because most of the values are positioned on the straight line at $+40\%$. That means that the increase of the coefficient is huge and the trend doesn't particularly change in relation to the value of the vapor quality. The reason that explains this behavior has already been given above for Figure 5.9 in Section 5.3.1 and for Figure 5.41, referring to the influence of the fins at low values of the mass flux [26].

To evaluate the convenience in the use of the micro-fin tubes in respect of the smooth tube, the enhancement factor *EH* is normally used. It is a parameter obtained by the ratio between the heat transfer coefficient for a micro-fin and that of a smooth tube at the same operating condition and maximum inside diameter [27], as it can be seen in Equation 5.1.

$$EH = \frac{\alpha_{micro-fin}}{\alpha_{smooth}} \tag{5.1}$$

Figure 5.46 shows the enhancement factor over the quality vapor for the different operating conditions related to the four experiments. For each value of vapor quality, four points are plotted, one for each measurement section along the tube length.

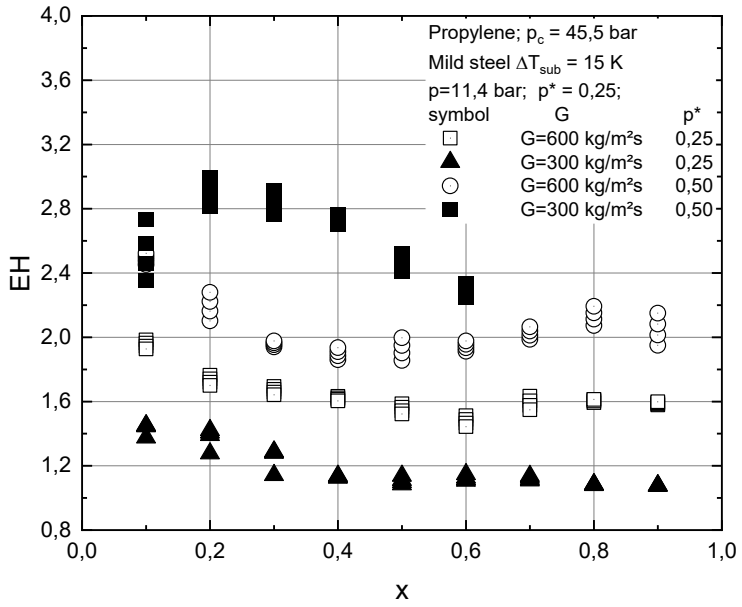

Figure 5.46: Enhancement factor over the vapor quality

The overall results of the enhancement factor *EH* are contained within a range $1.2 - 3$. The parameter is almost constant as the vapor quality varies for a given operating condition, since the range within which the variation of *EH* occurs as the vapor content varies is around $0{,}4$. The maximum benefit is achieved at the condition of $p = 22{,}75\ bar$, $G = 300\ kg/m^2s$ where the enhancement factor is the range $EH = 2{,}2 - 3$ for the range of vapor quality $x = 0{,}1 - 0{,}6$.

5.5.2 Pressure losses

Figure 5.47 and Figure 5.48 show the data collected and the results obtained by the use of Friedel [20] and Müller et al. [21] correlations, respectively at $p = 11{,}4\ bar$ and at $p = 22{,}75\ bar$, for both $G = 600\ kg/m^2s$ and $G = 300\ kg/m^2s$.

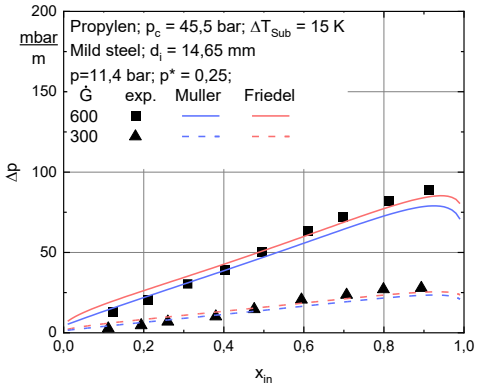

Figure 5.47: Pressure losses experimentally collected and achieved by the use of Friedel [20] and Müller et al. [21] correlations at $p = 11{,}4\ bar$ for $G = 600\ kg/m^2s$ and $G = 300\ kg/m^2s$

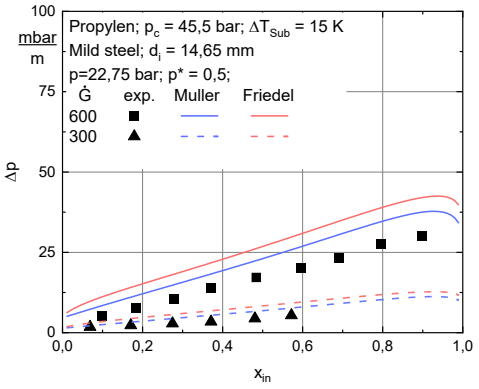

Figure 5.48: Pressure losses experimentally collected and achieved by the use of Friedel [20] and Müller et al. [21] correlations at $p = 22{,}75\ bar$ for $G = 600\ kg/m^2s$ and $G = 300\ kg/m^2s$

The data in all the cases are validated by the use of the correlations. The most reliable predictions are given at the lowest pressure value $p = 11{,}4\ bar$ for both the mass fluxes considered.

Figure 5.49, Figure 5.50, Figure 5.51 and Figure 5.52 show the comparison between the pressure losses for the micro-fin and the smooth tube respectively at $p = 11{,}4\ bar$, $G = 600\ kg/m^2s$, at $p = 11{,}4\ bar$, $G = 300\ kg/m^2s$, at $p = 22{,}75\ bar$, $G = 600\ kg/m^2s$, at $p = 22{,}75\ bar$, $G = 300\ kg/m^2s$.

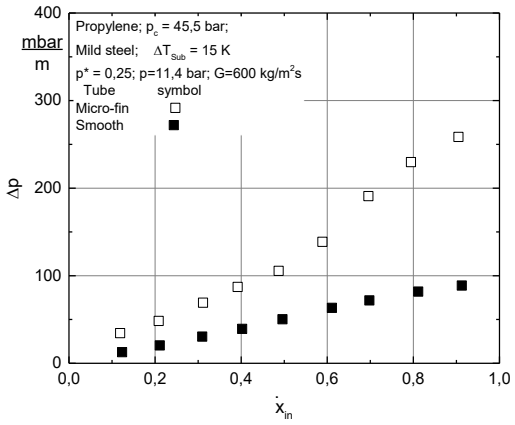

Figure 5.49: Comparison of pressure losses for micro-fin and smooth tube at $p = 11{,}4\ bar$, $G = 600\ kg/m^2s$

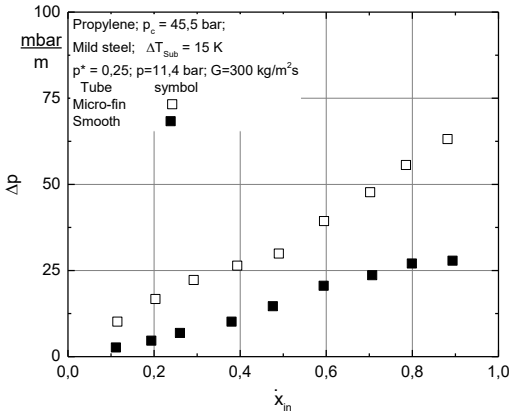

Figure 5.50: Comparison of pressure losses for micro-fin and smooth tube at $p = 11{,}4\ bar$, $G = 300\ kg/m^2s$

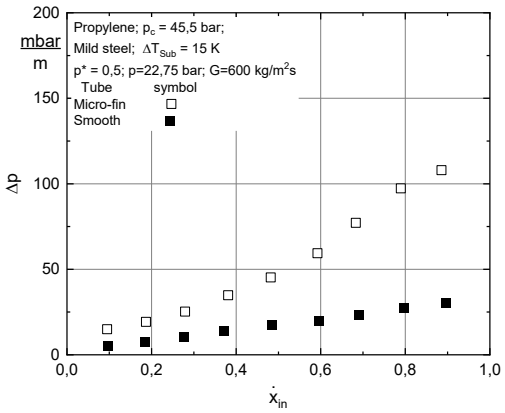

Figure 5.51: Comparison of pressure losses for micro-fin and smooth tube at $p = 22{,}75\ bar$, $G = 600\ kg/m^2s$

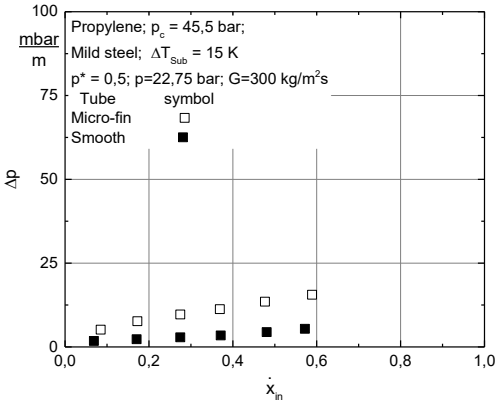

Figure 5.52: Comparison of pressure losses for micro-fin and smooth tube at $p = 22{,}75\ bar$, $G = 300\ kg/m^2s$

Since the enhanced structures promote the turbulence inside the tube, higher pressure losses are expected and measured in comparison with the data acquired for the smooth tube. Especially at higher values of vapor quality, the friction between the two phases of the fluid is huge since the velocity of the vapor is more relevant, and structures have a considerable impact in creating a chaotic flow. At lower values of

vapor quality, the tube is flooded and therefore the influence of the fins is so small as to be considered almost negligible.

To better understand the impact of the micro structures inside the tube, Figure 5.53, Figure 5.54, Figure 5.55 and Figure 5.56 show the plot of the micro-fin tube pressure losses over the smooth tube pressure losses respectively at $p = 11{,}4\ bar$, $G = 600\ kg/m^2s$, at $p = 11{,}4\ bar$, $G = 300\ kg/m^2s$, at $p = 22{,}75\ bar$, $G = 600\ kg/m^2s$, at $p = 22{,}75\ bar$, $G = 300\ kg/m^2s$. The incremental percentage of the drop is highlighted, referring to the bisector of the plot that represents the place where the data would lie if they matched in the two cases.

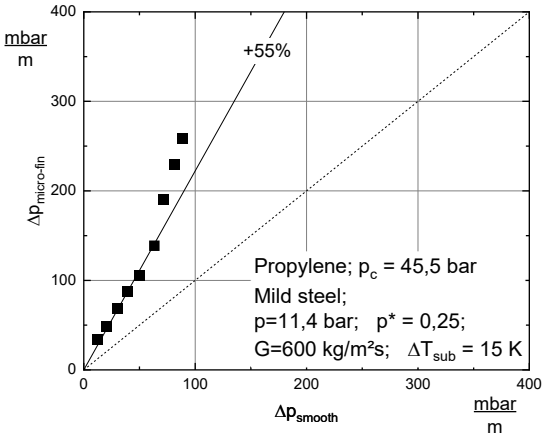

Figure 5.53: Percentage increase of the pressure losses value due to the use of the finned compared to the smooth tube at $p = 11{,}4\ bar$, $G = 600\ kg/m^2s$

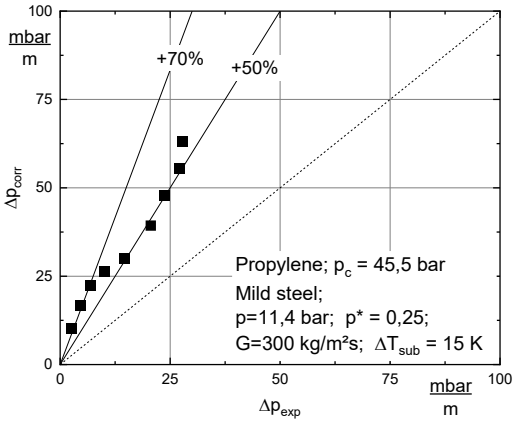

Figure 5.54: Percentage increase of the pressure losses value due to the use of the finned compared to the smooth tube at $p = 11{,}4\ bar$, $G = 300\ kg/m^2s$

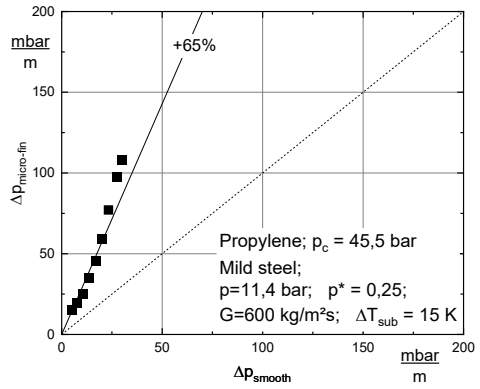

Figure 5.55: Percentage increase of the pressure losses value due to the use of the finned compared to the smooth tube at $p = 22{,}75\ bar$, $G = 600\ kg/m^2s$

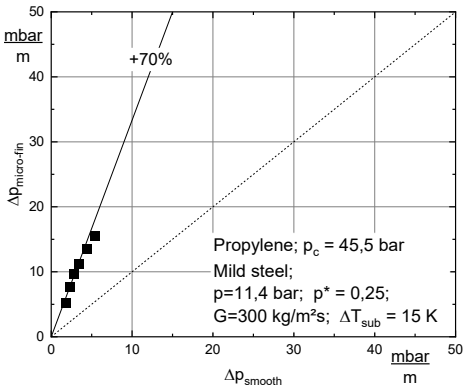

Figure 5.56: Percentage increase of the pressure losses value due to the use of the finned compared to the smooth tube at $p = 22{,}75\ bar$, $G = 300\ kg/m^2s$

It can be seen that the percentual increase of losses is significant, between $50 - 70\%$. In general, even if the percentual increase is high the amount of losses is not extremely penalizing, considering that the absolute value of pressure losses is in the order of millibar while the pressure system is set at $p = 11{,}4\ bar$ or at $p = 22{,}75\ bar$. Moreover, at $G = 600\ kg/m^2s$ both for $p = 11{,}4\ bar$ and $p = 22{,}75\ bar$ the percentual increase changes over the vapor quality, in fact the data don't lie on the same line for values greater than $x = 0{,}7$, as it can be seen in Figure 5.53 and 5.55. A difference occurs in Figure 5.54 for $G = 300\ kg/m^2s$, because the data lie in a huge range. It's not possible to compare with the other case in Figure 5.56, because there the data are only available up to $x = 0{,}7$ and therefore it is not possible to say whether the deviation depends on the value of the mass flow or whether there are other reasons.

To evaluate the penalty in the use of the micro-fin tubes in respect of the smooth tube, the pressure drop ratio factor *PDR* is normally used. It represents the ratio between frictional pressure drop per unit length of a micro-fin tube and that of a smooth tube at the same maximum inside diameter and operating conditions [27], as it can be seen in Equation 5.2.

$$PDR = \frac{\Delta p_{micro-fin}}{\Delta p_{smooth}} \tag{5.2}$$

Figure 5.57 shows the pressure drop ratio over the quality vapor for the different operating conditions related to the four experiments.

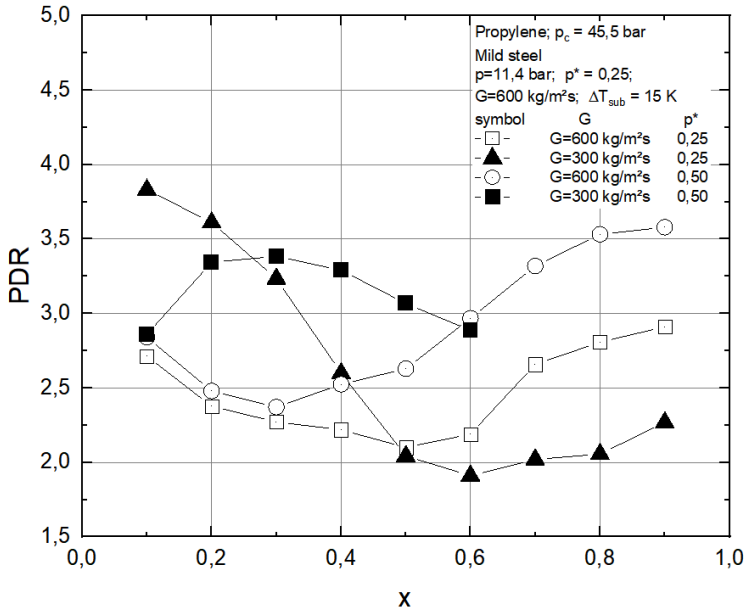

Figure 5.57: Pressure drop ratio over the vapor quality

The trend of the pressure drop ratio is different for each operating condition, but as a general consideration it can be said that for $G = 600\ kg/m^2s$ there is a small decrease starting from the low value of vapor quality, but then the *PDR* increases again, reaching the maximum for $x = 0{,}9$. For $G = 300\ kg/m^2s$ the trend is pretty high for low value of vapor content, reaches the minimum for $x = 0{,}6$ and then increases again for a small amount.

6 CONCLUSIONS

The present work was focused on the investigation of the in-tube heat transfer coefficient and pressure drop that occur inside a micro-fin tube during a condensation process that takes place through the heat transferred between a hot vapor of propylene and a cooling oil flowing in counter-flow. The main interest lies in studying the influence of fins during the condensation process, since the presence of enhanced surface areas has beneficial effects on the condensation mechanism, although it entails increased pressure losses as a disadvantage.

The test section is equipped with sensors to measure pressure and temperature and it is connected to a test rig that provides and regulates operating parameters such as steam content and volume flow. Before starting the experiments, several tests meant to prove the functioning of the test rig have been performed, with a particular attention to the accuracy of the temperature sensors.

The measurements have carried out for two values of pressure, $p = 11{,}4\ bar$ and $p = 22{,}75\ bar$ at two different mass fluxes $G = 600\ kg/m^2s$ and $G = 300\ kg/m^2s$. The experiments regard partial condensation inside a $2{,}4\ m$ length test tube with a diameter of $d = 15{,}1\ mm$, and all of them have been carried out for values of vapor quality at inlet considered in a range of $x = 0{,}1 - 0{,}9$, with steps of $0{,}1$ unities.

The heat transfer coefficient and the pressure drop were plotted as a function of the vapor quality in the different operating conditions, studying the influence of pressure and mass flow on the mechanism. It has been shown that increasing the mass flow is very beneficial, as higher velocity leads to more turbulence and chaos inside the tube, which effectively promotes heat transfer.

A literature review has been carried out in the first part of the present work, with the aim of studying and presenting the actual knowledge of the heat transfer mechanism during condensation. The flow pattern map by Taitel and Dukler [2] is discussed, and some correlations for the prediction of the variables of interest have been described, with the purpose to compare the mathematical results and the empirical data collected in order to validate the experimental data. Cavallini et al. [17] and Olivier et al. [19] correlations are adherent to the case study, providing results of the heat transfer coefficient value in a range of uncertainty between $15 - 25\%$. Pressure drops were reliably predicted through Cavallini et al. [22] and Olivier et al. [19] correlations, within a range of $30 - 50\%$.

To better understand the influence of the use of micro finned tubes, the same tests have been also conducted for a smooth tube, with an inner diameter $d = 14{,}65\ mm$. The data are validated through the correlations of Thome et al. [15] and Shah [16] for the heat transfer coefficient, and though Friedel [20] and Müller et al. [21] for the pressure drop. In both cases, they all can be considered very precise for the case considered. Then the comparison between the data for the smooth tube and the finned tube is carried out for both alpha and pressure losses as a function of vapor quality.

An immediate perception of the advantages and disadvantages of using a micro-finned tube can be obtained through the use of two parameters *EH* and *PDR*, which respectively indicate the ratio between the heat transfer coefficient and the pressure losses for a micro-fin and that of a smooth tube at the same operating condition and maximum inside diameter [27]. Both the enhancement factor *EH* and the penalty factor *PDR* are plotted as function of vapor quality. The *EH* gives results between $1.2 - 3$ and it is almost constant as the vapor quality varies for a given operating condition. The best result is obtained for $G = 300\ kg/m^2s$ at $p = 22{,}75\ bar$. The penalty factor *PDR* shows a more complicated trend varying the vapor quality, but the overall results are contained within the range $2 - 3{,}75$.

The use of micro-finned tubes is advantageous from the point of view of increasing the heat exchange coefficient, but the penalty resulting from pressure drops has to be considered. The choice has to be made considering the final application.

7 REFERENCES

[1] Dvora Barnea, Ovadia Shoham, Yehuda Taitel, A.E. Dukler: Flow pattern transition for gas-liquid flow in horizontal and inclined pipes. Int. J. Multiphase Flow Vol. 6, pp. 217-225, 1980

[2] Yemada Taitel, A.E. Dukler: A model for predicting flow regime transitions in horizontal and near horizontal gas-liquid flow. AIChE Journal, 22(1):47-55, 1976

[3] J.El Haja, J.R. Thome, A. Cavallini: Condensation in horizontal tubes, part 1: the two-phase flow pattern map. International Journal of Heat and Mass Transfer, Volume 46, Issue 18, Pages 3349-3363, 2003

[4] T.N. Tandon, H.K. Varma, C.P. Gupta: A new flow regime map for condensation inside horizontal tubes. J. Heat Transfer 104, 471-768, 1982

[5] R.G. Sardasei, R.G. Owen, D.J. Pulling: Flow regimes for condensation of a vapour inside horizontal tube. Chem. Eng. Sci. 36, 1173-1180, 1981

[6] M.K. Dobson, J.C. Chato: Condensation in smooth horizontal tubes. J. Heat Mass Transfer 22, 547-556, 1979

[7] N. Katta, J.R. Thome, D. Favrat: flow boiling in horizontal tubes: Part 1-Development od diabatic two-phase flow pattern map. J. Heat Transfer 120, 140-147, 1998

[8] L. Rossetto: Dispense di Trasmissione del calore e Termofluidodinamica, 2020

[9] A. Cavallini, D. Del Col, L. Doretti, G.A. Longo, L. Rossetto: Heat transfer and pressure drop during condensation of refrigerants inside horizontal enhanced tubes. International Journal of Refrigeration 23, Pages 4-25, 2000

[10] Yang CY, Webb RL.: A predictive model for condensation in small hydraulic diameter tubes having axial micro-fins. J Heat Transfer, 119:776-82, ASME Trans 1997

[11] Jonathan A. Olivier, Leon Liebenberg, John R. Thome, Josua P. Meyer: Heat transfer, pressure drop, and flow pattern recognition during condensation inside smooth, helical micro-fin, and herringbone tubes. International Journal of Refrigeration, Volume 30, Issues 4, Pages 609-623, 2007

[12] M.A. Akhavan-Behabadi, Ravi Kumar, S.G. Mohseni: Condensation heat transfer of R-134a inside a microfin tube with different tube inclinations. International Journal of Heat Transfer and Mass Transfer, Volume 50, Issues 23-24, Pages 4864-4871, 2007

[13] Akio Miyara, Kengo Nonaka, Mitsunori Taniguchi: Condensation heat transfer and flow pattern inside herringbone-type micro-fin tube. International Journal of Refrigeration, Volume 23, Issue 2, Pages 141-152, 2000

[14] Ralph L. Webb, Nae-Hyun Kim: Principles of Enhanced Heat Transfer. Taylor and Francis Group, New York, 2005

[15] J.R. Thome, J. El Hajal, A. Cavallini: Condensation in horizontal tubes, part 2: new heat transfer model based on flow regimes. International Journal of Heat Trasfer 46, 3365-3387, 2003

[16] Mirza M. Shah: Comprehensive correlations for heat transfer during condensation in conventional and mini/micro channels in all orientations. International Journal of Refrigeration 67, 22-41, 2016

[17] A. Cavallini, D. Del Col, L. Doretti, G.A. Longo, L. Rossetto: Heat transfer and pressure drop during condensation of refrigerants inside horizontal enhanced tubes. International Journal of Refrigeration 23, 4-25, 2000

[18] J. Yu, S. Koyama: Condensation heat transfer of pure refrigerants in microfin tubes. Proc 1998 Int. Refrig. Conf. at Purdue, p.325-330, 1998

[19] J. A. Olivier, L. Liebenberg, J. R. Thome, J. P. Meyer: Heat transfer, pressure drop, and flow pattern recognition during condensation inside smooth, helical micro-fin, and herringbone tubes. International Journal of

Refrigeration 30, 609-623, 2007

[20] L. Friedel, Improved friction pressure drop correlations for horizontal and vertical two phase pipe flow, 3R International 18. Jahrgang, Heft 7, July 1979

[21] H. Müller-Steinhagen, K. Heck: A simple friction pressure drop correlation for two-phase flow in pipes. Institut für Thermische Verfahrenstechnik, Universität Karlsruhe, Postfach 6980, 7500 Karlsruhe 1 (F.R.G.), 1986

[22] A. Cavallini, D. Del Col, L. Doretti, G.A. Longo, L. Rossetto: Pressure drop during condensation and vaporization of refrigerants inside enhanced tubes. Heat and Technology, 15(1):3-10, 1997

[23] H. Haraguchi, S. Koyama, J. Esaki, T. Fujii: Condensation heat transfer of refrigerants HFC134a, HCFC123 and HCFC22 in horizontal smooth tube and a horizontal microfin tube. Proc. 30th National Symp oj Japan, Yokohama, p. 343-5, 1993

[24] A. Cavallini, D. Del Col, M. Matkovic, L. Rossetto: Frictional pressure drop during vapour-liquid flow in minichannels: Modelling and experimental evaluation. International Journal of Heat and Fluid Flow 30, 131-139, 2009

[25] O. Garcia-Valladares: Review of in-tube condensation heat transfer correlations for smooth and microfin tubes. Heat Transfer Engineering, 24(4): 6-24, 2003

[26] M. B. Pate, S. J. Eckels: Evaporation and condensation of HFC-134a and CFC-12 in a smooth tube and micro-fin tube. ASHRAE Transactions, 97 (2), p. 68-78, 1991

[27] D. Han, Kyu-Jung Lee: Experimental study on condensation heat transfer enhancement and pressure drop penalty factors in four microfin tubes. International Journal of Heat and Mass Transfer 48, 3804-3816, (2005)

8 APPENDIX

8.1 Temperature trend around the tube

In this section, the trend of the temperature around the tube is considered. In particular, the temperature difference between the propylene and the wall is analyzed, since this parameter is involved in the calculation of the heat transfer coefficient, as shown in Equation (4.10), Equation (4.11) and the following, in Chapter 4.2.

The wall temperature is collected by the thermocouples glued in the external diameter of the inner tube. Thermocouples $2, 6, 13, 18, 24$ are broken so their values are not considered. Data collected at $p = 11{,}4\ bar$ for both $G = 600\ kg/m^2s$ and $G = 300\ kg/m^2s$ are presented as an example to have a visualization of the general trend.

Figure 8.1 and Figure 8.2 show the temperature difference around the tube in the four measurement sections, at $G = 600\ kg/m^2s$ and $p = 11{,}4\ bar$, respectively at $x = 0{,}1$ and $x = 0{,}9$.

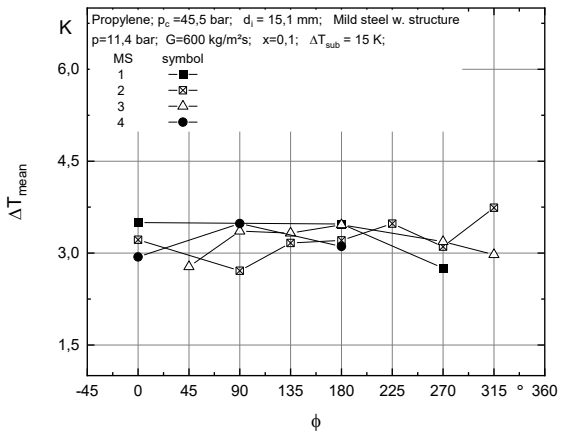

Figure 8.1: Temperature difference between propylene and the tube wall over the circumference in the four measurement sections, at $G = 600\ kg/m^2s$, $p = 11{,}4\ bar$ and $x = 0{,}1$

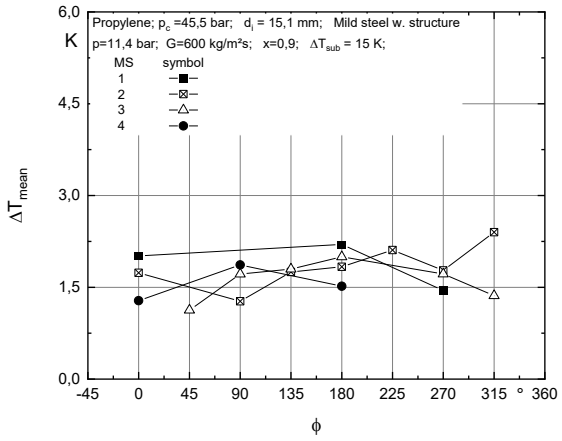

Figure 8.2: Temperature difference between propylene and the tube wall over the circumference in the four measurement sections, at $G = 600\ kg/m^2s$, $p = 11{,}4\ bar$ and $x = 0{,}9$

It can be observed that as the vapor quality increases, the temperature difference decreases. In fact, for $x = 0{,}1$ the temperature difference is around $\Delta T_{mean} = 2{,}7 - 3{,}75\ K$, while for $x = 0{,}9$ $\Delta T_{mean} = 1{,}2 - 2{,}4\ K$.

The considered trend is confirmed considering the same operating pressure at lower mass flux of $G = 300\ kg/m^2 s$ for both $x = 0{,}1$ and $x = 0{,}9$, as it can be seen respectively in Figure 8.3 and Figure 8.4.

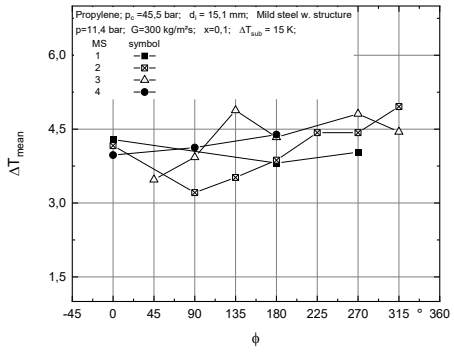

Figure 8.3: Temperature difference between propylene and the tube wall over the circumference in the four measurement sections, at $G = 300\ kg/m^2s$, $p = 11{,}4\ bar$ and $x = 0{,}1$

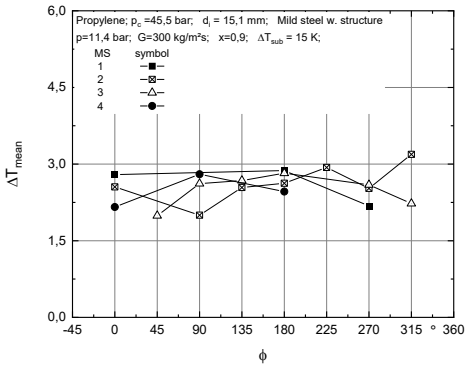

Figure 8.4: Temperature difference between propylene and the tube wall over the circumference in the four measurement sections, at $G = 300\,\frac{kg}{m^2s}$, $p = 11{,}4\ bar$ and $x = 0{,}9$

It is noticeable that the lower mass flux affects the temperature difference, since it can be seen that for $x = 0{,}1$ $\Delta T_{mean} = 3{,}2 - 4{,}9\ K$ while for $= 0{,}9$ $\Delta T_{mean} = 2 - 2{,}9\ K$.